University of Alberta

Numerical Simulation of Time-Dependent Droplet Deformation in an Electric Field

by

Graeme M. Supeene ©

A thesis submitted to the Faculty of Graduate Studies and Research in partial fulfillment of the requirements for the degree of Master of Science.

Department of Mechanical Engineering

Edmonton, Alberta
Spring 2006

Library and
Archives Canada

Published Heritage
Branch

395 Wellington Street
Ottawa ON K1A 0N4
Canada

Bibliothèque et
Archives Canada

Direction du
Patrimoine de l'édition

395, rue Wellington
Ottawa ON K1A 0N4
Canada

Your file Votre référence
ISBN: 0-494-13892-0
Our file Notre référence
ISBN: 0-494-13892-0

NOTICE:
The author has granted a non-exclusive license allowing Library and Archives Canada to reproduce, publish, archive, preserve, conserve, communicate to the public by telecommunication or on the Internet, loan, distribute and sell theses worldwide, for commercial or non-commercial purposes, in microform, paper, electronic and/or any other formats.

The author retains copyright ownership and moral rights in this thesis. Neither the thesis nor substantial extracts from it may be printed or otherwise reproduced without the author's permission.

AVIS:
L'auteur a accordé une licence non exclusive permettant à la Bibliothèque et Archives Canada de reproduire, publier, archiver, sauvegarder, conserver, transmettre au public par télécommunication ou par l'Internet, prêter, distribuer et vendre des thèses partout dans le monde, à des fins commerciales ou autres, sur support microforme, papier, électronique et/ou autres formats.

L'auteur conserve la propriété du droit d'auteur et des droits moraux qui protège cette thèse. Ni la thèse ni des extraits substantiels de celle-ci ne doivent être imprimés ou autrement reproduits sans son autorisation.

In compliance with the Canadian Privacy Act some supporting forms may have been removed from this thesis.

While these forms may be included in the document page count, their removal does not represent any loss of content from the thesis.

Conformément à la loi canadienne sur la protection de la vie privée, quelques formulaires secondaires ont été enlevés de cette thèse.

Bien que ces formulaires aient inclus dans la pagination, il n'y aura aucun contenu manquant.

Canada

ABSTRACT

Deformation of a suspended fluid drop in an electric field is a widely studied phenomenon, and has several significant technological applications. In this study, the suspended drop system is analyzed numerically in terms of its dynamic behaviour. The numerical model is validated with analytic, numerical and experimental results from literature. The response of the system to a step change in the electric field is simulated for numerous parameter variations. Two fundamental cases are studied: one where the fluids are perfectly insulating, and another where finite conductivity is assumed to allow a thin layer of free charge to build up on the drop interface. The dynamic behaviour of this free charge layer, including the effect of convection along the interface due to persistent electrohydrodynamic circulation, is investigated. The departure from linear theory of this system at large deformations is observed and commented on.

TABLE OF CONTENTS

1 Introduction **1**

1.1 Electrical Manipulation of Liquid-Liquid Interfaces 1

1.1.1 Deformation of a Suspended Drop in an Electric Field 2

1.1.2 Technological Applications 3

1.2 Objectives and Scope 5

1.2.1 Objectives: Dynamic Modeling of Suspended Drop Deformation 5

1.2.2 Purpose of the Study 6

1.3 Outline of this Dissertation 6

2 Literature Review of Drop Deformation **8**

2.1 The Perfect Dielectric Model 8

2.2 The Leaky Dielectric Model 12

2.2.1 Theoretical Developments Based on the Leaky Dielectric Model 14

2.3 Numerical Studies of the Deforming Droplet Problem 18

2.4 The Electrokinetic Model 21

2.5 Summary 22

3 Theory and Numerical Formulation **24**

3.1 System Description 24

3.2 Validity of Electrostatic Assumption in Analysis of Electromagnetic Subproblem 26

3.3 Range of Validity of the Leaky Dielectric Model 29
3.4 Governing Equations 30
  3.4.1 Electrostatic Equations 30
  3.4.2 Fluid Mechanics 33
3.5 Boundary Conditions 33
  3.5.1 Far-Field Conditions 33
  3.5.2 Conditions at the Interface Between the Drop and Continuous Phase 34
  3.5.3 Initial Conditions 38
3.6 Nondimensionalization of Governing Equations 39
3.7 Numerical Implementation 41
  3.7.1 Computational Problem Domain 43
  3.7.2 Dynamic Solution Structure 45
  3.7.3 Electrostatics 48
  3.7.4 Interfacial Stresses 51
  3.7.5 Fluid Mechanics 54
  3.7.6 Moving Mesh 58
  3.7.7 Variable Reinitialization 60
3.8 Summary 62

4 Convergence Testing and Verification **63**
4.1 Numerical Convergence Testing 64
  4.1.1 Demonstration of Mesh Independence 64
  4.1.2 Effect of Time Step on Accuracy and Stability 68
  4.1.3 Effect of Solver Tolerances 70
4.2 Accuracy of Small Steady-State Deformations 71
  4.2.1 Perfect Dielectric Model 72

4.2.2 Leaky Dielectric Model 73
4.3 Comparison of Dynamics With Existing Theory 74
4.3.1 Droplet Natural Frequency and Damping 74
4.3.2 Interface Charge Dynamics 77
4.4 Large Deformations: Agreement With Prior Numerical Studies 82
4.4.1 Free Oscillation at High Reynolds Number 83
4.4.2 Large Electrically Induced Deformation 84
4.5 Comparison With Experiments 87

5 Results of the Dynamic Simulations 89

5.1 Perfect Dielectric Results 89
5.1.1 Small Deformations 89
5.1.2 Large Deformations 95
5.2 Leaky Dielectric Results 102
5.2.1 Small Deformations 102
5.2.2 Effect of Charge Dynamics 108
5.2.3 Large Deformations 111
5.3 Lumped Parameter Modeling of Dynamic Responses 119
5.4 Summary 121

6 Conclusions and Further Research 123

6.1 Development of the Numerical Technique 123
6.2 Observed Results 123
6.2.1 Perfect Dielectric Results 123
6.2.2 Leaky Dielectrics: Boundary Charge Dynamics 124
6.2.3 Leaky Dielectrics: Large Deformations 124
6.2.4 Lumped Parameter Modeling 124
6.3 Recommendations for Future Work 125

Bibliography **127**

A Annotated Model Scripts **134**

A.1 Dynamic Interfacial Charge Calculation 134

A.2 Interfacial Curvature Calculation 137

A.3 Moving Mesh 141

A.4 Curve Parameter Correction 145

A.5 Solution Reinitialization 147

LIST OF TABLES

4.1 Perfect Dielectric Base Case 64

4.2 Effect of Mesh Alterations in the Electrostatics Problem 67

4.3 Common Parameters For Figures 4.11a and 4.11b 82

4.4 Parameters for Figures 4.13 and 4.14 84

5.1 Range of Parameters for Small-Deformation Perfect Dielectric Simulations. 90

5.2 Leaky Dielectric Base Case 103

LIST OF FIGURES

1.1 Schematic representation of the deformation of a droplet suspended in a second fluid in the presence of an electric field, $\vec{E}_0$. The dashed circle represents the spherical shape of the non-deformed droplet. The cylindrical coordinate system used in the simulations is also shown. . 2

1.2 The phenomenon of electrowetting: change in contact angle resulting from an applied electric field. 4

1.3 An experimental electrowetting array used to transport droplets under digital control. 4

3.1 A liquid droplet suspended in a second fluid in the presence of an electric field, $\vec{E}_0$. The electrical properties of the two fluids differ, and there is a positive tension at the interface between them. 25

3.2 Two-dimensional axisymmetric geometry for the numerical solution. . 44

3.3 Typical meshed geometry. Dimensions are scaled with respect to the drop radius. The inset shows the details of the mesh near the droplet boundary. 45

3.4 Structure of the dynamic finite element solution. 46

3.5 The principal curvatures of an axisymmetric body. The in-plane curvature is k_1, and the out-of-plane or perpendicular curvature is k_2. . . 51

3.6 Polynomial fitting for a single interface point. The first fit yields the normal vector at the point in question. The second fit is reoriented so that $\hat{n}_i$ is vertical in the local coordinate system, allowing calculation of the local in-plane curvature. 52

3.7 Motion of a single mesh point during the geometry update step, using velocity information from the Navier-Stokes solution. 59

3.8 Geometry, mesh, and solution reinitialization between time steps. Two copies of the FEM structure are used; one for the moved geometry/mesh, and one for the in-place solution reinitialization. 61

4.1 Variation of dynamic response for increasing mesh refinement at drop interface. The parameter varied is 'Hmax', which is a mesh size specification in FEMLAB, applied here to the interfacial boundary only. Time step is 0.06 radians. 65

4.2 Convergence of dynamic response with time step, for a 54-node interface. The nondimensional time step 'tstep' is given in radians, based on the analytic inviscid natural frequency of the drop. 69

4.3 Convergence of dynamic response with time step, for a 33-node interface. 69

4.4 Effect of very small absolute tolerance on the dynamic solution. . . . 70

4.5 Normalized Dynamic Responses for Variation in Electric Fields: Perfect Dielectric Model. 72

4.6 Normalized Dynamic Responses for Variation in Electric Fields: Leaky Dielectric Model. 73

4.7 Comparison of numerical and analytic dynamic responses: Perfect dielectric, low viscosity. 76

4.8 Leaky dielectric model: Comparison of static interfacial charge boundary condition with fast dynamic charge relaxation on interface, for an ionic concentration of 10^{-2} M, yielding a conductivity of 0.075 S/m. . 78

4.9 Total interfacial charge buildup on upper hemisphere as a function of time, for a far-field ionic concentration of 10^{-5} M and a partition coefficient of 1. 79

4.10 Total interfacial charge buildup on upper hemisphere as a function of time, for a far-field ionic concentration of 10^{-7} M and a partition coefficient of 1000. 80

4.11 Steady-state charge distribution on the drop interface, calculated both with and without convection. The solid lines are results from the present work with convection and interfacial dilation accounted for. The dashed lines are obtained from the static model. The open circles are from Feng (1999), Figures 3a and 4a, for comparison. 81

4.12 Comparison of the current model with that of Hirata et al. (2000) for a drop starting from a spheroidal shape with a 2:1 aspect ratio ($d = 1/3$). The drop Reynolds number as defined by Basaran (1992) is 100, and the surrounding fluid exerts negligible stress on the droplet. . . . 83

4.13 Comparison of numerical results with equivalent cases from Hirata et al. (2000): Case 1. 85

4.14 Comparison of numerical results with equivalent cases from Hirata et al. (2000): Case 3. 86

4.15 Steady-state deformation parameter plotted against Weber number for water in decyl alcohol: Comparison with Lu's results. 87

5.1 Effect of (a) droplet viscosity and (b) continuous phase viscosity on perfect dielectric dynamic response. M is the viscosity ratio, μ_i/μ_e. . 90

5.2 Effect of droplet and continuous phase density on the dynamic response of the perfect dielectric model. 92

5.3 Effect of interfacial tension on the dynamic response of the perfect dielectric model. 93

5.4 Fully dimensional plot of the effect of interfacial tension in the perfect dielectric model. 93

5.5 Effect of droplet size on the dynamic response of the perfect dielectric model 94

5.6 Normalized dynamic responses for high applied fields, using the perfect dielectric model. 96

5.7 Deformed droplet shape at end of run for an applied field of (a) 10 MV/m and (b) 20 MV/m. 97

5.8 Normalized dynamic responses at the limit of stability, using the perfect dielectric model. 98

5.9 Normalized dynamic responses for high applied fields in the perfect dielectric base case, but with the drop permittivity reduced from 80 to 8. 99

5.10 Deformed droplet shape at steady-state for $\epsilon_i/\epsilon_e = 2.67$ and an applied field of (a) 50.15 MV/m and (b) 150 MV/m. 101

5.11 Steady-state circulation in the static leaky dielectric model. 102

5.12 Effect of viscosity on leaky dielectric response. 104

5.13 Superimposition of normalized perfect and leaky dielectric results, for comparison of the dynamics. 105

5.14 Prolate deformation of a leaky dielectric droplet due to large ion partition coefficient for the drop. 106

5.15 Dynamic response and steady-state flow pattern for parameters leading to an analytically predicted deformation of zero. 107

5.16 Dynamic contribution from charge relaxation on interface for various fluid conductivities in the full leaky dielectric model. 109

5.17 Steady-state offset from Taylor limit resulting from charge convection in the full leaky dielectric model. 110

5.18 Effect of high applied fields on the static leaky dielectric response. . . 112

5.19 Effect of high applied fields on the static leaky dielectric response, with physical values of the deformation parameter. 112

5.20 Deformed droplet shape and velocity field at end of run for (a) 10 MV/m and (b) 15 MV/m. 114

5.21 Stages of deformation for 10 MV/m leaky dielectric case: (a) 0.06 rad, (b) 1.8 rad, (c) 4.5 rad, and (d) 24 rad (steady-state). 115

5.22 Effect of conductivity ratio on the character of the nonlinearity for an applied field of 10 MV/m. 116

5.23 Deformed droplet shape and velocity field at end of run, for (a) $\alpha = 0.1$ and 10 MV/m and (b) $\alpha = 3$ and 30 MV/m. 117

5.24 Deformed droplet shapes for (a) $\alpha = 0.2$ and (b) $\alpha = 0.5$, with an applied field of 10 MV/m, showing the transition between two modes of nonlinear deformation. 119

5.25 Comparison of the numerical results with analytic predictions and with the ARMAX-derived lumped parameter model, for the perfect dielectric base case with 15 MV/m applied field. 120

NOMENCLATURE

Note that $\vec{\ }$ denotes a vector quantity. The double bar $^{=}$ indicates a tensor. Bold face denotes a matrix.

Roman symbols:

A	Surface Area of an Arbitrary Region on the Drop [m^2]
a	Equatorial Radius of a Deformed Drop [m]
b	Polar Radius (Half-Axis) of a Deformed Drop [m]
Ca	Capillary Number
c^k	Ion Concentration [mol/m^3]
$\vec{D}$	Electric Displacement [C/m^2]
D^k	Ion Diffusion Coefficient [m^2/s]
$\mathbf{d_a}$	FEMLAB Time Coefficient
d	Drop Deformation Parameter [-]
d_t	Theoretical Deformation Parameter (as compared with simulations)
$\vec{E}$	Local Electric Field [V/m]
$\vec{E}^*$	Normalized Local Electric Field [-]

E_0, $\vec{E}_0$	Applied Electric Field [V/m]
E^F	Nondimensional Applied Field From Feng (1999) [-]
E^H	Nondimensional Applied Field From Hirata et al. (2000) [-]
e	Eccentricity of a Spheroid
$\mathbf{F}$	FEMLAB General Form Forcing Term
$\mathcal{F}$	Faraday's Constant [C/mol]
f_b	Fluid Body Force [N/m^3]
$\mathbf{G}$	FEMLAB Neumann Condition
H	Conductivity Ratio, Drop:Medium
$\mathbf{h}$	FEMLAB Boundary Variable: $-\frac{\partial \mathbf{R}}{\partial \mathbf{u}}$
$\bar{\bar{I}}$	Identity Tensor
K	Dielectric Constant ($4\pi\epsilon_0\epsilon_r$)
k_1	rz-Plane Curvature [m^{-1}]
k_2	Out-of-Plane (Perpendicular) Curvature [m^{-1}]
l	Characteristic Length (Generic) [m]
M	Dynamic Viscosity Ratio, Drop:Medium
N	Density Ratio, Drop:Medium
n	Drop Oscillation Mode Number

$\hat{n}$	Outward Normal Vector [-]
n_r	Radial Component of $\hat{n}$
n_z	Axial Component of $\hat{n}$
$\vec{P}$	Electric Polarization [C/m^2]
p	Local Fluid Pressure [Pa]
p^*	Nondimensional Local Fluid Pressure [-]
p_0	Characteristic System Pressure [Pa]
Q	Ruark Number
q	Surface Charge Density [C/m^2]
q^*	Nondimensional Surface Charge Density [-]
R	Universal Gas Constant [J/mol·K]
R_d	Deformed Drop Radius (Local) [m]
R_0	Initial Drop Radius [m]
$\mathbf{R}$	FEMLAB Dirichlet Condition
r	Radial Coordinate [m]
r^*	Normalized Radial Coordinate [-]
Re	Reynolds Number
S	Permittivity Ratio, Drop:Medium

$\vec{S}_n$	Interfacial Stress, Electrical + Interfacial Tension [Pa]
St	Strouhal Number
s	Laplace Transform Variable Corresponding to t
T	Temperature [K]
T_0	Interfacial Normal Stress, Electrical + Fluid [Pa]
t	Time [s]
t^*	Nondimensional Time [rad]
$\hat{t}$	Unit Tangent Vector [-]
u	Radial Fluid Velocity (r-dir) [m/s]
u^*	Nondimensional Radial Fluid Velocity [-]
$\mathbf{u}$	FEMLAB Independent Variables
V^*	Nondimensional Electric Potential [-]
v	Axial Fluid Velocity (z-dir) [m/s]
v^*	Nondimensional Axial Fluid Velocity [-]
$\vec{v}$	Fluid Velocity [m/s]
$\vec{v}^*$	Nondimensional Fluid Velocity [-]
v_0	Characteristic System Velocity [m/s]
We	Weber number

z	Axial Coordinate [m]
z^*	Normalized Axial Coordinate [-]
z^k	Ion Valence [-]

Greek symbols:

α	Ion Partition Coefficient, Drop:Medium
$\mathbf{\Gamma}$	FEMLAB General Form Flux Term
γ	Interfacial Tension [N/m]
ϵ_0	Permittivity of Free Space [F/m]
ϵ_r	Relative Permittivity [-]
ϵ_i, ϵ_e	Relative Permittivities of Internal and External Phases [-]
θ	Azimuthal Angle [rad]
$\boldsymbol{\mu}$	FEMLAB Lagrange Multipliers
μ	Fluid Viscosity [Pa·s]
μ_0	Permeability of Free Space [H/m]
μ_r	Relative Permeability [-]
ρ	Fluid Density [kg/m^3]
ρ_f	Free Charge Density [C/m^3]
σ	Conductivity [S/m]

σ_d	Damping Rate [s^{-1}]
$\bar{\bar{\sigma}}^M$	Maxwell Stress Tensor [Pa]
τ	Drop Oscillation Time Scale [s]
Φ	Taylor's Discriminatory Function
ϕ	Polar Angle [rad]
X	Interface Mean Curvature [m^{-2}]
Ψ	Electric Potential [V]
ω_n	Inviscid Oscillation Speed of Mode n [rad/s]
ω_d	Damped Oscillation Speed For a Given Mode [rad/s]

Miscellaneous:

e	Subscript: External Fluid (Medium)
i	Subscript: Internal Fluid (Drop) or Boundary Point Index
j	Subscript: Summation Index
k	Superscript: Ion Species Index
T	Superscript: Tensor Transpose
$\bar{\nabla}$	Normalized Gradient [-]
∇_s	Gradient Along a Surface [m^{-1}]

CHAPTER 1

INTRODUCTION

1.1 Electrical Manipulation of Liquid-Liquid Interfaces

An interface between two fluids having different electrical properties experiences a force when an electric field is applied to it. The electrical Maxwell stress, which is proportional to the square of the applied field, causes the fluid interface to deform. This is a subset of a class of phenomena known as electrohydrodynamics [Melcher and Taylor, 1969, Saville, 1997], in which electrical forces on a fluid induce hydrodynamic flow.

The electrical force at an interface between two fluids depends on two separate effects. One, a polarization stress can develop normal to the interface if the two fluids have different dielectric permittivities. This effect in isolation can generate transient flow patterns, but it does not tend to produce shear flow or vortices, and the steady state is generally quiescent. Two, the presence of finite conductivity raises the possibility of free charge accumulating at an interface if the ratio between the permittivities of the two fluids differs from the ratio between their conductivities. The force exerted by an electric field on an interface possessing free charge depends only on the direction of the electric field, and therefore produces tangential forces on the interface, supporting the possibility of steady shear or vortex flows.

Another phenomenon of interest occurs where a liquid interface encounters a solid surface. Interfacial tension between the three phases (solid, liquid, liquid) gives rise to a characteristic contact angle. The application of an electric field to the three-phase contact line alters the contact angle. This phenomenon is known as electrowetting [Cho et al., 2003], due to the fact that very often a drop which was formerly non-wetting (contact angle > 90°) can be made wetting by the application of an electric field.

1.1.1 Deformation of a Suspended Drop in an Electric Field

A fluid drop suspended in another immiscible fluid will deform when subjected to an electric field. The electrical and fluid mechanical properties of the fluids determine the character of the deformation. Figure 1.1 shows a representative schematic.

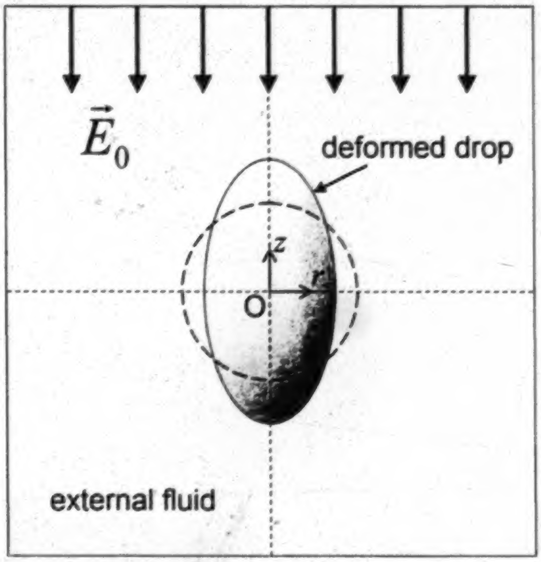

Figure 1.1: Schematic representation of the deformation of a droplet suspended in a second fluid in the presence of an electric field, $\vec{E}_0$. The dashed circle represents the spherical shape of the non-deformed droplet. The cylindrical coordinate system used in the simulations is also shown.

The deformation of a drop in an electric field is characterized by a balance of stresses at the drop interface. The electrical stresses cause the interface to distort, while interfacial tension tends to restore the spherical shape. Viscous stresses and fluid pressure gradients due to the flow fields can alter the deformation substantially. The mathematical description of this system requires simultaneous solution of the dynamic fluid mechanical equations and the equations of electrostatics.

1.1.2 Technological Applications

Electrical drop deformation has a wide variety of applications. Knowledge of this phenomenon is useful in the study of aerosols, or in the enhancement of heat or mass transfer between phases in dispersions or colloids. It is important in inkjet printing, and can be utilized to induce and control directionality in the properties of a blended polymer melt by aligning the dispersed phase. Removal of finely dispersed contaminant phases from liquids such as synthetic crude oil could be accomplished by coalescence enhancement. Additionally, knowledge of how this free-surface problem behaves and understanding of the underlying physics could assist in the development of technologies that employ similar or related effects, such as electrowetting.

Electrowetting is of immense interest, because it can be used as an actuation mechanism for lab-on-a-chip devices. A lab-on-a-chip is essentially a digitally controlled microscale chemical laboratory, which can be automated to perform rapid chemical testing using extremely small quantities of a reagent. Several technologies to actuate fluid on the chip are being developed, and electrowetting is one of the most promising.

The basic phenomenon of electrowetting is shown in Figure 1.2. It involves the change in contact angle of a liquid interface on a solid surface, often in such a way that a previously nonwetting drop configuration becomes wetting. Since the change in contact angle produces a change in the direction of the surface tension force on the three-phase contact line, it is possible to apply a field preferentially to one side of a

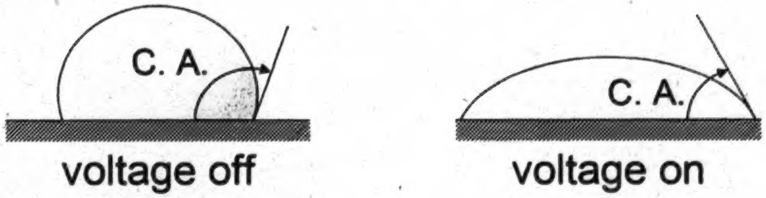

Figure 1.2: The phenomenon of electrowetting: change in contact angle resulting from an applied electric field.

drop in order to produce an unbalanced force and generate motion.

This is the principle used in the device shown in Figure 1.3. The electrode squares are serrated so as to maintain contact with a drop on a neighbouring electrode. The initial state is shown in Figure 1.3a. When an electrode adjacent to the drop is turned on, the contact angle changes on that side and the drop experiences an unbalanced force that causes it to move onto the active electrode, as in Figure 1.3b. The end result is that the entire drop is transferred over to the active electrode, which can then be switched off (Figure 1.3c). Discrete manipulation of fluid droplets on branching paths is one of the major advantages of this approach. This technique has been adapted to (1) create drops from a reservoir, (2) mix two drops, and (3) break one drop into two [Cho et al., 2003]. Together with (4) controlled transport of droplets

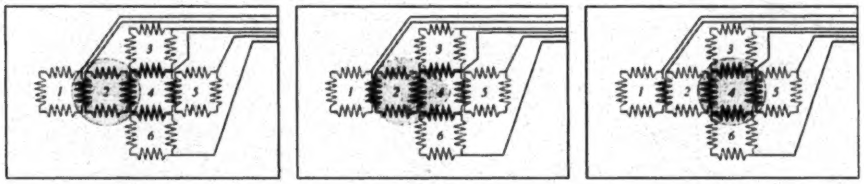

(a) (b) (c)

Figure 1.3: An experimental electrowetting array used to transport droplets under digital control.

on the chip, these tasks comprise the four basic functions that would be required of a working lab-on-a-chip device.

Unfortunately, the dynamic behaviour of these drops is not well understood. Their demonstrated lack of reliability in practical applications may be caused by dynamic instabilities which are not predicted by the existing theory. A better understanding of the underlying physics of electrowetting, coupled with an understanding of the liquid drop dynamics, is required.

1.2 Objectives and Scope

1.2.1 Objectives: Dynamic Modeling of Suspended Drop Deformation

This study encompasses the problem of the electrical deformation of a single drop of incompressible, Newtonian fluid suspended in an incompressible, Newtonian continuous phase. The fluids are immiscible. The drop is sufficiently large that the continuum assumption remains valid, but sufficiently small that the effects of gravity do not become important. Although simple electrolytes may be present in either or both of the fluids, no surfactant effects or solute adsorption on the fluid interface are considered.

It is the objective of this research to develop and test a numerical model capable of predicting the dynamic response of the fluid system described above to a step applied electric field. The case where both fluids are perfect dielectrics is solved first, followed by a treatment allowing finite conductivity. The finite-conductivity model is extended to allow time-dependent charge buildup on the interface due to migration, as well as alteration of the transient and equilibrium interface charge distribution by lateral convection and interface dilation. Large deformations of both perfect and leaky dielectric systems are simulated to equilibrium, or to the initiation of drop breakup/burst if no equilibrium exists.

1.2.2 Purpose of the Study

It is expected that this research will lead to an improved understanding of the effects and processes underlying electrohydrodynamic deformation of a fluid interface. Numerical requirements for dealing with liquid-liquid deformable interfaces are to be clarified, and the correct forms of the physical equations and boundary conditions are to be thoroughly understood.

The success of this research is expected to facilitate an investigation into the behaviour of electrowetting systems. The phenomenon of electrowetting cannot be considered in isolation; the accompanying framework of drop behaviour in an electric field must be considered simultaneously. Dynamic simulation of a fully three-dimensional three-phase system with the complexity required to understand the physics of electrowetting is not trivial [Shapiro et al., 2003], and requires some groundwork. Laying that groundwork is a major aim of this research.

1.3 Outline of this Dissertation

In Chapter 2, the history of the electrical drop deformation problem is reviewed, with important results highlighted. Particular attention is given to the two original analytic results, dealing with perfect dielectrics and with leaky dielectrics. A summary of numerical investigations is provided.

The theoretical basis for this work is examined in Chapter 3, starting with a discussion of the validity of the electrostatic equations, and proceeding to the fluid mechanics and the form of the stress balance. The numerical method is also detailed in the second part of the chapter.

Chapter 4 presents validation results for the numerical technique developed here. The results of the numerical simulations are compared with steady-state and transient theory, and found to accord well with analytic results. Testing of the numerical method against similar computational techniques is carried out. Finally, a comparison with a set of experimental results tests the ability of the method to predict physical phenomena outside the range of the linear theories.

Simulation results are presented in Chapter 5. The perfect dielectric case is treated first, and is examined in various small-deformation cases to illustrate the physical significance of the simulation results in the language of dynamic systems. Larger deformations illustrate nonlinearities occurring at high applied fields. The leaky dielectric model is analyzed for both static and dynamic interface charge, and the effects of finite conduction time and charge convection on the dynamic response are demonstrated. Large-deformation simulations with the static charge boundary condition are performed in order to observe the characteristic modes of nonlinear deformation. A second-order lumped-parameter model fit to numerical data is demonstrated, offering the possibility of rapid dynamic modeling in a real-time control application.

In Chapter 6, conclusions are drawn and potential future work is discussed.

CHAPTER 2

LITERATURE REVIEW

The deformation of a droplet in an electric field has been extensively studied. Industrial applications include spraying/aerosols, inkjet printing, enhancement of heat or mass transfer in emulsions, and coalescence of droplets for de-emulsification purposes. Early studies in the 1920s and 1930s involved experimental observations of the behaviour of water droplets or soap bubbles in air, subjected to an electric field. The related problem of a droplet deforming and bursting in shear or extensional flow was well studied analytically in the 1930s; Taylor (1934) produced an analytic result for small deformations of drops in shear flow, and did several experiments. When the mathematical study of electrical drop deformation began in earnest, the similarity in form between the two problems led to close links between them in the early papers, but the electrical problem showed nonlinearities not present in the pure flow problem. These nonlinearities severely restrict the range of validity of the analytic solutions and continue to complicate numerical and experimental analysis of this problem.

2.1 The Perfect Dielectric Model

The first known analytic result predicting the value of the induced deformation of a drop in an electric field was derived in 1953 by O'Konski and Thacher for perfectly insulating drops in perfectly insulating media. Their paper used an energy method to derive an expression for the steady-state droplet deformation, assuming that the field is sufficiently small that the droplet remains nearly spherical. It was further assumed that the droplet's deformed shape approximates a spheroid of eccentricity e. Since it can be shown that the Maxwell stress on an interface between two perfect dielectrics is normal to the interface, and that there is no force in the bulk fluid, their solution assumed no fluid motion. Gravity was ignored, because it can be shown to be negligible in the size range of interest, and electrostriction was ignored due to the nearly incompressible behaviour of the liquids in question.

The full solution obtained by O'Konski and Thacher (1953) is as follows:

$$R_0\epsilon_0 E_0^2 \frac{(\epsilon_i - \epsilon_e)^2}{2\gamma\epsilon_e} = \frac{[(3-2e^2)/(1-e^2)^{2/3} - (3-4e^2)\sin^{-1} e/\langle e(1-e^2)^{7/6}\rangle]}{[\{3/e - e\}\{\ln\langle(1+e)/(1-e)\rangle\} - 6]/e^2[1+(\epsilon_i - \epsilon_e)B/\epsilon_e]^2} \tag{2.1}$$

where

$$B = [1-e^2][\ln\{(1+e)/(1-e)\} - 2e]/2e^3 \tag{2.2}$$

The original expression was difficult to interpret; a clarification has been obtained from the work of Lev et al. (2001), who used a similar technique in their analysis of the deformation of liquid crystal droplets.

By expressing this result in terms of power series, and assuming that $e^2 \ll 1$, O'Konski and Thacher reduced the above expression to a small-deformation limit, as follows:

$$e = \frac{3E_0(|\epsilon_i - \epsilon_e|)\sqrt{\epsilon_0\epsilon_e R_0/\gamma}}{2(\epsilon_i + 2\epsilon_e)} \tag{2.3}$$

Allan and Mason (1962) performed a force balance over a dielectric droplet in a dielectric medium. In their solution, the shape of the approximately ellipsoidal deformed droplet is given by:

$$R_d = R_0[1 + d\cos 2\phi] \tag{2.4}$$

where ϕ is the polar angle measured at a point on the interface. This expression introduces the deformation parameter d, which is equal to:

$$d = (b-a)/(b+a) \tag{2.5}$$

Here b is the polar half-axis and a is the equatorial radius. Allan and Mason's force balance produces the following result:

$$d = \frac{9R_0K_eE_0^2(S-1)^2}{64\pi\gamma(S+2)^2} \tag{2.6}$$

in which K_e is the dielectric constant of the medium. This notation, which was used by Allan and Mason (1962), represents the inverse of Coulomb's constant, and is equal to $4\pi\epsilon_0\epsilon_e$. S is the ratio of the dielectric constant of the drop to that of the medium, calculated as K_i/K_e.

Allan and Mason noted that if the deformation is small, d approaches $e^2/4$. Using this, one can express the small-deformation limit of O'Konski and Thacher's result as:

$$d = \frac{9R_0\epsilon_0\epsilon_eE_0^2(S-1)^2}{16\gamma(S+2)^2} \tag{2.7}$$

which is equivalent to Allan and Mason's result. Note that the deformation must always be positive; *i.e.*, the resultant deformed shape is always a prolate spheroid, elongated in the direction of the electric field. Equation 2.7 is sometimes referred to as the OTAM result, standing for the names of the four researchers who developed it.

Allan and Mason (1962) also reported experiments in their paper, in which they attempted to verify their analytic result. The paper's scope included deformation and burst of droplets in shear flow, electric fields, and combined shear/electric fields. The shear problem had been well studied prior to their publication, and the expected agreement with Taylor's result [Taylor, 1934] was observed. However, the electrical problem showed substantial discrepancies, and in some cases oblate deformation (compression in the axis of the applied field) was observed, although it is clear from Equation 2.7 that this should be impossible.

Prior to Allan and Mason's efforts, O'Konski and Harris (1957) had speculated that the finite conductivity of most real fluids could alter the electric fields, and had given an expression predicting oblate deformation for certain cases. However, none of Allan and Mason's experiments were within the necessary parameter ranges. Allan and Mason (1962) also noted that negative charge tends to leak through silicone oil, and that some of their drops had acquired a net charge due to this effect during the experiments. It was speculated that this might have relevance, but the problem was not addressed further by them.

Garton and Krasucki (1964) derived the shape of a bubble in an electric field for the perfect dielectric case and for perfectly conducting bubbles. The result was compared with the exact spheroidal shape for an aspect ratio of 1.4055, and the results were in extremely good agreement, indicating that the shape of the bubble does remain nearly spheroidal under substantial electrical deformation. It was also noted that for large deformations of conducting or highly polarizable drops, a turning point exists beyond which the necessary applied field for equilibrium decreases with further deformation, generating a second family of unstable solutions for applied fields near the turning point. This implies that for a given system, there is a critical applied field beyond which no equilibrium shape exists. The critical bubble shape was calculated to correspond to a prolate aspect ratio of 1.85. Experiments bore out these predictions, and a mode of breakup was observed in which a water drop developed sharp points at either end and ejected a spray of fine droplets from each point.

Taylor (1964) calculated the stress on a spheroid due to an electric field for arbitrary deformations, assuming that the shape remains spheroidal and utilizing two separate approximations. He noted, as did Garton and Krasucki (1964), that for certain cases a turning point exists beyond which the applied field necessary to sustain equilibrium decreases as the deformation rises, and calculated the critical aspect ratio as 1.9.

Rosenkilde (1969) analyzed the large-deformation behaviour of drops in an electric field under the spheroidal assumption. The analysis indicated that for certain values of the permittivity ratio and the applied field, it is possible for three separate equilibrium aspect ratios to exist, only one of which is unstable. For these cases the turning point noted by Garton and Krasucki (1964) and Taylor (1964), past which a negative relationship exists between deformation and equilibrium field, has a counterpart at very high deformations where the relationship becomes positive again. This produces a third family of equilibrium shapes, which are highly elongated but stable.

2.2 The Leaky Dielectric Model

In 1966, Sir Geoffrey Taylor published a work in which the effect of small conductivity was addressed [Taylor, 1966]. He criticized the solution of O'Konski and Harris (1957) because their energy minimization technique neglected surface charge on the drop. He noted, however, that their discriminatory function for prolate vs. oblate drops can become zero, indicating a spherical drop. This was taken to suggest fluid motion, with hydrodynamic stress balancing the electrical stress, since no other restoring effect in the system can vary over the surface of a spherical drop. Taylor then proceeded to perform a combined electrical/hydrodynamic stress analysis, utilizing the known electrical solution for steady current and the Stokes equations for fluid flow. Taylor's electrohydrodynamic solution predicts circulatory flow inside the drop and approximately hyperbolic flow outside the drop in steady-state, and provides a revised discriminatory function based on the corrected stress profile.

The discriminatory function takes the same sign as the deformation parameter; positive for a prolate drop (elongated in the electric field axis), and negative for an oblate drop (compressed in the electric field axis). Taylor compared the experiments of Allan and Mason (1962) with the value of the revised function, where Allan and Mason's published data allowed its calculation, and in every such case it correctly predicted the differentiation between prolate and oblate drops.

An addendum to Taylor (1966) by McEwan and de Jong described flow visualization experiments with a silicone oil drop in a mixture of corn oil and castor oil. Mearlite dry powder was used as a tracer, with a narrow plane of illumination provided perpendicular to the line of observation. The observed deformation was oblate, as predicted by Taylor's theory, and circulation was also observed in accordance with the theory, in the predicted direction.

In 1969, Melcher and Taylor published a review on the subject of electrohydrodynamics. In it, the theory of electrohydrodynamics was elucidated by means of several example problems, one of which was the droplet deformation problem. A small arithmetical error in Taylor's paper was corrected by Melcher and Taylor, who gave a revised discriminatory function:

$$\Phi(S,H,M) = (H^2+1)/S - 2 + 3(H/S-1)\left(\frac{2+3M}{5+5M}\right) \tag{2.8}$$

in which

$$S = \frac{\epsilon_i}{\epsilon_e}, \quad H = \frac{\sigma_i}{\sigma_e}, \quad M = \frac{\mu_i}{\mu_e}$$

If Equation 2.8 is positive, the corresponding deformation will be prolate. If it is negative, the deformation will be oblate.

The combined electrical and fluid mechanical normal stress distribution T_0 involving Φ from Equation 2.8 can be obtained from:

$$T_0 = \frac{9\epsilon_0\epsilon_i E_0^2 \Phi}{2(2+H)^2} \tag{2.9}$$

which gives rise to the Taylor result for small deformations of a leaky dielectric droplet:

$$d = \frac{9R_0\epsilon_0\epsilon_e E_0^2}{16\gamma(2+H)^2}\left[H^2 + 1 - 2S + 3(H-S)\left(\frac{2+3M}{5+5M}\right)\right] \tag{2.10}$$

Equation 2.10 can be used to predict deformations for drops with arbitrary nonzero conductivities. If the conductivity of the drop becomes infinite, this expression is identical with the OTAM result of Equation 2.7 for the case of infinite drop permittivity. However, in the general case, if both conductivities are reduced to zero, the Taylor result (Equation 2.10) does not converge to the OTAM result, because it depends only on the ratio of the conductivities and not on their absolute values. The Taylor result was derived under the assumption that the conductivities of the droplet and continuous phase are uniform except at the interface, which is not true if the electrolyte concentrations are extremely low. It might therefore be expected that these two results are limiting cases of a more general equation.

2.2.1 Theoretical Developments Based on the Leaky Dielectric Model

Torza, Cox, and Mason (1971) performed experiments to test the effects of steady and oscillating electric fields on suspended fluid drops. They also extended Taylor's result analytically to include the effects of oscillating electric fields. Their experimental results agreed qualitatively with the leaky dielectric theory, including the proportionality with E_0^2 common to both analytic theories, but in most cases the deformation was greater than predicted, sometimes by a factor of 3 or 4.

Attempting to explain the discrepancy, Torza et al. (1971) considered the possible importance of surface conductance and of charge convection along the interface. They concluded that their experiments did not show any consistent effects which could be related to a surface conductance term, and that convection of charge was not important in the parameter range employed. They recommended that the limitations of the electrical theory, including possible effects of diffuse ionic layers, be investigated further, and that the inertial terms in the Navier-Stokes equations be considered.

Several attempts have been made to improve the agreement of theory with experiment. Sozou (1972) introduced a correction to the equations of Torza et al. (1971) by including the acceleration term in the fluid mechanics equations. It was pointed out that while the neglect of this term is justifiable in the case of Taylor's steady-state solution for constant electric field, it is not justifiable if oscillatory electric fields are present, and under certain conditions Torza et al.'s theory is invalid. However, the data provided by Torza et al. were insufficient to allow unique solutions using Sozou's more complex theory, which rendered a test of the theory difficult in this case.

Ajayi (1978) attempted to improve on the small-deformation assumption, by which Taylor and other researchers assumed the drop to remain nearly spherical. The method used was a polynomial expansion on the drop shape, with the first-order perturbation term employed to increase the accuracy of the leaky dielectric result to second-order in deformation. Some improvement with respect to comparison with experimental results was achieved; however, the correction was insufficient to remove the discrepancy.

Baygents and Saville (1989) introduced an electrokinetic solution, as suggested by Torza et al., in which space charge accumulates in the vicinity of the drop interface. A singular perturbation method was used to derive the electrical stresses and drop deformation, with the result that Taylor's solution was reproduced exactly. This demonstrated that the space charge buildup described by the electrokinetic model is analytically equivalent to the surface charge implicit in the leaky dielectric model. However, due to the perturbation method used, this conclusion is only valid if the electrostatic double layer thickness is substantially smaller than the drop radius.

Vizika and Saville (1992) performed experiments with suspended drops under steady and oscillatory electric fields. No new theory was developed, but care was taken to obtain accurate physical parameters for the systems under test. The agreement with theory was substantially better overall than for Torza et al.'s experiments. The steady field tests showed some discrepancies with the theory, although an improvement was noted. Tests of the theory for oscillatory applied fields demonstrated good quantitative agreement between theory and experiment.

Bentenitis and Krause (2005) developed an extension to the leaky dielectric model for steady electric fields, by using a spheroidal coordinate system to allow better approximation of large deformations. Their theory improves on the linear perturbation theory markedly in the case of prolate deformations, showing quantitative agreement in cases where the original theory fails to capture the general trend of the data. However, the ability of this extended leaky dielectric model to quantitatively predict oblate deformations is limited.

Due to the interest in the subject, various extensions have been proposed for the Taylor leaky dielectric theory. Some of these have to do with extending the range over which the theory is valid, and have been listed above. In some cases, however, the intent is to deal with a problem that Taylor's theory was not intended to solve, and the generality of the theory is increased by the extension.

Sozou (1973) analyzed the transient response of a leaky dielectric droplet to a step electric field, for asymptotic perturbations. Results indicate that the development of the interfacial flow may have a non-monotonic transient, and that the external flow begins with closed circulation cells, which eventually propagate outwards and become the approximately hyperbolic pattern predicted by Taylor's result. Sozou's solution, like its precursors, is valid only for small deformations.

Feng and Beard (1990, 1991, 1991) studied the effects of harmonic resonance and mode coupling in charged, electrically suspended drops and in drops forced by an alternating field. The analysis was extended to three-dimensional spherical harmonics by an asymptotic analysis, and the deformation and viscosity were both assumed to be small. Lee and Kang (1999) presented an analytic result for steady deformation and small-amplitude oscillations of a generalized three-dimensional drop. Non-uniform applied fields were permitted in their analysis. The deformation was described by superimposition of a finite number of spherical harmonics. For small deformations and to a first-order approximation, the results of Lee and Kang's work indicated that free oscillation frequencies depend only on the steady part of the electrically induced deformation.

The original Taylor result and its derivatives neglected the possibility of non-electrical solute adsorption on the drop interface. Ha and Yang (1995, 1998) studied the effect of surfactant adsorption on the electrohydrodynamic drop deformation problem. Particular attention was given to the modes of breakup and the effect of the surfactant on them, and an analytic stability analysis was performed.

Feng (2002) dealt with a non-axisymmetric characteristic of leaky dielectric systems; the phenomenon of electrorotation. If the continuous phase is more conductive than the drop, a reversed dipole can develop across the drop in unstable equilibrium with the electric field. If the field exceeds a critical value, the drop will rotate indefinitely as the inverted dipole is maintained by conduction against the convective effect of the rotation. Feng's result was derived for two-dimensional (cylindrical) drops, but elementary components of the three-dimensional theory were derived and compared qualitatively with the two-dimensional result.

Saville (1997) provided a comprehensive review of the field of electrohydrodynamics, and reiterated several key results.

2.3 Numerical Studies of the Deforming Droplet Problem

Since the theoretical treatments of drop deformation in an electric field are limited to small deformations, or large deformations with assumptions placed on the shape, there has been a significant and continuing interest in finding numerical solutions to these problems. Numerical solutions do not suffer from the same limitations as the analytic theories, although care must be taken to ensure the correctness of the results. Attempts to model this problem computationally appear quite early following the initial analytic efforts, and continue with the present study.

Brazier-Smith (1971) and Brazier-Smith, Jennings and Latham (1971) carried out pioneering computational treatments of the drop deformation problem. Their studies dealt with conducting drops with constant surface potential, both isolated and in pairs, and with isolated charged drops. Brazier-Smith employed a finite perturbation technique to converge to the correct force balance for this system, yielding the steady-state result, which for relatively large deformations showed a small deviation from the spheroidal shape. Brazier-Smith, Jennings and Latham solved the irrotational, inviscid fluid mechanics equations to provide dynamic analyses of drop deformation and contact between drop pairs. Their simulations with individual drops showed the development of conical tips in extreme cases of deformation. Due to the irrotational equations used, the solution could not be continued past the development of these points. Brazier-Smith, Jennings, and Latham also performed experiments with falling drop pairs in order to verify the numerical results.

Miksis (1981) solved the steady-state perfect dielectric problem using Newton's method with stepwise changes in applied field. The dielectric constant of the drop was varied in these calculations, and it was observed that the drop developed pointed ends only when the drop's dielectric constant was higher than a certain critical value. Below this value, the drop continued to elongate while maintaining a roughly spheroidal profile.

Sherwood (1988) analyzed the leaky dielectric model by means of a boundary integral method. Viscosity was included in the model, but the droplet and medium were assumed to be equally viscous. The momentum term in the Navier-Stokes equations was neglected, as the boundary integral method is not capable of dealing with nonlinearity. Large deformations were obtained by stepwise increases in the applied field. Sherwood's results indicate that when the permittivity ratio ϵ_i/ϵ_e is high enough, the drop develops the pointed ends characteristic of tip streaming, whereas a high conductivity ratio tends to produce the bulbous-ended breakup mode.

Basaran and Scriven (1989) performed a finite element analysis of the shape patterns and stability of a charged drop in an electric field. Their method was steady-state, and assumed infinite drop conductivity, so that the final state did not involve flow, and hence the fluid mechanics equations were not necessary. They followed the solution around the turning points noted previously, into the unstable regime.

Haywood, Renksizbulut, and Raithby (1991) developed a numerical technique to predict the transient deformation history of a perfect dielectric system. Differences between the stability limits predicted from steady-state analysis and from their fully dynamic model were observed. An analytic model was developed which shows some of the characteristics of the numerical model for small deformations.

Tsukada, Katayama, Ito and Hozawa (1993) performed experiments with the system of mixed vegetable oil and silicone oil studied by McEwan and de Jong in their addendum to Taylor (1966). Two experimental cases were studied, one with silicone oil as the drop and mixed corn and castor oil as the medium, and the other case with these components reversed. The experiments were accompanied by steady-state numerical calculations using the finite element method. The finite element calculations used Taylor's leaky dielectric model, with the full steady Navier-Stokes equations, and showed a substantial improvement in predictive power over the analytic formulae. Subsequent studies headed by Tsukada have used the same numerical technique to deal with the cases of a moving drop and of a compound drop; that is, a drop with a smaller immiscible drop inside it.

Basaran, Patzek, Benner, and Scriven (1995) analyzed an inviscid, infinitely conducting drop in terms of its nonlinear oscillatory behaviour and breakup modes, using the finite element method. The oscillations were followed in detail, and multiple harmonics were observed. During breakup, the ends of the drop became pointed, and thin threads of fluid appeared, jetting out of the nearly singular tips. Instances of numerical codes successfully continuing past the development of the pointed tip are rare; it is not clear that this was not a numerical artifact, but it is significant nonetheless.

Feng and Scott (1996) employed the Galerkin finite element technique in a comprehensive steady-state analysis of the leaky dielectric model. The previously noted turning points, beyond which the steady-state solution is unstable, were followed in detail, and the effect of finite Reynolds number on the solution was characterized. The effect of charge convection was treated later, in Feng (1999), where a parameter called electric Reynolds number was introduced. This is a ratio of the time scales of charge convection and conduction, and if it is nonzero, the final interfacial charge distribution and droplet deformation can be altered significantly. Feng's analysis used essentially the same finite element method as Feng and Scott (1996), and was steady-state.

In 2000, Tsukada et al.'s method was extended to deal with the full dynamic problem of a leaky dielectric step response of arbitrary magnitude. Hirata, Kikuchi, Tsukada and Hozawa (2000) presented representative results for the dynamic response of the silicone oil/vegetable oil systems studied by Tsukada (1993). The dynamic response of their model was compared with a highly oscillatory solution from a paper by Basaran (1992), in which pure droplet oscillations were studied without the presence of electric fields. The particular example used here had a Reynolds number of 100; the agreement between the model of Hirata et al. (2000) and that of Basaran (1992) was excellent. The development of unstable prolate deformation was tracked using parameters corresponding to a drop of mixed vegetable oil in silicone oil, and an unstable oblate mode was observed with the system of silicone oil in mixed oil. This oblate mode developed a sharp edge, similar to the sharp tips observed during prolate breakup by tip streaming. Unfortunately, the moving mesh method used by Hirata et al. (2000) was incapable of continuing past such a singularity. Charge convection and finite conduction time were not considered.

Zhang and Kwok (2005) presented a two-dimensional lattice Boltzmann model of electrohydrodynamic drop deformation. The lattice Boltzmann model has the advantage of not requiring specific treatment of the interface in the numerical method. This is similar to the volume-of-fluid and levelset methods, and like them the method is capable of treating very complex fluid structures with no additional programming. However, these methods also share the disadvantage of a certain degree of imprecision when treating large fluid systems with sharp interfaces.

2.4 The Electrokinetic Model

In 2002, Zholkovskij, Masliyah, and Czarnecki published an electrokinetic solution to the problem of electrically induced small drop deformations. Unlike the solution of

Baygents and Saville, this result is valid for electrostatic double layers of arbitrary size. It appears to represent a more general case than either the perfect dielectric or the leaky dielectric case, as both of these theories appear as limits of the general electrokinetic expression. When the conductivity is very small, the electrostatic double layer thickness tends to infinity, and the value of the deformation converges to the perfect dielectric result. When the conductivity is high, the double layers are much thinner than the radius of the droplet and the calculated deformation converges to the leaky dielectric result. In between these two limits, an S-curve is described, similar to that seen for Henry's function in electrophoresis.

The electrokinetic result may not be able to explain all the remaining discrepancies between theory and experiment. Most experiments with dielectric drops in electric fields are done for relatively large drops, on the millimeter scale. Even in inorganic solvents, the electrostatic double layer can easily be on the scale of microns. However, this is not always the case; some of the parameter sets in Feng (1999) give rise to predicted double layer thicknesses as large as half the drop radius. In addition, this theory provides an important understanding of the roles played by the two limiting theories, and may find application in microfluidic devices in which the length scale of the ion layer is important.

2.5 Summary

Analysis of the deforming droplet problem to date has been extensive, and several aspects of the problem have been studied. However, studies of the dynamic response of this type of system are less common than steady-state analyses, and the important contributions due to finite conduction speed and charge convection have not yet been quantified in the context of a dynamic model. In addition, knowledge of the dynamic modes of large-deformation instability appears to be incomplete with respect to the leaky dielectric model, particularly when the aforementioned boundary charge dynamics are considered. There have been no attempts known by this researcher to numerically model a general electrokinetic system like that of Zholkovskij et al. (2002).

The objective of this study is to model the dynamic response of a droplet deforming in an electric field, for both perfect and leaky dielectric cases, and including the effects of finite conduction and convection of boundary charge. Large deformations are modeled, up to the point of breakup if the system is unstable. Modeling of droplet fragmentation is not attempted. The analysis is axisymmetric, which excludes the possibility of modeling electrorotation, and the full electrokinetic problem is left for a future study.

CHAPTER 3

THEORY AND NUMERICAL FORMULATION

3.1 System Description

The system under consideration is shown in Figure 3.1. It consists of a single liquid droplet suspended in a continuous phase, effectively infinite in extent, with the two fluids being immiscible. This results in a sharp interface between the two fluids. The free stream velocity, far from the droplet, is uniformly zero. Interfacial tension yields a pressure discontinuity across the interface proportional to the local mean curvature, such that the pressure is higher inside the droplet than outside it. For small droplets, the internal pressure can be very large. Any deformation of the droplet from the spherical shape is resisted by the interfacial tension.

An electric field $\vec{E}_0$ is applied to this system in order to deform it. This field is uniform far from the domain of interest. However, if the electrical properties of the two fluids differ, the field will distort in the vicinity of the droplet, and Maxwell electrical stresses will arise.

The Maxwell stress has two components: first, there is the polarization stress that occurs due to the difference in the dielectric permittivities, ϵ_i and ϵ_e, of the two fluids. If the problem is treated as electrostatic, this stress is the only one involved in the perfect dielectric case. It is localized at the interface of the droplet, where the

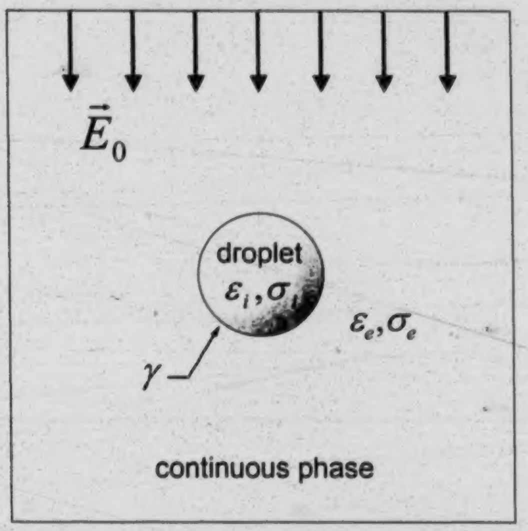

Figure 3.1: A liquid droplet suspended in a second fluid in the presence of an electric field, $\vec{E}_0$. The electrical properties of the two fluids differ, and there is a positive tension at the interface between them.

permittivity is discontinuous. It can be shown that the polarization stress is always normal to the interface, and if no other stresses are present, it always produces a prolate deformed shape; that is, the droplet stretches parallel to the electric field [O'Konski and Thacher, 1953].

The second component of the electrical stress is the body force due to nonzero net free charge density at a point in the bulk fluid. This force depends on the conductivities σ_i and σ_e, and is caused by a nonzero concentration of free charge carriers (such as ions) in one or both fluids, allowing free charge to build up near the droplet. If the conductivities are relatively high, or the droplet is relatively large, it can be assumed that the charge carriers build up only in a thin layer on the interface. This reduces the total Maxwell stress to a boundary condition, and is one of the assumptions made by Taylor (1966). Unlike the polarization stress, this effect is not necessarily normal to the interface. It can produce steady-state circulating flows, and, depending on the parameters, can produce an oblately deformed droplet: one that is squashed in the axis parallel to the applied field.

The deformation of the droplet in the time domain is the result of interactions between electrical stresses, interfacial tension, and inertial and viscous forces in both fluids. The fluid mechanics problem is driven by the electrical stresses, and the interfacial tension and viscous stresses resist the resulting motion. Since the solution to the electrical problem depends on the geometry of the droplet, and any ions present may be convected by the flow, it can be seen that there is a two-way coupling between the electrical and fluid mechanical problems.

3.2 Validity of Electrostatic Assumption in Analysis of Electromagnetic Subproblem

The electrical description of the suspended droplet system depicted in Figure 1.1 can be accomplished in general by considering the Maxwell equations of electromagnetics in polarizable media [Smythe, 1968]. The description of electromagnetic phenomena given by Maxwell's equations is complicated in that it involves the solution of four coupled vector partial differential equations, for a total of six equations in 2D or eight in 3D. However, if the time scale of interest is much longer than the electromagnetic relaxation time, the problem can be treated as quasi-static, so that the electric and magnetic fields are decoupled [Saville, 1997].

The time scale of interest in this case is that of the droplet oscillation. An approximation to the n$^{\text{th}}$ resonant frequency ω_n of a suspended fluid drop with zero viscosity is given by Whitaker et al. (1998):

$$\omega_n^2 = \frac{(n-1)n(n+1)(n+2)}{n\rho_e + (n+1)\rho_i} \frac{\gamma}{R_0^3} \tag{3.1}$$

in which ρ_i and ρ_e are the internal (droplet) and external (continuous phase) fluid densities, respectively, γ is the interfacial tension, and R_0 is the undeformed radius of the droplet.

The squash/stretch mode corresponds to the $n = 2$ harmonic, which is the lowest-order harmonic possible in an incompressible droplet under zero net force [Basaran, 1992]. Since this study deals entirely with step responses, the fundamental harmonic is dominant and we can use $n = 2$ to simplify the above expression. The resulting time scale τ is as follows:

$$\tau = \sqrt{\frac{(2\rho_e + 3\rho_i)R_0^3}{24\gamma}} \tag{3.2}$$

In problems of the type studied here, the droplet radius R_0 typically varies from 10^{-3} to 10^{-6} metres. For densities similar to that of water or oil, with a high interfacial tension approaching the water/air interface value of 0.07 N/m, the time scale given by Equation 3.2 is of order 10^{-3} and 10^{-7} seconds respectively for these two length scales. Smaller values of γ result in a slower system.

The characteristic time scale τ_m for magnetic coupling effects is given by Saville (1997) as:

$$\tau_m = \mu_r \mu_0 \sigma l^2 \tag{3.3}$$

where l is a characteristic length, $\mu_r \mu_0$ is the magnetic permeability of the fluid (typically $\mu_r \simeq 1$ for non-magnetic fluids), and σ is the conductivity. In this case, the length scale in Equation 3.3 can be taken as the radius of the droplet, or between 10^{-3} and 10^{-6} m. This yields a time scale for magnetic phenomena between $10^{-10}\sigma$ and $10^{-18}\sigma$ seconds, which can be matched to the fluid time scale by appropriately large values of the conductivity. The minimum required conductivity is 10^7 S/m, which is physically impossible, no matter what electrolyte is used (see Equation 3.5 below). Even mercury, which is not studied here, only has a conductivity of approximately

10^6 S/m [CRC, 2004]. Therefore, within the parameters given, the fluid time scale is long enough to permit the use of the electrostatic assumption.

Another problem of interest occurs on the time scale of charge buildup due to inhomogeneous conduction. The characteristic time scale for conductive phenomena, τ_e, is given by Saville (1997) as:

$$\tau_e = \epsilon_r \epsilon_0 / \sigma \tag{3.4}$$

where $\epsilon_r \epsilon_0$ is the electric permittivity of the fluid. If the conduction effects are to be magnetically independent, the condition $\epsilon_r \epsilon_0 / \sigma \gg \mu_r \mu_0 \sigma l^2$ must be met. For non-ferromagnetic materials in which the relative permeability $\mu_r \simeq 1$, and assuming the permittivity of vacuum, or $\epsilon_r = 1$, this reduces to $7.046 \times 10^{-6} \gg \sigma^2 l^2$. For a 1 mm droplet, $\sigma \ll 3$ S/m satisfies this criterion, and the limit on σ only rises as l shrinks.

The concentration of ions required to yield a conductivity of 3 S/m can be calculated from the following [Masliyah, 1994]:

$$\sigma = \frac{\mathcal{F}^2 \sum (z^k)^2 c^k D^k}{RT} \tag{3.5}$$

$\mathcal{F}$ is Faraday's constant, and R is the universal gas constant. Using an ionic valence z^k of ±1, a typical diffusion coefficient D^k of 10^{-9} m^2/s [CRC, 2004] for both ion species, and a system temperature of 298 K, we find that a conductivity of 3 S/m results from a solute concentration of 399 mol/m^3, or 0.4 M. A solution this concentrated can certainly exist, but the study of leaky dielectrics usually deals with significantly more dilute electrolytes.

Comparing Equation 3.4 to Equations 3.2 and 3.3, it may be seen that if the conductivity is high enough to produce a significant electromagnetic coupling, both the electric and magnetic time scales are very much faster than the fluid mechanics. While electrostatic analysis of the conduction transients is not possible under these circumstances, the steady-state should be decoupled sufficiently for the electrostatic assumption to be valid in the range of the droplet oscillation time scale. This allows the use of an electrostatics solution to drive the fluid mechanics problem.

3.3 Range of Validity of the Leaky Dielectric Model

In a conductive system, nonzero net free charge can accumulate near interfaces between fluids. The leaky dielectric model [Melcher and Taylor, 1969] treats this accumulation as a boundary effect. For this treatment to be accurate, the thickness of the electrostatic double layer (the region near the interface in which ion concentrations differ substantially from their far-field values) must be significantly less than the characteristic length scale of the system.

The assumption of thin electrostatic double layers which characterizes the leaky dielectric model can be validated in this case by calculating the thickness of the double layer and comparing it with the droplet radius R_0. The double layer thickness for a given system is the Debye length κ^{-1} [Masliyah, 1994]:

$$\kappa^{-1} = \sqrt{\frac{\epsilon_0 \epsilon_r RT}{\mathcal{F}^2 \sum_k (z^k)^2 c^k}} \tag{3.6}$$

Given a small droplet 10^{-6} m in radius, a Debye length of $\kappa^{-1} = 10^{-6}$ m represents a double layer on the same scale as the droplet. For a droplet with $\epsilon_r = 80$ at a temperature of 298 K, containing a monovalent electrolyte ($z = \pm 1$), the required ionic concentration is approximately 10^{-8} M. For lower ϵ_r, a more dilute solution is required to produce the same κ^{-1}.

The conductive time scale for this case can be calculated from Equations 3.4 and 3.5, for comparison with the drop oscillation time calculated from Equation 3.2. A monovalent ion concentration of 10^{-8} M (10^{-5} mol/m^3), with a diffusion coefficient of 10^{-9} m^2/s, yields a conductivity on the order of 10^{-7} S/m, leading to a conduction time scale of approximately 10^{-2} s, or 10^4 times the droplet oscillation time scale.

Since the double layer thickness scales with $(c^k)^{-1/2}$, a drop on the scale of 10^{-3} m rather than 10^{-6} m would require a concentration 10^6 times smaller to maintain the same double layer thickness relative to the drop size. This increases the conduction time scale from 10 ms to almost three hours, and is probably not physically realizable with most fluids and experimental setups.

On the scale of the smaller droplets (10^{-6} m), it is physically reasonable to consider finite double layer thickness. However, the conduction time scale in cases where the double layer thickness is important is much larger than the droplet oscillation time. In cases with such widely disparate time scales, standard finite element formulations are difficult to solve, and special measures become necessary. Such measures are beyond the scope of this work.

3.4 Governing Equations

In order to describe the coupled electrical/fluid mechanical system in Figure 3.1, governing equations describing the electrical problem and the fluid mechanics problem are necessary. This study uses the Poisson equation for electrostatics, simplified to the Laplace equation for the limiting cases considered, and the incompressible Navier-Stokes equations for the fluid mechanics.

3.4.1 Electrostatic Equations

It is evident from Section 3.2 that electromagnetic coupling can be safely neglected for most problems of the type studied here. Since the problem of interest is much slower than the magnetic time scale, and no significant external magnetic excitation is present, we can use the electrostatic equations for a polarizable medium [Landau and Lifshitz, 1960]:

$$\nabla \times \vec{E} = 0 \tag{3.7}$$

and

$$\nabla \cdot \vec{D} = \nabla \cdot (\epsilon_0 \vec{E} + \vec{P}) = \rho_f \tag{3.8}$$

in which $\vec{E}$ is the local electric field at a point, $\vec{D}$ is the electric displacement, $\vec{P}$ is the electric polarization of the material, and ρ_f is the free charge density.

Most fluids of interest in the suspended droplet problem can be considered as isotropic linear dielectrics. This is assumed in the first paper in which this problem is treated [O'Konski and Thacher, 1953] and all known subsequent works on the subject. If it is assumed that the material being described is an isotropic linear dielectric, the polarization $\vec{P}$ is described by

$$\vec{P} = (\epsilon_r - 1)\epsilon_0 \vec{E} \tag{3.9}$$

and Equation 3.8 becomes:

$$\nabla \cdot (\epsilon_r \epsilon_0 \vec{E}) = \rho_f \tag{3.10}$$

It is well known that if $\vec{E}$ is treated as the gradient of a scalar potential, Equation 3.7 is automatically satisfied. The scalar potential typically used is Ψ, the electric potential, representing energy per unit charge, such that $\vec{E} = -\nabla\Psi$. Equations 3.7 and 3.10 can thus be condensed into a single scalar potential equation, the Poisson equation:

$$\nabla^2(\epsilon_r \epsilon_0 \Psi) = -\rho_f \tag{3.11}$$

In the general case, ρ_f represents the net free charge density, or imbalance in ionic strength, at a point in the bulk fluid.

In the case where the medium of interest is a perfect dielectric, no current can flow and free charge is absent. This means that the net free charge density is zero everywhere, giving rise to the Laplace equation:

$$\nabla^2(\epsilon_r\epsilon_0\Psi) = 0 \tag{3.12}$$

Since there is only one variable in this equation, no further descriptor equations are required, and one can solve for the electric potential Ψ on any geometry with an appropriate set of boundary conditions.

In the case of Taylor's leaky dielectric model [Melcher and Taylor, 1969], ion diffusion is ignored, and the electrostatic double layer is assumed to be very thin relative to the geometry in question. This reduces the net free charge to a boundary condition, and once again ρ_f is zero in the bulk fluid.

There are two ways in which the boundary charge layer may be described. The most general form is an explicit treatment, where conduction and convection of charge carriers are modeled directly. If the charge on the boundary is treated explicitly, Equation 3.12 is used in the bulk. However, if the boundary charge is assumed to be in static equilibrium, the Laplace equation may be written as follows, in accordance with the principle of continuity of current:

$$\nabla^2(\sigma\Psi) = 0 \tag{3.13}$$

Here σ is the local conductivity of the fluid, which is uniform in each phase. This formulation allows a natural interfacial boundary description, in which the surface charge density is dealt with implicitly by the use of a Neumann continuity condition. This will be described in Section 3.5.2.

3.4.2 Fluid Mechanics

The fluid mechanical problem is described using the incompressible Navier-Stokes equations [Batchelor, 1967]:

$$\begin{gathered}\rho\frac{\partial\vec{v}}{\partial t}-\nabla\cdot\mu(\nabla\vec{v}+(\nabla\vec{v})^T)+\rho(\vec{v}\cdot\nabla)\vec{v}+\nabla p=\vec{f_b}\\ \nabla\cdot\vec{v}=0\end{gathered}\tag{3.14}$$

If the fluid is assumed to be Newtonian, μ may be treated as a scalar constant. Since the droplets under consideration are very small, gravity is assumed to be negligible. This follows O'Konski & Thacher (1953), Allan & Mason (1962), Taylor (1966), and Zholkovskij et al. (2002), none of whom consider the effects of gravity in their theories. As noted in section 3.5.2, without free charge, the expression for electrical force becomes a boundary expression only, so that no significant body forces are present and the right-hand-side term $\vec{f_b}$ in Equation 3.14 becomes zero. The flow in both the perfect and leaky dielectric cases is thus driven entirely by the boundary conditions.

3.5 Boundary Conditions

3.5.1 Far-Field Conditions

Figure 3.1 depicts a droplet suspended in an infinite stationary medium and subject to a uniform applied electric field. The corresponding far-field boundary condition formulation is:

$$\nabla\Psi = -\vec{E}_0 \quad \text{at infinity} \tag{3.15a}$$

$$-p\bar{\bar{I}}+\mu(\nabla\vec{v}+(\nabla\vec{v})^T) = \bar{\bar{0}} \quad \text{at infinity} \tag{3.15b}$$

where $\bar{\bar{I}}$ is the identity tensor and $\bar{\bar{0}}$ is the null tensor.

Equation 3.15a represents the application of a defined uniform electric field $\vec{E}_0$ far from the drop. Any perturbation in the field due to the presence of the drop becomes vanishingly small as the distance from the drop becomes large.

Equation 3.15b maintains the total fluid stress in the far field at zero. This condition is an expression of far-field uniformity in the fluid solution. In this case, the electrical problem is also uniform in the far field, and thus no body forces are expected there. Hence Equation 3.15b, given zero initial conditions for pressure and velocity, will tend to maintain quiescence in the far field.

3.5.2 Conditions at the Interface Between the Drop and Continuous Phase

Electrostatics

In the electrical problem, considering the perfect dielectric case, the drop interface is described by continuity of potential and of electric displacement. Accordingly, following Zholkovskij et al. (2002), the boundary conditions for this case are:

$$\Psi_i = \Psi_e \quad \text{at interface} \tag{3.16a}$$

$$\sum_{j=i,e}[\nabla(\epsilon_{r,j}\Psi_j)\cdot\hat{n}_j] = 0 \quad \text{at interface} \tag{3.16b}$$

where i and e signify variables in the internal and external fluids respectively, and $\hat{n}_j$ is the outward unit normal from each domain into the other.

Equation 3.16a represents continuity of electric potential. Equation 3.16b represents continuity of electric displacement, and is the appropriate boundary condition at a clean interface between two uniform, isotropic perfect dielectrics with different values of ϵ_r.

In the leaky dielectric case, a layer of ions builds up on the interface, and the displacement condition takes a different form. For simplicity, once again following Zholkovskij et al. (2002), it is assumed that no solute adsorbs on the interface, so that the ion layer is due to electrical effects. Since the surface charge density q represents a discontinuity in electric displacement, the corresponding boundary condition can be written in either the general form

$$\sum_{j=i,e}[\nabla(\epsilon_j \Psi_j) \cdot \hat{n}_j] = q \tag{3.17}$$

or the static equilibrium form

$$\sum_{j=i,e}[\nabla(\sigma_j \Psi_j) \cdot \hat{n}_j] = 0 \tag{3.18}$$

which specifies continuity of current. If convection/diffusion are taken into account, or if the time scale of charge migration is important, the first form must be used. This necessitates an extra equation to describe the dynamics of charge transport to and from the boundary. Saville (1997) gives:

$$\frac{\partial q}{\partial t} + \vec{v} \cdot \nabla_s q = q\hat{n} \cdot (\hat{n} \cdot \nabla)\vec{v} - ||\sigma \vec{E}|| \cdot \hat{n} \tag{3.19}$$

where the use of $|| \cdots ||$ indicates the jump from inside to outside, $\hat{n}$ is the outward normal in that direction, and ∇_s is the tangential or surface gradient. The second term on the left is the convective flux along the boundary, and the first term on the right is the change in concentration due to dilation of the interface; this can be seen by considering the incompressibility condition. The term on the far right is the current discontinuity, or charge buildup due to migration.

Interfacial Stresses

The deformation of the droplet under an applied electric field is caused by electrically-induced surface and body forces. Saville (1997) gives the net Maxwell stress $\bar{\bar{\sigma}}^M \cdot \hat{n}$ at an interface as:

$$\begin{aligned}
\left[\bar{\bar{\sigma}}^M \cdot \hat{n}\right] \cdot \hat{n} &= \frac{\epsilon_0}{2} || \epsilon_r (\vec{E} \cdot \hat{n})^2 - \epsilon_r (\vec{E} \cdot \hat{t}_1)^2 - \epsilon_r (\vec{E} \cdot \hat{t}_2)^2 || \qquad (3.20a)\\
\left[\bar{\bar{\sigma}}^M \cdot \hat{n}\right] \cdot \hat{t}_i &= q \vec{E} \cdot \hat{t}_i \qquad (3.20b)
\end{aligned}$$

where $\vec{t}_i$ are orthogonal unit tangents.

Another form of Equation 3.20a is given by Zholkovskij et al. (2002) for the complete normal interfacial stress balance:

$$\begin{aligned}
&\frac{\epsilon_0}{2} \{ \epsilon_e (\nabla \Psi_e \cdot \hat{n})^2 - \epsilon_i (\nabla \Psi_i \cdot \hat{n})^2 - (\epsilon_e - \epsilon_i) [(\nabla \Psi_i)^2 - (\nabla \Psi_i \cdot \hat{n})^2] \} \\
&-(p_e - p_i) + \{ \mu_e [\nabla \vec{v}_e + (\nabla \vec{v}_e)^T] \cdot \hat{n} - \mu_i [\nabla \vec{v}_i + (\nabla \vec{v}_i)^T] \cdot \hat{n} \} \cdot \hat{n} = -2\gamma X \qquad (3.21)
\end{aligned}$$

The terms including $\nabla \vec{v}$ are normal viscous stresses from the Navier-Stokes solution, p_i and p_e are fluid pressures on either side of the interface, and $2\gamma X$ is the Young-Laplace pressure from interfacial tension (γ) where X is the mean interface curvature. It should be noted that Equation 3.21 uses the convention that mean curvature is concave-positive, convex-negative.

From Pythagoras' theorem, $\epsilon_r (\vec{E} \cdot \hat{t}_1)^2 + \epsilon_r (\vec{E} \cdot \hat{t}_2)^2 = \epsilon_r |\vec{E}|^2 - \epsilon_r (\vec{E} \cdot \hat{n})^2$. Also, since $\Psi_i \equiv \Psi_e$ on the boundary, it is necessary that $\vec{E}_i \cdot \hat{t} = \vec{E}_e \cdot \hat{t}$. From this, the terms involving the electric field ($-\nabla \Psi$) in Equation 3.21 can be seen to constitute an equivalent expression to Equation 3.20a.

The tangential Maxwell stress depends on the surface charge, and is thus absent in the perfect dielectric case. It is also absent in the general electrokinetic problem, since adsorption is neglected and the net free charge is treated as a volumetric effect

[Zholkovskij et al., 2002]. In the leaky dielectric case, if surface charge is not present explicitly in the electrical continuity condition at the interface, it must be calculated based on the behaviour of the electric field, using Equation 3.17. The resulting complete expression for tangential stress is as follows:

$$\epsilon_0[\epsilon_e \nabla\Psi_e \cdot \hat{n} - \epsilon_i \nabla\Psi_i \cdot \hat{n}]\nabla\Psi_i \cdot t_i + \{\mu_e[\nabla\vec{v}_e + (\nabla\vec{v}_e)^T]\cdot\hat{n} - \mu_i[\nabla\vec{v}_i + (\nabla\vec{v}_i)^T]\cdot\hat{n}\}\cdot\hat{t}_i = 0 \quad (3.22)$$

The leaky dielectric model contains no electrical body forces. In the general problem, nonzero net free charge density leads to an electric body force $\rho_f \vec{E}$ in the bulk fluid, but this is not present in either the perfect or leaky dielectric limiting cases.

In the case of a uniform, isotropic linear dielectric with no net free charge in the bulk, electrical stress occurs only at a boundary. Neglecting secondary body forces such as gravity, the treatment of interfacial stress given by Equations 3.21 and 3.22 is thus sufficient to describe both limiting cases.

Fluid Mechanics

The interfacial boundary conditions for the fluid problem represent continuity of velocity and a discontinuity in total stress caused by electrical and surface tension loading:

$$\vec{v}_i = \vec{v}_e \qquad \text{at interface} \quad (3.23a)$$

$$\mu_i(\nabla\vec{v}_i + (\nabla\vec{v}_i)^T)\cdot\hat{n} - \mu_e(\nabla\vec{v}_e + (\nabla\vec{v}_e)^T)\cdot\hat{n} - p_i + p_e = \vec{S}_n \qquad \text{at interface} \quad (3.23b)$$

This last condition prescribes a jump $\vec{S}_n$ in the total fluid stress. It is a restatement of Equations 3.21 and 3.22, and the jump represents the combination of electrical and interfacial tension surface stresses:

$$\vec{S}_n \cdot \hat{n} = \frac{\epsilon_0}{2}(\epsilon_e(\vec{E}_e \cdot \hat{n})^2 - \epsilon_i(\vec{E}_i \cdot \hat{n})^2 - (\epsilon_e - \epsilon_i)(E_{r_i}^2 + E_{z_i}^2 - \vec{E}_i \cdot \hat{n}^2)) + 2\gamma X \tag{3.24a}$$

$$\vec{S}_n \cdot \hat{t}_i = -\epsilon_0 \vec{E} \cdot \hat{t}_i(\epsilon_i \vec{E}_i \cdot \hat{n} - \epsilon_e \vec{E}_e \cdot \hat{n}) \tag{3.24b}$$

3.5.3 Initial Conditions

The present problem is being studied in the context of its response to a step change in the electric field. Prior to the application of $\vec{E}_0$ at $t = 0$, it is assumed that no electric field is present. Other situations besides the electric field step can be modeled, such as oscillation resulting from a nonspherical initial shape, but in all such cases the problem is assumed to be stationary and locally electroneutral at $t = 0$.

The interfacial tension effect on a spherical droplet produces a static pressure rise inside the droplet due to the uniform mean curvature of the interface. This pressure can be expressed using the Young-Laplace equation, as in Equation 3.21, employing the reciprocal of the droplet radius as the mean curvature. It is necessary to take this pressure into account in the present problem.

The resulting initial conditions are expressed as follows:

$$\vec{v} = 0 \quad \text{and} \quad p = 0 \qquad \text{in continuous phase} \tag{3.25a}$$

$$\vec{v} = 0 \quad \text{and} \quad p = \frac{2\gamma}{R_0} \qquad \text{in droplet} \tag{3.25b}$$

$$q = 0 \quad \text{on interface} \tag{3.25c}$$

Equations 3.25a and 3.25b specify quiescence of both fluids over the entire domain, with the additional Young-Laplace pressure present inside the droplet. It is not necessary to specify an initial condition for the electric field, since the Laplace equation is static. However, in the leaky dielectric case, local electroneutrality must be enforced at $t = 0$, and Equation 3.25c corresponds to this condition.

Actually, since the fluid is incompressible, the initial pressure difference can be subtracted from the interfacial stress boundary condition given by Equation 3.24a without affecting the solution. If this is done, the pressure difference should also be absent from the initial condition, and Equation 3.25a can be used over the whole domain. This is done in the finite element implementation and leads to improved numerical conditioning.

To summarize, the descriptor equations and corresponding initial and boundary conditions for the perfect and leaky dielectric limiting cases have been obtained. The equations to be solved in the perfect dielectric case are given by Equation 3.12 and 3.14, subject to boundary conditions given by Equations 3.15, 3.16, and 3.23 along with Equations 3.24. In the leaky dielectric case, there are two possibilities: if the charge on the boundary is considered to be in static equilibrium, Equation 3.12 is replaced with 3.13, and Equation 3.16b is replaced with Equation 3.18. If boundary charge is to be tracked in the time domain, Equation 3.16b is replaced with Equation 3.17 combined with Equation 3.19, and all other equations remain the same. Initial conditions for the problem as stated are given by Equations 3.25. However, in order to stabilize the numerical result, without loss of accuracy Equation 3.25b is replaced with Equation 3.25a, and the initial value of the interfacial tension stress is subtracted from Equation 3.24a.

3.6 Nondimensionalization of Governing Equations

In order to scale the problem appropriately so as to allow numerical solution without ill-conditioning, the equations describing the system are nondimensionalized. The electrostatics problem is normalized as follows:

$$\vec{E}^* = \frac{\vec{E}}{E_0}, \qquad V^* = \frac{\Psi}{E_0 R_0}, \qquad q^* = \frac{q}{E_0 \epsilon_0} \tag{3.26}$$

where $\vec{E}^*$, V^*, and q^* are the nondimensional field, potential, and charge, respectively.

The Navier-Stokes equations are nondimensionalized as follows:

$$\frac{Q}{St}\frac{\partial \vec{v}^*}{\partial t^*} - \bar{\nabla} \cdot \frac{Q}{Re}(\bar{\nabla}\vec{v}^* + (\bar{\nabla}\vec{v}^*)^T) + Q(\vec{v}^* \cdot \bar{\nabla})\vec{v}^* + \bar{\nabla} p^* = 0 \tag{3.27}$$

$$\bar{\nabla} \cdot \vec{v}^* = 0$$

$$(r^*, z^*) = \frac{(r, z)}{R_0}, \quad t^* = \frac{t}{\tau}, \quad p^* = \frac{p}{p_0}, \quad \vec{v}^* = \frac{\vec{v}}{v_0} \tag{3.28a}$$

$$\text{and} \quad Q = \frac{\rho v_0^2}{p_0}, \quad St = \frac{\tau v_0}{R_0}, \quad Re = \frac{\rho v_0 R_0}{\mu} \tag{3.28b}$$

$$\text{where} \quad \tau = \sqrt{\frac{(2\rho_e + 3\rho_i)R_0^3}{24\gamma}}, \quad p_0 = \epsilon_0 E_0^2 \left(\epsilon_e - \frac{\epsilon_e^2}{\epsilon_i}\right), \quad v_0 = \frac{2R_0 d_t}{\tau} \tag{3.28c}$$

St is the Strouhal number, *Q* is the Ruark number, and *Re* is the Reynolds number. $\bar{\nabla}$ is the nondimensional gradient computed on the normalized geometry.

Following Whitaker et al. (1998), the time scale τ in Equations 3.28c is the characteristic time of oscillation for an inviscid droplet with the given parameters. Since it is the inverse of the natural frequency ω_2 [rad/s], this characteristic time scale is in s/rad, which means that the nondimensionalized time t^* of Equations 3.28a is in units of radians. 2π radians indicates one complete cycle of oscillation of the drop.

The characteristic pressure p_0 is the pressure that would occur at a flat interface between the two fluids under study if it were subject to a perpendicular field E_0 in the absence of free charge. The theoretical deformation parameter d_t is calculated from the appropriate analytic result in Chapter 2. The characteristic velocity v_0 is an estimate of how fast the pole ($r = 0,\ z = b$) of the droplet would have to travel to go from a spherical shape to the deformed shape corresponding to d_t in the calculated characteristic time τ.

3.7 Numerical Implementation

Finite element modeling of the deforming droplet system was done using the commercial software package FEMLAB, version 2.3b [COMSOL, 2002]. This software allows problem input in the form of a partial differential equation, which makes it a flexible multiphysics package. A small selection of general-purpose elements is available, and user-defined elements are also possible.

The deforming droplet problem as studied in the present work is a combination of electrostatics and hydrodynamics, and was solved using first- and second-order triangular Lagrange elements. On a Lagrange element, mapping of the equation variables to the element nodes occurs via shape functions which are polynomials of degree equal to the element order. The first-order element has nodes at the vertices of the triangle, and the shape functions are linear. The second-order element has additional degrees of freedom midway along each side, for a total of six, and the shape functions are quadratic.

Following the Navier-Stokes implementation in FEMLAB's Chemical Engineering Module, first-order elements were used for pressure. This avoids numerical well-posedness problems [Feng and Scott, 1996]. All other variables were solved on second-order Lagrange elements.

FEMLAB uses Galerkin's method to map an arbitrary partial differential equation to the finite element space. The input can be in any of these three different formats: the coefficient form, the general form, and the weak form. The coefficient form is broken up into recognizable components, such as diffusion, convection, reaction and so forth, and is unsuitable for highly nonlinear problems due to simplifying assumptions made during setup of the matrices. The general form allows freeform input, is more robust with respect to nonlinearities and is adequate for most problems. The weak form is the Galerkin integral formulation itself, and allows solution of the most general class of problems.

For this problem, the general form was used. FEMLAB's general formulation is as follows:

$$\mathbf{d_a}\frac{\partial \mathbf{u}}{\partial t} + \bar{\nabla} \cdot \mathbf{\Gamma} = \mathbf{F} \tag{3.29}$$

in which $\mathbf{d_a}$, $\mathbf{\Gamma}$ and $\mathbf{F}$ are arbitrary functions of the equation variables $\mathbf{u}$ and their derivatives. The variable list $\mathbf{u}$ is a row vector, and $\mathbf{F}$ is a column vector with each row corresponding to a single equation in the system of equations being described. $\mathbf{\Gamma}$ is a matrix with columns corresponding to the space dimensions of the problem, and $\mathbf{d_a}$ is a square matrix with size equal to the number of equations in the system.

Boundary conditions for the general form are defined as paired Dirichlet and Neumann conditions, with a Lagrange multiplier term serving as a switch. The formulation is as follows:

$$\sum(-\hat{n} \cdot \mathbf{\Gamma}) = \mathbf{G} + \left(\frac{\partial \mathbf{R}}{\partial \mathbf{u}}\right)^T \boldsymbol{\mu} \tag{3.30a}$$

$$\mathbf{R} = 0 \tag{3.30b}$$

where $\mathbf{G}$ is the Neumann condition and $\mathbf{R}$ is the Dirichlet condition. The set of unknown or dependent variables is denoted by $\mathbf{u}$, and $\boldsymbol{\mu}$ is a vector of Lagrange multipliers. $\mathbf{\Gamma}$ is the flux term from the general PDE formulation described by Equation 3.29. The normal $\hat{n}$ is outward from each domain into the other. **G**, **R**, and $\boldsymbol{\mu}$ are column vectors.

From this description it can be seen that since the Lagrange multipliers are free, the presence of a Dirichlet condition will normally render the Neumann condition ineffective. In this case, the loads resulting from the Dirichlet constraint may be recovered from the Lagrange multipliers. If, however, the Dirichlet term **R** is zero, or does not depend on the equation variables, the Lagrange multiplier is cancelled and the Neumann condition takes effect.

If variables from more than one equation are used in a Dirichlet condition, the Lagrange multipliers may become defined, resulting in a double boundary condition. In the present problem this effect occurs only in the fluid mechanics, where it assists in the application of the correct boundary conditions at the interface. This is detailed in Section 3.7.5.

3.7.1 Computational Problem Domain

Figure 3.2 shows the geometry used in the numerical solution. The deforming droplet system in Figure 3.1 is assumed to be symmetric with respect to the polar axis of the droplet, parallel to the electric field. It is possible for non-axisymmetric instabilities to arise under oscillatory electrical excitation [Azuma and Yoshihara, 1999]. However, in experiments that do not attempt specifically to excite these high-order modes, any non-axisymmetric behaviour appears primarily as an artifact, irrelevant to the general character of the observed behaviour [Allan and Mason, 1962, Torza et al., 1971, Tsukada et al., 1993, Eow et al., 2001]. An exception to this is electrorotation of leaky dielectric drops within certain parameter ranges, as discussed by Feng (2002). This effect is difficult to treat, as it does not permit any reduction of the general three-dimensional problem, and no corresponding three-

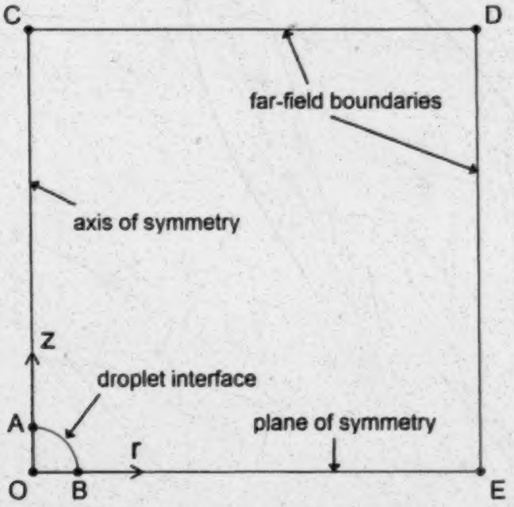

Figure 3.2: Two-dimensional axisymmetric geometry for the numerical solution.

dimensional analytic result is known. The present work does not attempt to model electrorotation. The seminal analytic studies, and most numerical investigations [Sherwood, 1988, Tsukada et al., 1993, Feng and Scott, 1996, Hirata et al., 2000] use an axisymmetric description.

In the present work, it is further assumed that the fluid mechanics obeys symmetry across the equatorial plane of the droplet, and that the electrical problem follows a form of antisymmetry whereby opposite charges fulfill the same roles on opposite sides of the equator. This allows the problem domain to be further reduced, so that modeling takes place on only one hemisphere of the droplet, and eliminates the possibility of drifting of the droplet's centre of mass. As with axial symmetry, equatorial symmetry is not guaranteed in the physical system [Feng and Scott, 1996], but the purpose of this study is not to observe high-order forced oscillations or charged-drop migration, and the computational savings involved in this truncation are considerable.

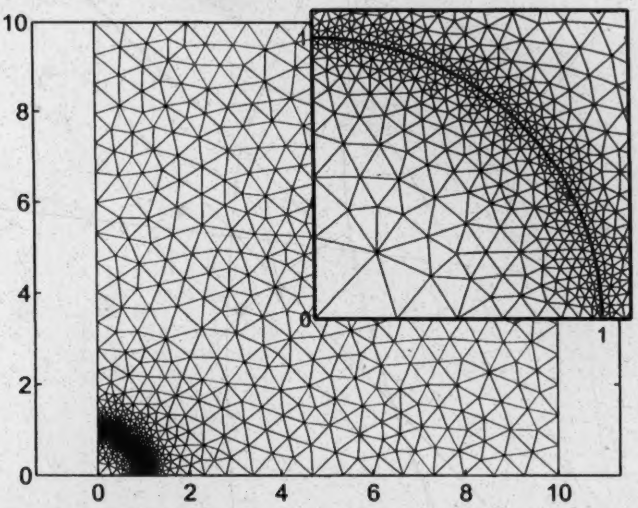

Figure 3.3: Typical meshed geometry. Dimensions are scaled with respect to the drop radius. The inset shows the details of the mesh near the droplet boundary.

Meshing of the computational domain is performed using a Delaunay triangulation algorithm [COMSOL, 2002], which generates an unstructured triangular mesh on the 2D problem domain. Figure 3.3 shows the problem mesh, with an inset detailing the refinement at the fluid interface. The number of elements in this problem is approximately 2000, due mostly to this interfacial refinement. Both the electrostatics problem and the fluid mechanics problem use the same geometry and mesh.

3.7.2 Dynamic Solution Structure

The finite element model is solved using a fixed time step method with a moving mesh. The method is multistage, and electrostatics is solved separately. Figure 3.4 details the steps involved in the method.

Parameter initialization is performed once at the beginning of the simulation, which then enters a loop containing the bulk of the processing. Fixed timestepping is used, and the simulation is stopped at a prespecified time. After the loop, the results

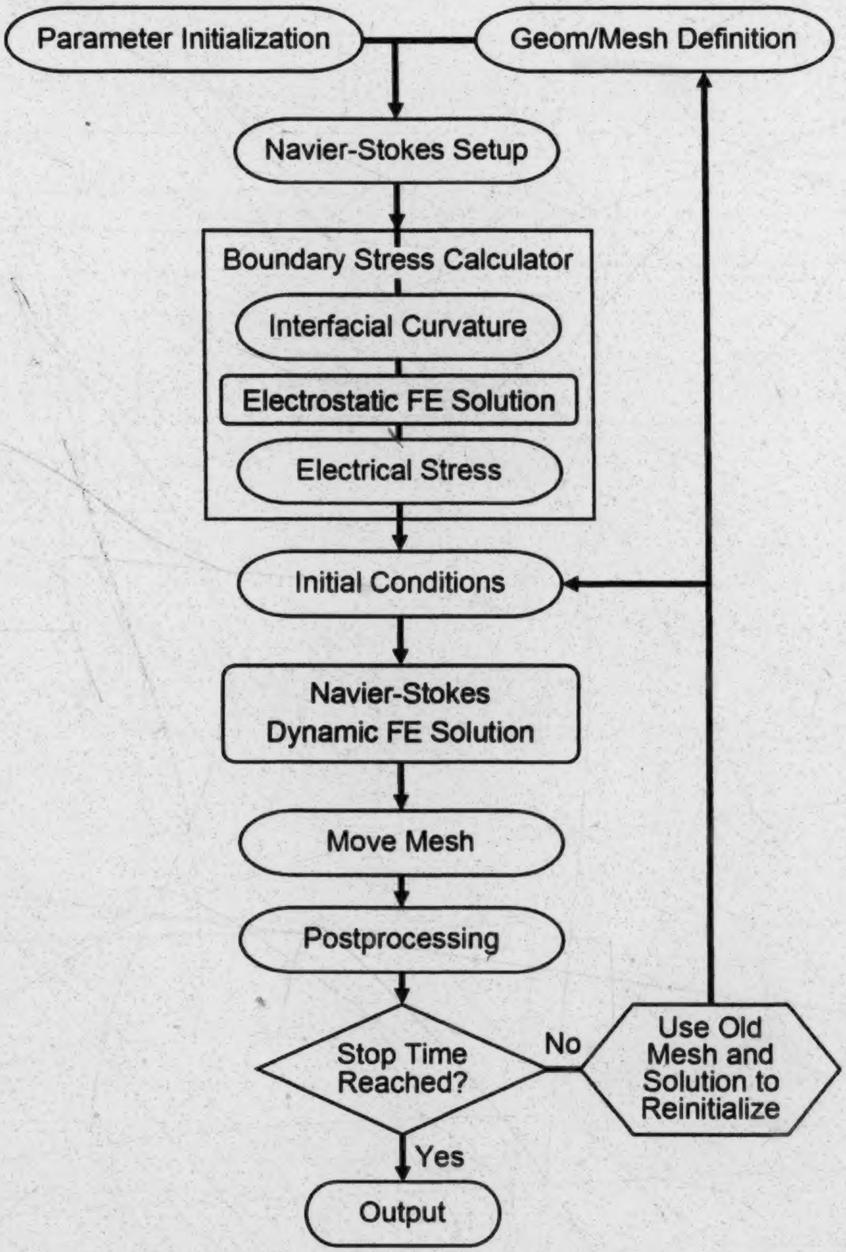

Figure 3.4: Structure of the dynamic finite element solution.

are plotted and the contents of the MATLAB workspace are saved to a file.

Each time step begins with the geometry definition. During the first time step, the geometry in Figure 3.2 is generated with FEMLAB primitives. For subsequent steps, the convected geometry from the previous step is used. Stepwise mesh motion allows approximation of the actual motion of the fluid interface, if the time step is small enough; this method is detailed in Section 3.7.6.

After (re)initialization of the geometry, the Navier-Stokes problem is defined, according to the formulation in Section 3.7.5. At this stage, in the first time step, the mesh is generated, and in subsequent steps the convected mesh from the previous step is analyzed and replaced if necessary. The Navier-Stokes setup includes equations and boundary conditions, as well as initial conditions for the first time step. In subsequent steps, the initial condition is derived from the solution at the end of the previous step, and is not defined until just before the solution stage.

The fluid mechanics, unlike the electrostatics, is not set up as a single equation over the whole domain. In order to allow a pressure discontinuity at the interface, separate Navier-Stokes problems are defined in the droplet and continuous phase, and appropriate continuity is maintained by coupling at the interfacial boundary.

After defining the fluid mechanics problem, it becomes necessary to obtain the numeric value of the variable used for the interfacial stress condition. The boundary stress calculator obtains the interfacial tension stress as in Section 3.7.4 and solves the electrostatics problem as in Section 3.7.3, using a static linear finite element solution. It then combines the interfacial tension stress with the electrical stress to produce a usable boundary condition.

Once the interfacial stress calculation has been completed, the initial conditions for the solution are defined. For the first time step, they are uniformly zero for all variables, and are calculated by FEMLAB from the initial conditions specified during the Navier-Stokes setup phase. In subsequent steps, the initial conditions are generated from the previous step's solution as in Section 3.7.7.

Solution of the fluid mechanics problem over one time step is done by FEMLAB's time-dependent solver framework, which uses the robust nonlinear solver DASPK [Brown et al., 1994] to traverse the time step. Since DASPK uses its own timestepping scheme to produce a high-order result, a midpoint solution is requested so as to allow second-order convection of the geometry. This allows larger time steps than would be possible with a zero- or first-order convection scheme.

DASPK takes several small backward Euler steps at the beginning of its run in order to obtain a consistent initial condition [Brown et al., 1998]. This provides smoothing of any artifacts that may be present after the previous time step's solution is remapped to the new geometry.

After the solution, the complete FEMLAB data structure is copied into two reference structures for mesh moving and reinitialization purposes. This is necessary because the main FEM structure itself is deleted and reinitialized at the beginning of the next time step. The mesh in one of the reference structures is moved based on the average velocity over the time step, according to the method in Section 3.7.6. The other reference structure is left as it is, and will be used for reinitialization of the solution.

During the rest of the postprocessing phase, the drop volume is checked, the deformation parameter is calculated, and important variables such as the deformation parameter are added to master data lists. The global simulation time is incremented, and program control proceeds to the beginning of the next time step. This process repeats until the global time reaches a preset stop point.

3.7.3 Electrostatics

The FEMLAB implementation of the electrostatic problem uses the general PDE formulation described by Equation 3.29. The Laplace equation in axisymmetric form is defined in FEMLAB as follows:

$$\mathbf{\Gamma} = \left[\begin{array}{cc} -r^{*}\epsilon_r \dfrac{\partial V^{*}}{\partial r^{*}} & -r^{*}\epsilon_r \dfrac{\partial V^{*}}{\partial z^{*}} \end{array} \right] \tag{3.31a}$$

$$\mathbf{F} = 0 \tag{3.31b}$$

$$\mathbf{d_a} = 0 \tag{3.31c}$$

The axisymmetric coordinate system is accounted for by inserting a factor of r^{*} as shown. The entire $\mathbf{\Gamma}$ term is differentiated by FEMLAB, giving the correct axisymmetric description while minimizing any possible effects of the singularity at $r^{*} = 0$. This requires that any Neumann conditions also be multiplied by r^{*}, since they are written in terms of $\mathbf{\Gamma}$.

The boundary conditions for the problem constitute the only real difference between the perfect and leaky dielectric cases. The perfect dielectric case is characterized by continuity of electric displacement at the interface, and in the static leaky dielectric case, current is continuous. In the present implementation, the boundary conditions for both these cases are as follows, with boundaries labeled as in Figure 3.2:

$$-\hat{n} \cdot \mathbf{\Gamma} = r^{*}\epsilon_r \quad \text{on CE} \tag{3.32a}$$

$$\mathrm{V} = 0 \quad \text{on OD} \tag{3.32b}$$

$$-\hat{n} \cdot \mathbf{\Gamma} = 0 \quad \text{on OC and DE} \tag{3.32c}$$

$$\sum_{i,e}(-\hat{n} \cdot \mathbf{\Gamma}) = 0 \quad \text{on AB} \tag{3.32d}$$

Equation 3.32a applies a nondimensional field of 1 at the far boundary parallel to the equator, and Equation 3.32b constrains the potential at the equatorial symmetry plane to zero. Equation 3.32c represents a pair of Neumann conditions, which prescribe zero flux through the drop's polar axis and through the annular boundary at $r^* = 10$, maintaining the field parallel to these two boundaries. The conditions on CE and DE constitute an approximation to the far-field condition at infinity.

Equation 3.32d, in which $\hat{n}$ is considered to be outwards from whichever domain $\mathbf{\Gamma}$ is being evaluated in, is the interfacial continuity condition. In the perfect dielectric case, this corresponds to continuity of electric displacement, $\epsilon_r \vec{E}$.

The static leaky dielectric case is modeled as in Equation 3.18, by replacing ϵ_r with σ. The result is that the solution in the bulk is the same (since the whole equation is multiplied by the same factor) but the interfacial boundary condition changes from $\Sigma \hat{n} \cdot \epsilon_r \vec{E} = 0$ to $\Sigma \hat{n} \cdot \sigma \vec{E} = 0$, or continuity of current.

The conductivity of each phase is calculated as in Equation 3.5, given the relevant ionic characteristics. The partition of ions between the droplet and continuous phase is described by $c_i/c_e = \alpha$, the partition coefficient. If $\alpha = 10$, for instance, local equilibrium at the interface is such that the concentration of ions in the droplet is ten times the concentration in the continuous phase. For the purposes of this model, we assume the droplet and medium to be in equilibrium when the electric field is turned on, so that the concentration throughout the droplet is α times that of its surroundings at $t = 0$.

In the full leaky dielectric case, where interfacial charge dynamics are modeled, the formulation of the governing equation is done with ϵ_r as opposed to σ, but the interfacial condition changes to:

$$\sum_{i,e}(-\hat{n} \cdot \mathbf{\Gamma}) = r^* q^* \qquad \text{at interface} \tag{3.33}$$

The nondimensionalized interfacial charge density q^* is calculated on each boundary node from Equations 3.19 and 3.26 at the beginning of each time step, based on the combined electrical and fluid mechanical solutions of the previous step. For the first time step, it is considered to be zero. Annotated code for the interfacial charge calculation at each time step is provided in Appendix A.1.

3.7.4 Interfacial Stresses

Once the electrostatic problem has been solved for a particular geometry, the stress on the interface is calculated. This is required as a boundary condition to drive the fluid mechanics problem. The expressions given here do not include viscous/pressure stresses; those are present in the fluid mechanics formulation and do not need to be specified externally.

The interface mean curvature is required for interfacial tension effects. Mean curvature can be expressed as the unweighted average of the two perpendicular principal curvatures. In the case of an axisymmetric body, one of these curvatures is in the

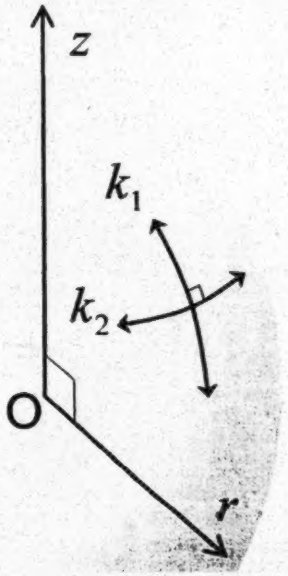

Figure 3.5: The principal curvatures of an axisymmetric body. The in-plane curvature is k_1, and the out-of-plane or perpendicular curvature is k_2.

rz-plane, and the other curvature lies perpendicular to it. Because the surface normal need not be oriented in the r-direction, the second principal curvature is generally not in the $r\theta$-plane. The principal curvatures k_1 and k_2 on an axisymmetric body are shown in Figure 3.5.

The curvature is computed by means of a quartic polynomial fit to the interface nodes from the fluid mechanics mesh. Annotated code is provided in Appendix A.2. Each point receives its own polynomial fit, based on the positions of two nodes on each side, plus itself, for a total of five nodes. In the case of the symmetry boundaries, the second and third nodes from each boundary are mirrored across it to provide a basis for using this method on the boundary node and on the one next to it.

Two polynomial fits are done; the first is oriented using a horizontal axis passing through the endpoints of the fit ($i-2$, $i+2$), as in Figure 3.6a. The normal vector at the centre point is then obtained from the first derivative of the curve, and a new fit is done with the vertical axis parallel to the normal as shown in Figure 3.6b. The

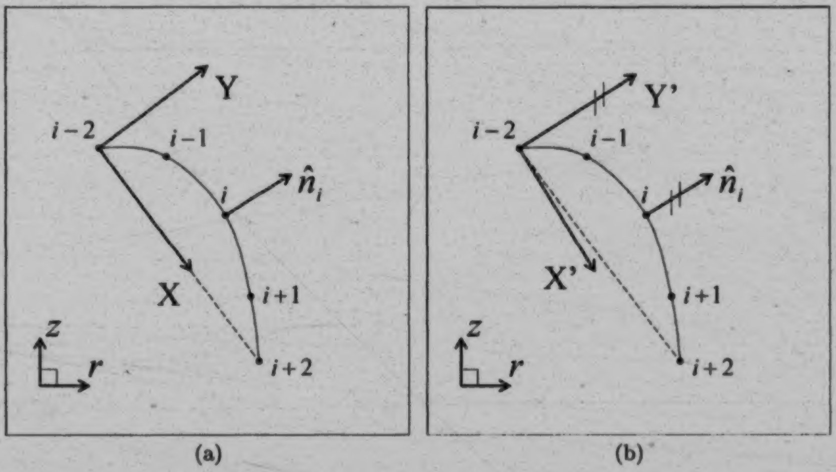

(a) (b)

Figure 3.6: Polynomial fitting for a single interface point. The first fit yields the normal vector at the point in question. The second fit is reoriented so that $\hat{n}_i$ is vertical in the local coordinate system, allowing calculation of the local in-plane curvature.

second derivative of this fit at the centre point i is thus equal to the in-plane curvature k_1 at that point.

In addition to the in-plane curvature k_1, we need another curvature perpendicular to it in order to compute mean curvature. The relevant expression in the axisymmetric case is [Bhattacharjee, 1995]:

$$k_2(r) = \frac{z'(r)}{r\sqrt{1 + z'(r)^2}} \tag{3.34}$$

We can easily obtain $z'(r)$ from the normal vector. This expression is singular at both pole and equator, but its values there can be deduced by considering the geometry: the perpendicular curvature at the pole is the same as the in-plane curvature, and at the equator it is the cylindrical curvature $-r^{-1}$.

Mean curvature, X, is the arithmetic mean of the two orthogonal curvatures:

$$2X = \left(\frac{1}{k_1} + \frac{1}{k_2}\right) \tag{3.35}$$

Once the curvature has been obtained, the electrostatic solution is performed and the interfacial stress is calculated. The perfect dielectric case has only normal stresses; it can be shown that both interfacial tension and nonconducting electrostatics produce stresses normal to the boundary. A slight modification of Equation 3.24a gives the total stress discontinuity at the interface in this case:

$$\vec{S}_n \cdot \hat{n} = \frac{\epsilon_0}{2}(\epsilon_e(\vec{E}_e \cdot \hat{n})^2 - \epsilon_i(\vec{E}_i \cdot \hat{n})^2 - (\epsilon_e - \epsilon_i)(E_{r_i}^2 + E_{z_i}^2 - \vec{E}_i \cdot \hat{n}^2)) + 2\gamma\left(X + \frac{1}{R_0}\right) \tag{3.36}$$

The only difference between this and Equation 3.24a is that the initial mean curvature $-\frac{1}{R_0}$ is subtracted from X in order to improve numerical conditioning. As mentioned in Section 3.5.3, this procedure leads to the initial conditions for the fluid problem becoming uniformly zero, such that Equation 3.25a is used in both the droplet and the continuous phase.

For the leaky dielectric case, Equation 3.36 for the normal stress still holds, since it is based on the Maxwell stress, which is valid for any electric field discontinuity no matter how it occurs. The tangential stress, however, is not zero in this case because charge builds up on the boundary. Tangential stresses develop as in Equation 3.24b:

$$\vec{S}_n \cdot \hat{t} = -\epsilon_0 \vec{E} \cdot \hat{t}(\epsilon_i \vec{E}_i \cdot \hat{n} - \epsilon_e \vec{E}_e \cdot \hat{n}) \tag{3.37}$$

It should be noted that, since the system is axisymmetric and therefore θ-invariant, $\hat{t}_i$ has been reduced to $\hat{t}$.

3.7.5 Fluid Mechanics

The full Eulerian Navier-Stokes equations are employed in the numerical model. Since there is a pressure discontinuity at the interface between the droplet and the continuous phase, and the finite element method assumes continuity of variables, two separate sets of Navier-Stokes equations were used; one for the droplet, and one for the medium, with separate pressure and velocity variables. Special measures are taken to avoid nonphysical mesh convection effects; these are described in Section 3.7.6. The equations are defined in FEMLAB in axisymmetric form, using the general PDE formulation of Equation 3.29, as follows:

$$\mathbf{\Gamma} = \begin{bmatrix} r^*p^* - 2\frac{Q}{Re}r^*\frac{\partial u^*}{\partial r^*} & -\frac{Q}{Re}r^*(\frac{\partial u^*}{\partial z^*} + \frac{\partial v^*}{\partial r^*}) \\ -\frac{Q}{Re}r^*(\frac{\partial v^*}{\partial r^*} + \frac{\partial u^*}{\partial z^*}) & r^*p^* - 2\frac{Q}{Re}r^*\frac{\partial v^*}{\partial z^*} \\ 0 & 0 \end{bmatrix} \tag{3.38a}$$

$$\mathbf{F} = \begin{bmatrix} p^* - r^*Q(u^*\frac{\partial u^*}{\partial r^*} + v^*\frac{\partial u^*}{\partial z^*}) - 2\frac{Q}{Re}\frac{u^*}{r^*} \\ -r^*Q(u^*\frac{\partial v^*}{\partial r^*} + v^*\frac{\partial v^*}{\partial z^*}) \\ -(r^*(\frac{\partial u^*}{\partial r^*} + \frac{\partial v^*}{\partial z^*}) + u^*) \end{bmatrix} \tag{3.38b}$$

$$\mathbf{d_a} = \begin{bmatrix} r^*\frac{Q}{St} & 0 & 0 \\ 0 & r^*\frac{Q}{St} & 0 \\ 0 & 0 & 0 \end{bmatrix} \tag{3.38c}$$

Two physics modes are used, with independent variable names and fluid parameters but otherwise identical equations. This is to allow a pressure discontinuity at the interface between the medium and the droplet, which would otherwise not be possible as the finite element method assumes continuity of variables.

The boundary conditions in the fluid problem are as follows, with boundaries labeled as in Figure 3.2:

$$-\hat{n}\cdot\mathbf{\Gamma} = (0,0) \quad \text{on CE and DE} \tag{3.39a}$$

$$-\hat{n}\cdot\vec{v}^* = 0 \quad \text{on OC and OD} \tag{3.39b}$$

$$\vec{v}_i^* = \vec{v}_e^* \quad \text{on AB} \tag{3.39c}$$

$$\sum_{i,e}(-\hat{n}\cdot\mathbf{\Gamma}) = r^*\frac{\vec{S}_n}{p_0} \quad \text{on AB} \tag{3.39d}$$

The symmetry boundaries OC and OD are given slip conditions, which constrain the normal velocity to zero. Tangential stress at a symmetry boundary is also constrained to zero by these conditions, which is explained later in this section. The far-field boundaries CE and DE are given zero stress conditions. The interface is assigned two conditions, since it requires a method of simultaneously loading the fluid and maintaining appropriate continuity between the two separate Navier-Stokes equation sets.

In the present model, the total stress formulation of the equations is used, which means that the pressure terms are included in the flux term, $\mathbf{\Gamma}$, in Equation 3.38. This causes the pressure to participate in the Neumann condition in Equation 3.39d, avoiding overconstraint problems that can arise through the artificial division of pressure and viscous stresses.

Equation 3.39c constrains the external fluid velocity to match the internal fluid velocity at the interface. This preserves continuity and represents half of the necessary boundary definition.

The fluid in the droplet sees a total stress (Neumann) condition in which the electrical/interfacial tension load is added to the total stress from the external fluid. This is implemented by specifying the electrical/interfacial tension stress (multiplied by r^* for compatibility with the axisymmetric formulation) as the Neumann condition, leaving out the fluid stresses. In spite of the fact that the two domains have separate definitions of the Navier-Stokes equations, and thus FEMLAB could not be expected to maintain continuity of fluid stress between them, this method nevertheless produces the correct result. This is because FEMLAB describes general boundary conditions as in Equation 3.30b:

$$\sum(-\hat{n} \cdot \mathbf{\Gamma}) = \mathbf{G} + \left(\frac{\partial \mathbf{R}}{\partial \mathbf{u}}\right)^T \boldsymbol{\mu}$$
$$\mathbf{R} = 0$$

with $\mathbf{G}$ being the Neumann condition and $\mathbf{R}$ the Dirichlet condition. In most cases a nonzero Dirichlet condition will simply cancel the Neumann condition by bringing in the Lagrange multiplier $\boldsymbol{\mu}$. However, if variables from both domains are used together in **R**, the Lagrange multipliers can actually become defined, and the Neumann condition activates. In this case, there are two Navier-Stokes domains adjacent to one another but with separate variables; u_i^*, v_i^*, $p_i{}^*$ and u_e^*, v_e^*, $p_e{}^*$. If continuity of velocity is applied to one domain and a stress condition to the other, the boundary representation in FEMLAB (considering velocity variables only) is as follows:

$$\mathbf{u} = \begin{bmatrix} u_i^* & v_i^* & u_e^* & v_e^* \end{bmatrix} \quad \text{equation set} : \begin{Bmatrix} < \mathrm{r} - \text{momentum } i > \\ < \mathrm{z} - \text{momentum } i > \\ < \mathrm{r} - \text{momentum } e > \\ < \mathrm{z} - \text{momentum } e > \end{Bmatrix}$$

$$\mathbf{G} = \begin{bmatrix} |\vec{S}_n^*| n_r \\ |\vec{S}_n^*| n_z \\ 0 \\ 0 \end{bmatrix} \quad \mathbf{R} = \begin{bmatrix} 0 \\ 0 \\ u_i^* - u_e^* \\ v_i^* - v_e^* \end{bmatrix} \quad \mathbf{h} = -\frac{\partial \mathbf{R}}{\partial \mathbf{u}} = \begin{bmatrix} 0 & 0 & 0 & 0 \\ 0 & 0 & 0 & 0 \\ -1 & 0 & 1 & 0 \\ 0 & -1 & 0 & 1 \end{bmatrix} \quad \boldsymbol{\mu} = \begin{bmatrix} \mu_1 \\ \mu_2 \\ \mu_3 \\ \mu_4 \end{bmatrix}$$

and since $-\hat{n} \cdot \boldsymbol{\Gamma} = \mathbf{G} - \mathbf{h}^T \boldsymbol{\mu}$ for a boundary where each application mode is active on only one side, which is the situation here, this results in:

$$-\hat{n} \cdot \boldsymbol{\Gamma} = \text{stress on boundary} = \begin{bmatrix} |\vec{S}_n^*| n_r + \mu_3 \\ |\vec{S}_n^*| n_z + \mu_4 \\ 0 - \mu_3 \\ 0 - \mu_4 \end{bmatrix} \tag{3.40}$$

The combined condition of Equation 3.40 defines a stress difference between the two fluids, rather than a simple absolute surface pressure on the internal fluid.

The slip condition works similarly. A slip/symmetry boundary for a single fluid is defined as follows:

$$\mathbf{G} = \begin{bmatrix} 0 \\ 0 \end{bmatrix} \quad \mathbf{R} = \begin{bmatrix} -(u^* n_r + v^* n_z) \\ 0 \end{bmatrix} \quad \mathbf{h} = -\frac{\partial \mathbf{R}}{\partial \mathbf{u}} = \begin{bmatrix} n_r & n_z \\ 0 & 0 \end{bmatrix} \quad \boldsymbol{\mu} = \begin{bmatrix} \mu_1 \\ \mu_2 \end{bmatrix}$$

This leads to:

$$-\hat{n} \cdot \boldsymbol{\Gamma} = \text{stress on boundary} = \begin{bmatrix} 0 - n_r \mu_1 \\ 0 - n_z \mu_1 \end{bmatrix} \tag{3.41}$$

In addition to the velocity constraint, this condition also maintains the viscous stress normal to the symmetry boundary.

3.7.6 Moving Mesh

Since the deformation of the droplet is the parameter under study, it is necessary to formulate a moving-boundary problem. The method used is a Lagrangian moving mesh, where at the end of each time step, the mesh is convected according to the local velocity. Figure 3.7 shows the mesh update procedure being performed on a single mesh point i, where the distance moved is $\vec{x} = \vec{v}^{i}_{avg} \Delta t$.

The actual mesh motion is performed on one of the reference copies of the solved FEMLAB data structure, since the original is cleared and redefined at the beginning of the next step. The moved mesh from the copy can then be imported into the new structure. The distance moved by each mesh point is calculated approximately using a quadratic averaging technique, using output times at the beginning, middle, and end of the time step:

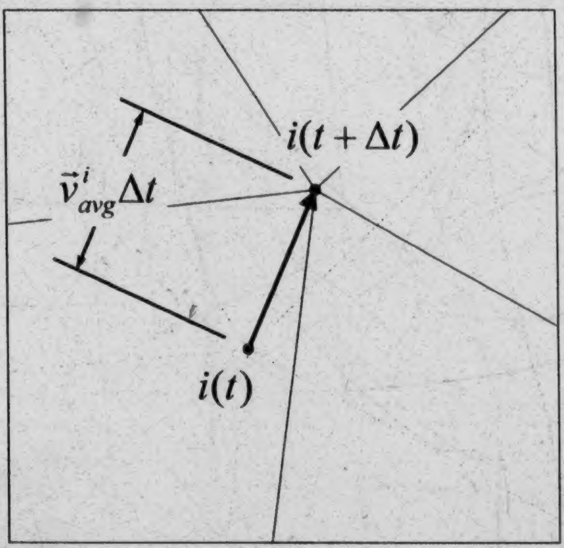

Figure 3.7: Motion of a single mesh point during the geometry update step, using velocity information from the Navier-Stokes solution.

$$\vec{x}(t+\Delta t) = \vec{x}(t) + \Delta t\left[\frac{1}{6}\vec{v}(t) + \frac{2}{3}\vec{v}(t+\frac{\Delta t}{2}) + \frac{1}{6}\vec{v}(t+\Delta t)\right] \tag{3.42}$$

This may be nondimensionalized to give the correct value in the normalized geometry, by using nondimensional values for the variables and multiplying the raw velocity average by the Strouhal number:

$$\vec{x}^*(t+\Delta t) = \vec{x}^*(t) + St\Delta t^*\left[\frac{1}{6}\vec{v}^*(t) + \frac{2}{3}\vec{v}^*(t+\frac{\Delta t}{2}) + \frac{1}{6}\vec{v}^*(t+\Delta t)\right] \tag{3.43}$$

Second-order averaging is possible because the fluid mechanics time step is handled by a nonlinear solver that produces intermediate output, thus making a midpoint solution available. An annotated copy of the code for this method is provided in Appendix A.3.

After moving the mesh, and before using it in the new FEM structure, the curve parameters in the moved mesh are rescaled. Each boundary in the geometry has a curve parameter that varies from zero to one (usually) along its length. When the mesh is convected, these curve parameters are convected with it, and if there is substantial flow along a boundary, the curve parameter map can become highly distorted. Since FEMLAB's mesh generator refers to the curve parameter for spacing information on boundaries, this can render remeshing ineffective at restoring element quality. Rescaling the curve parameter to be proportional to chord length after each time step removes the distortion and prevents the resulting breakdown of the solution. An annotated copy of this function is included in Appendix A.4.

Geometry redefinition takes advantage of FEMLAB's "mesh as geometry" feature, by which a FEMLAB mesh can be treated as a geometry with no extra processing. At the beginning of the next time step, the moved mesh is assigned to the geometry field in the new FEMLAB data structure, and, if no remesh is necessary, to the mesh field as well. In order to determine whether a remesh is necessary, the element quality, or minimum aspect ratio, is calculated for each element. If the smallest value of element quality in the moved mesh is less than 0.6, a new mesh is created on the geometry defined by the moved mesh.

The diagram in Figure 3.8 illustrates the procedures detailed in this section and the following section. The relationships between the meshes and solution mappings between time steps are shown.

3.7.7 Variable Reinitialization

Remapping of the old solution to the new node positions is necessary to create an initial condition for the next time step. Since the full Eulerian Navier-Stokes equations are used to describe the fluid mechanics, simply moving the solution with the nodes is inadmissible because it would introduce spurious convection. Reinitialization is therefore done in place, obtaining the solution from an unmoved copy of the FEM

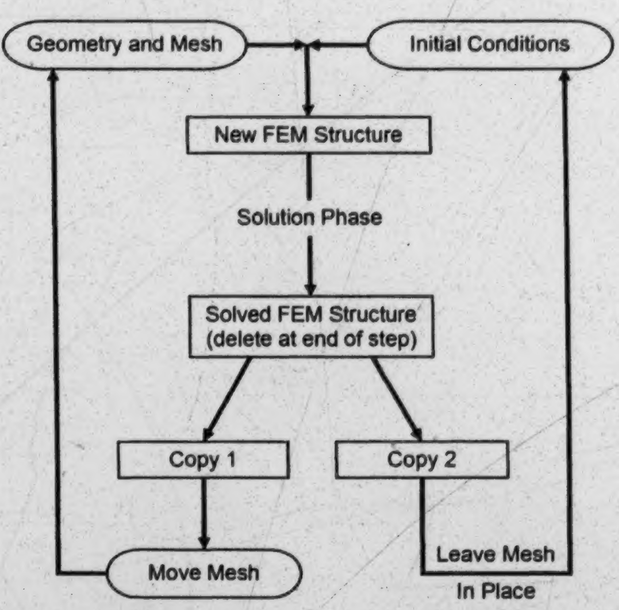

Figure 3.8: Geometry, mesh, and solution reinitialization between time steps. Two copies of the FEM structure are used; one for the moved geometry/mesh, and one for the in-place solution reinitialization.

structure and interpolating it onto the new nodes.

The method is as follows: for each fluid mechanics variable, the list of global degrees of freedom in the current extended mesh is analyzed, and a sub-list of the degree-of-freedom numbers corresponding to that variable is generated. After this, the geometric coordinates corresponding to each entry in the sub-list are obtained, and FEMLAB's postprocessing interpolator is used to find the value of the variable in question at those coordinates in the old, unmoved mesh from the previous time step. More detail is available in the annotated code provided in Appendix A.5.

Since with a moving boundary, part of each subdomain may have moved into the space formerly occupied by the other, and since each subdomain uses a separate set of fluid variables, an attempt to interpolate the value of a degree of freedom near the interface may fail. The reinitialization code checks for the failure of the interpolator for a given variable and uses the corresponding variable (radial velocity, axial velocity, or pressure) from the other subdomain. Extrapolation is only allowed during these recovery attempts. Zero is used if the recovery attempt fails; this indicates that the point in question has moved off one of the exterior boundaries.

The degree-of-freedom numbers are used by FEMLAB as indices into the solution vector, so the reinitialization code uses them to concatenate the results of the interpolation procedure into a vector functionally equivalent to a FEM solution. This constructed solution is used as the initial condition in the next time step.

3.8 Summary

In this chapter, the problem of a drop deforming in an electric field has been examined mathematically, and its theoretical foundation has been established for the two limiting cases of perfect and leaky dielectric fluid systems. The conversion of the general descriptor equations to a finite element problem has been detailed, and the numerical solution procedure has been described.

The next chapter begins by providing representative examples to demonstrate that the numerical results are independent of the discretization employed. The results of the numerical simulations are then compared with analytic, numerical and experimental results from other researchers, in order to demonstrate the validity of the present model.

CHAPTER 4

CONVERGENCE TESTING AND VERIFICATION

In this section, the numerical algorithm described in Chapter 3 is tested to confirm that the solution is not strongly dependent on the discretization level in space and time, or on the solution tolerances employed in the time-dependent solver. To assess the accuracy of the numerical code, the results of the simulations are then compared with established analytic results. For small deformations the method presented here should converge to the appropriate asymptotic result.

For small deformations and relatively low viscosities, the dynamic response obtained from the numerical solution is compared with the analytic results given by Scott et al. (1990). They obtained their result from Miller and Scriven (1968), who developed a damping time and damped natural frequency based on the inviscid natural frequency and drop parameters.

In order to verify the dynamic leaky dielectric boundary condition, the time scale of the numerical charge relaxation is compared with the analytic time scale. If these two values match, and the final deformation matches the predicted value, then charge buildup via migration is being modeled accurately. Convective transport on the boundary has an effect on the steady-state charge distribution and drop deformation, as detailed in Feng (1999). Comparison of a test case with Feng's results serves to test the accuracy of the convection treatment.

Nmerical modeling of droplet dynamics has been done in the past by other researchers [Basaran, 1992, Hirata et al., 2000], and this provides a basis for verification in cases of large deformation or high Reynolds number. Finally, the present model is tested against the experiments of Lu (2002) in order to test its ability to predict the behaviour of real physical systems.

4.1 Numerical Convergence Testing

4.1.1 Demonstration of Mesh Independence

In order to be assured of the accuracy of a finite element solution, it is necessary to observe that the discretization is sufficiently fine so as to have no significant effect on the solution. For this problem, the critical area is the immediate vicinity of the interface, and so it is expected that mesh refinement there will have the most significant effect. Outside this region, a general refinement is held to be sufficient to test for mesh independence.

Convergence testing must be done every time a simulation is run that departs significantly from the parameter range of existing convergence studies, unless a wide-

Table 4.1: Perfect Dielectric Base Case

Applied Electric Field E_0	1 MV/m
Droplet Radius R_0	1 μm
Droplet Relative Permittivity ϵ_i	80
Medium Relative Permittivity ϵ_e	3
Interfacial Tension γ	0.03 N/m
Droplet Density ρ_i	1000 kg/m^3
Medium Density ρ_e	1000 kg/m^3
Droplet Viscosity μ_i	0.001 Pa·s
Medium Viscosity μ_e	0.001 Pa·s

ranging relationship can be derived or deduced between the physical parameters and the convergence behaviour. The results presented here are representative and limited to a single physical case, which will henceforth be called the base case. It approximates a water droplet in oil with a radius of 1 μm, subject to a 1 MV/m applied electric field. Deformation in the base case is small; the OTAM result predicts a steady-state deformation parameter of 3.9926×10^{-4}. Table 4.1 details the base case parameters for perfect dielectric fluids.

Figure 4.1 shows the effect of altering the boundary refinement across a range of values, with the far-field set to FEMLAB's default resolution. The parameter 'Hmax' is a mesh size specification in FEMLAB; here it is used exclusively on the interfacial boundary, with the bulk fluid and all other boundaries left at the default resolution. The electrostatics problem is solved on the same mesh as the fluid mechanics.

It was noted during testing that refinements further away from the interface have

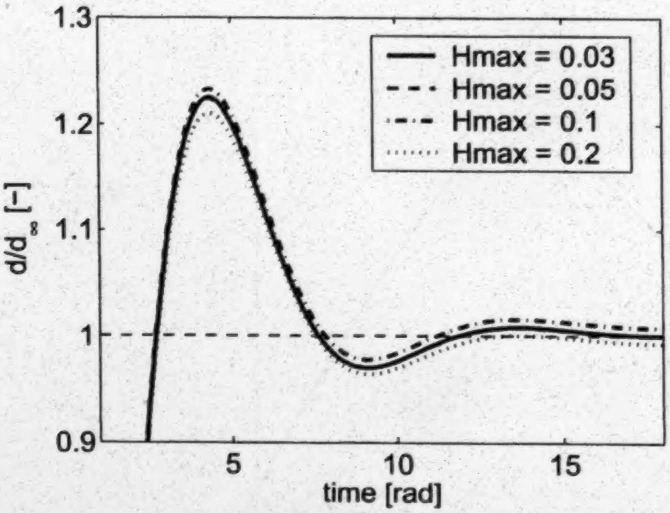

Figure 4.1: Variation of dynamic response for increasing mesh refinement at drop interface. The parameter varied is 'Hmax', which is a mesh size specification in FEMLAB, applied here to the interfacial boundary only. Time step is 0.06 radians.

no appreciable effect on the fluid mechanics solution. Accordingly, no mesh size specifications are made except in the area of the interface. Using the default resolution in the bulk allows a mesh-independent solution for the deformation, provided that the interface grid is sufficiently fine.

With 9 nodes on the interface ('Hmax' = 0.2), the error in the solution is significant, though not large. Increasing the resolution to 17 nodes ('Hmax' = 0.1) results in a reversal of the error, which suggests that multiple factors, such as error in the electrostatics solution, are contributing to the error in the first case. This implies that, despite the moderately low error, the results in general are not trustworthy at such low interfacial resolutions.

At a resolution of 33 nodes on the boundary ('Hmax = 0.05'), the results are effectively converged. The steady-state is approximately 0.02% greater than the analytic OTAM result, and the dynamic response shows a peak 0.062% lower than that of the 54-node case ('Hmax' = 0.03). The 54-node case is approximately 0.02% further from the OTAM result than the 33-node case, but since the deformation in this problem is non-zero, such a result is not necessarily incorrect. The global mesh in the case of the 33-node boundary contains 1424 elements, and in the case of the 54-node boundary, the global mesh contains 1960 elements.

For optimum computational expenditure, the base case is best solved with an 'Hmax' of 0.05, or 33 interface nodes. Simulations of larger deformations displaying nonlinearity or instability sometimes require an interface mesh size of 0.03 (54 nodes), but refinement beyond 54 nodes has proved to have little effect on most problems.

Table 4.2 details the effect on convergence of varying the electrostatics mesh independently of the fluid mechanics mesh. The base case perfect dielectric problem was used in these tests. The parameter 'Hmax' is used to control the interfacial mesh size. Refinement is used to increase global mesh density. The fluid mechanics mesh for these tests used 'Hmax' = 0.03, or 54 nodes on the boundary, with no global

Table 4.2: Effect of Mesh Alterations in the Electrostatics Problem

case	Hmax	refine?	#elem.	$\frac{d_{final}}{d_t}$	$\int_s \sum \hat{n} \cdot \epsilon_r \nabla V^*$	$\int_s \sum \hat{n} \cdot \epsilon_r \nabla V^*$ (remap)
1	0.3	no	816	0.92185	-0.06740	-0.07370
2	0.1	no	1046	0.99051	-0.016077	-0.015449
3	(0.03)	no	1960	1.00047	-0.004149	(-0.004149)
4	0.1	yes	4000	0.98927	-0.018638	-0.017462

refinement, and the time step was 0.06 radians. The ratio d_{final}/d_t compares the calculated steady-state deformation with the analytic result. This provides a measure of the accuracy of the numerical method, with a ratio of 1 signifying perfect agreement with the asymptotic OTAM theory.

It is critical that the electrostatics solution be accurate at the interface, since the interfacial electric field drives the fluid mechanics problem. The last two columns are line integrals of the discontinuity in electric displacement along the droplet interface from pole to equator. For an ideal Laplace solution, this value should be zero, in accordance with Equation 3.16b. The first of these columns (the second column from the right) is the result of performing this integration directly on the electrostatics mesh. The last column on the right is the result of remapping the solution to the fluid mechanics mesh before integrating. The difference between these two numbers may provide an indicator of how much degradation is introduced when the electrostatics solution is used in the interfacial stress boundary condition in the fluid mechanics problem.

Case 1 describes the FEMLAB default meshing parameters. The result has poor resolution and yields a deformation nearly 8% lower than predicted analytically. The electric displacement discontinuity at the boundary is also large. Case 2 describes the same situation, but with the interfacial mesh resolution tripled. The performance is good, with less than 1% deviation between theory and experiment. Continuity of electric displacement is still imperfect.

Case 3 is obtained by importing and using the fluid mechanics mesh. The resolution at the boundary is very high, and it drops off quickly far from the drop. This is evidently adequate, because this case has by far the best performance out of those tested.

Case 4 has somewhat lower interfacial resolution than case 3. The refinement cuts element sizes approximately in half, resulting in an interfacial resolution equivalent to that obtained with 'Hmax' = 0.05 in the absence of refinement. The fluid mechanics is already converged at this resolution. However, the electrostatics problem shows poorer performance despite the uniformly high resolution in the bulk. Reusing the fluid mechanics mesh appears to be the best option out of those listed.

4.1.2 Effect of Time Step on Accuracy and Stability

Figure 4.2 shows the effect of time step on the convergence of the base case perfect dielectric problem. The time step is expressed in radians, where 2π radians signifies one complete cycle of oscillation of the drop as predicted by inviscid theory (Equation 3.2). Three time steps are tested: 0.03, 0.06, and 0.09 radians.

The first two cases demonstrate good agreement with one another, with a peak value difference of less than 0.5%. The steady-state is, predictably, much less sensitive to time step, and agrees within 1.5 ppm between these two cases. The 0.09 radian time step, on the other hand, is too large to maintain stability, and the pole of the drop oscillates in an unsteady fashion, eventually compromising the geometric integrity of the mesh. Only the beginning of this instability is shown here, as the full plot would mask the peaks of the other two curves.

These plots were obtained with an interface resolution of 54 nodes, which is finer than necessary for this problem. If 33 nodes are used, the stability limit is raised somewhat. Figure 4.3 demonstrates this.

In Figure 4.3, it may be seen that the stability limit is significantly higher for a

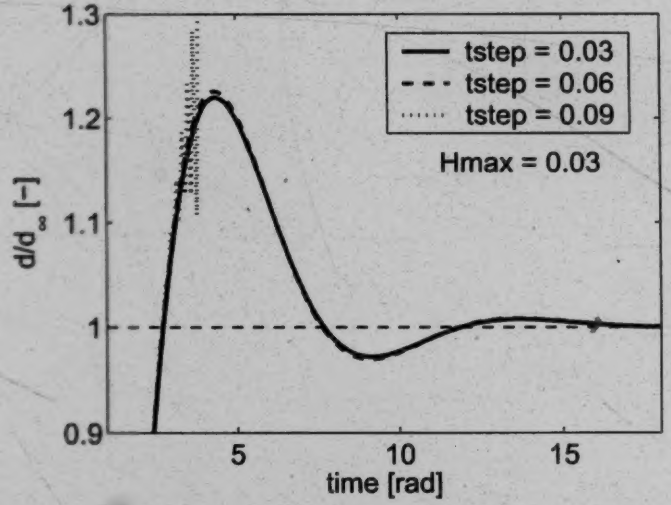

Figure 4.2: Convergence of dynamic response with time step, for a 54-node interface. The nondimensional time step 'tstep' is given in radians, based on the analytic inviscid natural frequency of the drop.

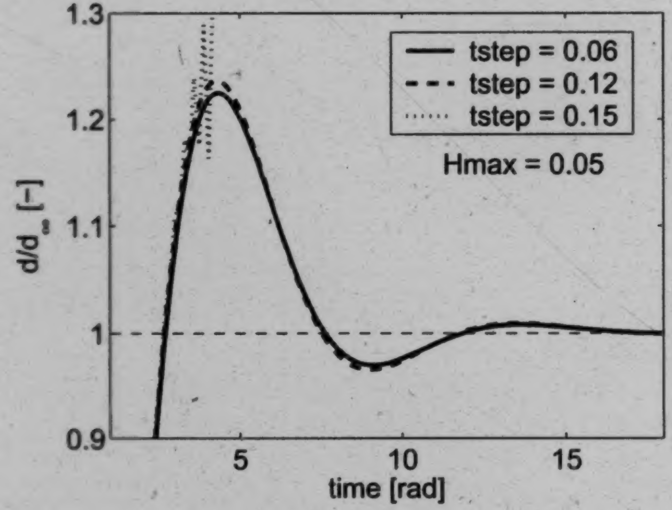

Figure 4.3: Convergence of dynamic response with time step, for a 33-node interface.

less refined interface. However, the general trend of the results is similar. Time steps of 0.06 and 0.12 radians produce results within 1% of one another at peak, and a time step of 0.15 radians is unstable. On both meshes tested here, the required time step for stability is very close to the required time step for accuracy. In general, it has been found that if a simulation runs to completion without mesh instability, the results can be trusted in most cases. Exceptions occur in cases of large deformation with physical instability leading to breakup.

4.1.3 Effect of Solver Tolerances

The time-dependent solver DASPK employed in these calculations has two tolerance variables: 'atol' and 'rtol', the absolute and relative tolerances. By default, the absolute tolerance is set at 0.01 for velocity and infinity for pressure in FEMLAB's Navier-Stokes application mode, and the relative tolerance is set at 0.01. These tolerances have been re-used for the general-form model in the present work.

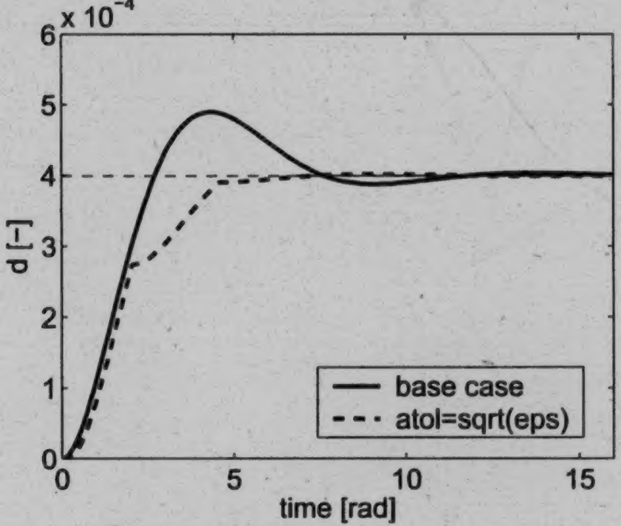

Figure 4.4: Effect of very small absolute tolerance on the dynamic solution.

These values seem to be high at first sight. However, while attempting to test convergence with respect to these variables, it is observed that neither of them alter the solution of the base case at all, even when reduced to 10^{-6}. The only exception occurs when 'atol' is reduced to $\sqrt{\text{eps}}$, where eps is 2.2204×10^{-16}, the limit of machine precision. In that case, the solver repeatedly fails to follow the solution through, resulting in the plot in Figure 4.4. It appears as though the flow field is suddenly arrested at multiple points along the solution, and that it then begins to accelerate again from a stop. The precise mechanism of this failure mode is not clear.

Use of lower tolerances can have an effect on problems with more extreme conditions and parameters. However, the effect is not often large. It was noted in the previous section that the solution for the base case with finely discretized interface is accurate just under the stability limit. Since any problem too nonlinear for DASPK's default settings to handle would constitute a time step too large for stability, the question of solver tuning does not arise. This finding should not be considered universally true for the complete parameter space of the model, but it has proved to be widely applicable.

4.2 Accuracy of Small Steady-State Deformations

The OTAM and Taylor results (Equations 2.7 and 2.10, respectively) form the analytic foundation of this problem. They are first-order steady-state approximations to the deformation of perfect dielectric and leaky dielectric droplet systems respectively. A given simulation, provided the deformation is small enough, should match the appropriate analytic result at steady-state.

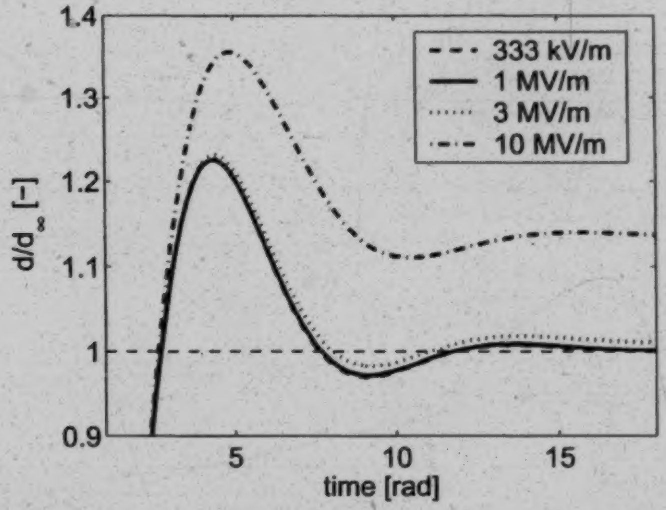

Figure 4.5: Normalized Dynamic Responses for Variation in Electric Fields: Perfect Dielectric Model.

4.2.1 Perfect Dielectric Model

Figure 4.5 shows four results for the perfect dielectric case. The vertical axis is normalized by the analytically predicted (OTAM) deformation, so that ideally each numerically obtained dynamic response should converge to 1 for large time. The physical parameters are as listed in Table 4.1, and the electric field is varied.

It can be seen that for the lower two values of the electric field, the numerical result does converge almost exactly to the analytic result. The 3 MV/m case is slightly offset, which indicates the onset of nonlinearity - the droplet becomes nonspherical and the assumption of infinitesimal deformation begins to fail. The deformation parameter in this case is approximately 0.0036, which is relatively small. The 10 MV/m case with $d_{OTAM} = 0.04$ is significantly nonlinear, and illustrates well the characteristic increase in elongation other researchers have observed in large prolate deformations [Garton and Krasucki, 1964, Miksis, 1981].

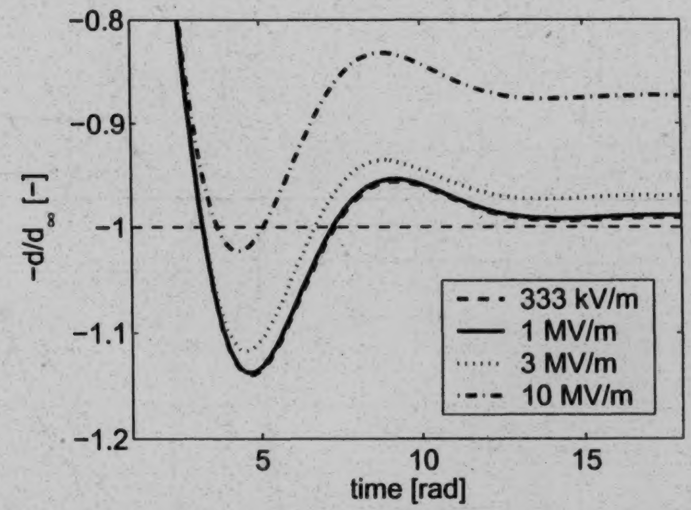

Figure 4.6: Normalized Dynamic Responses for Variation in Electric Fields: Leaky Dielectric Model.

4.2.2 Leaky Dielectric Model

Figure 4.6 shows four results from the static-boundary leaky dielectric case. The physical parameters are the same as in the perfect dielectric base case, but the additional specification of equal ionic concentrations in the two fluids is made.

It may be noted that the nonlinearity is uniformly somewhat larger than for the perfect dielectric case; this may be because the absolute deformations involved are larger by approximately a factor of 10. The Taylor result for the 10 MV/m case is approximately -0.5 (the negative sign indicating oblate, or squashed, deformation), which is admittedly not small. In addition, unlike the perfect dielectric case, the leaky dielectric case exhibits a dynamic equilibrium, due to the steady-state circulation resulting from free charge on the interface. This introduces an additional avenue for systematic error, since the steady-state deformation now depends strongly on the accuracy of the Navier-Stokes solution. This may explain the slightly greater offset observed here between the low-field results and the analytic Taylor result.

The perfect and leaky dielectric models, as implemented in the present numerical method, both generate small-deformation results in excellent agreement with their respective analytic limits. Figures 4.5 and 4.6 illustrate this well, and despite a small systematic offset in the leaky dielectric case, it may be said that the present numerical formulation accurately captures the steady-state behaviour of both perfect and leaky dielectric systems for small deformations.

4.3 Comparison of Dynamics With Existing Theory

4.3.1 Droplet Natural Frequency and Damping

The natural frequency of a fluid droplet in a fluid medium in the absence of viscosity is given by Whitaker et al. (1998) . As noted in Chapter 3, Section 3.4.1, the dominant harmonic in this case is $n = 2$. Equation 3.2 gives the corresponding time scale, which is the inverse of the natural ($n = 2$) frequency ω_2 in rad/s:

$$\omega_2 = \sqrt{\frac{24\gamma}{(2\rho_e + 3\rho_i)R_0^3}} \tag{4.1}$$

The approximate damping rate of this system is given by Whitaker et al. (1998), as well as by Scott et al. (1990):

$$\sigma_d \simeq \frac{(2n+1)^2(\omega_n\mu_i\mu_e\rho_i\rho_e)^{1/2}}{\sqrt{2}\beta} - \frac{(2n+1)^4\rho_i\rho_e\mu_i\mu_e}{\beta^2} + \frac{\left\{ \begin{array}{r} (2n+1)\left\{2(n-1)(n+1)\mu_i^2\rho_i + 2n(n+2)\mu_e^2\rho_e \right. \\ \left. +\mu_i\mu_e[(n+2)\rho_i - (n-1)\rho_e]\right\} \end{array} \right\}}{R_0\beta[(\mu_i\rho_i)^{1/2} + (\mu_e\rho_e)^{1/2}]} \tag{4.2}$$

where

$$\beta = 2R_0[n\rho_e + (n+1)\rho_i][(\mu_i\rho_i)^{1/2} + (\mu_e\rho_e)^{1/2}] \tag{4.3}$$

Scott et al. (1990) give the natural frequency in the presence of small viscous damping as:

$$\omega_d = \omega_n - \frac{(2n+1)^2\sqrt{\omega_n \mu_i \mu_e \rho_i \rho_e}}{2\sqrt{2}R_0(n\rho_e + (n+1)\rho_i)(\sqrt{\mu_i\rho_i} + \sqrt{\mu_e\rho_e})} \tag{4.4}$$

Simplifying the damping rate expression for $n = 2$ results in:

$$\sigma_d \simeq \frac{25\sqrt{\omega_0 \mu_i \mu_e \rho_i \rho_e}}{\sqrt{2}\beta} - \frac{625\rho_i\rho_e\mu_i\mu_e}{\beta^2} + \frac{\left\{ 5\left\{6\mu_i^2\rho_i + 16\mu_e^2\rho_e + \mu_i\mu_e[4\rho_i - \rho_e]\right\} \right\}}{R\beta[\sqrt{\mu_i\rho_i} + \sqrt{\mu_e\rho_e}]} \tag{4.5}$$

$$\beta = 2R_0[2\rho_e + 3\rho_i][\sqrt{\mu_i\rho_i} + \sqrt{\mu_e\rho_e}]$$

and the damped natural frequency becomes:

$$\omega_d = \omega_2 - \frac{25\sqrt{\omega_2 \mu_i \mu_e \rho_i \rho_e}}{2\sqrt{2}R_0(2\rho_e + 3\rho_i)(\sqrt{\mu_i\rho_i} + \sqrt{\mu_e\rho_e})} \tag{4.6}$$

The complete dynamic response can be obtained by assuming that the drop is a linear second-order dynamic system. The relevant s-plane transfer function in this case is [Franklin et al., 2002]:

$$G = \frac{\sqrt{\omega_d^2 + \sigma_d^2}}{s^2 + 2\sigma_d s + \omega_d^2 + \sigma_d^2} \tag{4.7}$$

where $\sqrt{\omega_d^2 + \sigma_d^2}$ is a fictitious undamped natural frequency extrapolated from the parameters given in Equations 4.5 and 4.6. This is not the same as the inviscid natural frequency given in Equation 4.1, because the damping in the suspended drop system does not behave identically to damping in an ideal linear system.

Figure 4.7 shows a simulation of a perfect dielectric drop, identical to the base case except that the external viscosity has been reduced by a factor of 10 to better

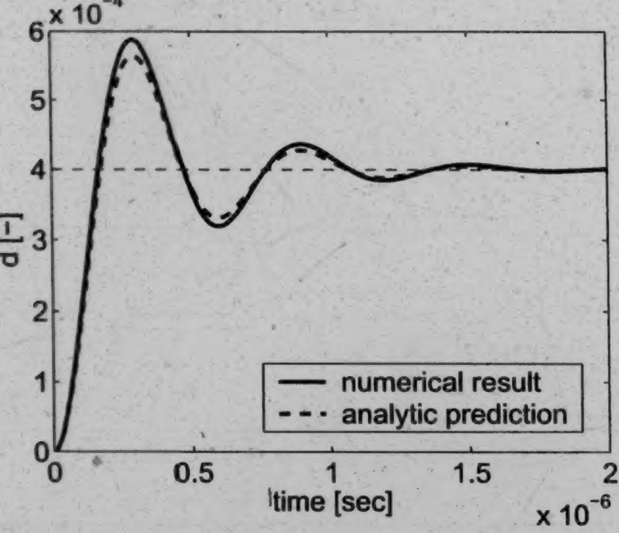

Figure 4.7: Comparison of numerical and analytic dynamic responses: Perfect dielectric, low viscosity.

show the oscillatory behaviour. Superimposed for comparison is a curve obtained by applying the natural frequency and damping rate calculated above in the context of a linear second-order dynamic system.

It is clear from this figure that the damped natural frequency from the numerical model is in extremely good agreement with the theory. The damping rate is also in good agreement, although the peak overshoot is not predicted precisely. Exact agreement in all facets of the problem is, however, not necessarily expected, since the linear second-order dynamic theory does not exactly apply to oscillating drops even for relatively small deformations and low viscosities. This is evidenced by the necessity of calculating the damped natural frequency explicitly using Equation 4.6, rather than using the inviscid natural frequency directly in Equation 4.7.

4.3.2 Interface Charge Dynamics

Conduction

If charge transport by conduction is significantly faster than transport by convection, using the full leaky dielectric model with charge dynamics does not substantially alter the steady-state value of the deformation. In addition, if conduction is sufficiently fast compared to the oscillation of the drop, the dynamic response of the drop obtained from the full leaky dielectric model approaches that obtained from assuming static equilibrium for the interface charge. The dynamic interface charge model as implemented in this work should demonstrate nearly identical results to the static interface treatment if the conduction time scale is short enough.

Figure 4.8 compares the static and dynamic models for an ionic concentration of 0.01 M in the base case. The conductivity is 0.075 S/m, and the resulting electric time scale given by Equation 3.4 is almost exactly equal to one time step (0.06 radians, or 5 ns for this system). The inset is a magnified view of the first few time steps for both curves.

The curves in Figure 4.8 are very similar due to the rapid relaxation of the boundary charge to steady-state, as well as the relative unimportance of charge convection in this specific instance. The difference between the curves during the transient can be almost entirely explained by the time taken for the interfacial charge to build up in the dynamic case. The steady-state difference in values is below 0.02%, and both curves approach within 1% of the analytic Taylor result. This indicates that the final distribution of free charge density generated by the dynamic interface charge method is correct.

The time constant for charge relaxation is given by Saville (1997) as $\epsilon_r \epsilon_0/\sigma$. For the case of a two-fluid interface, Feng (1999) gives the time scale as $\epsilon_0(\epsilon_i + \epsilon_e)/(\sigma_i + \sigma_e)$. The dynamic response in this case should be first-order, since interfacial free

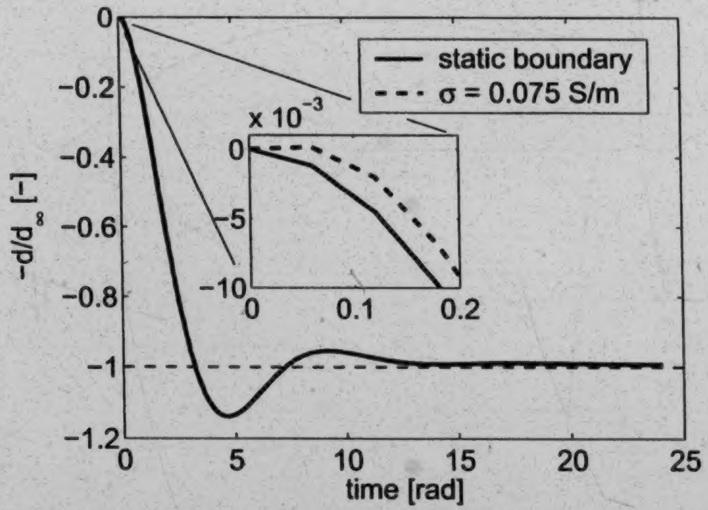

Figure 4.8: Leaky dielectric model: Comparison of static interfacial charge boundary condition with fast dynamic charge relaxation on interface, for an ionic concentration of 10^{-2} M, yielding a conductivity of 0.075 S/m.

charge buildup does not exhibit momentum in the continuum description. The total net charge of any part of the interface can therefore be described, to a reasonable approximation, as a single exponential, with time constant τ_e and steady-state value equal to the net interface charge integrated over the surface at equilibrium:

$$\int_A q(t)\,dA \;\simeq\; \left(1 - e^{-t/\tau_e}\right) \int_A q(\infty)\,dA \tag{4.8}$$

Figure 4.9 shows the total interfacial charge on the upper hemisphere of the droplet as a function of time, for a conductivity of 7.51×10^{-5} S/m. Feng's expression gives a relaxation time of 4.89×10^{-6} s, by which the time axis is normalized. The fluid mechanics solution and mesh mover code are disabled for this run, so the contribution from convection/dilation is zero.

It can be seen from the figure that the time scale corresponds reasonably well to

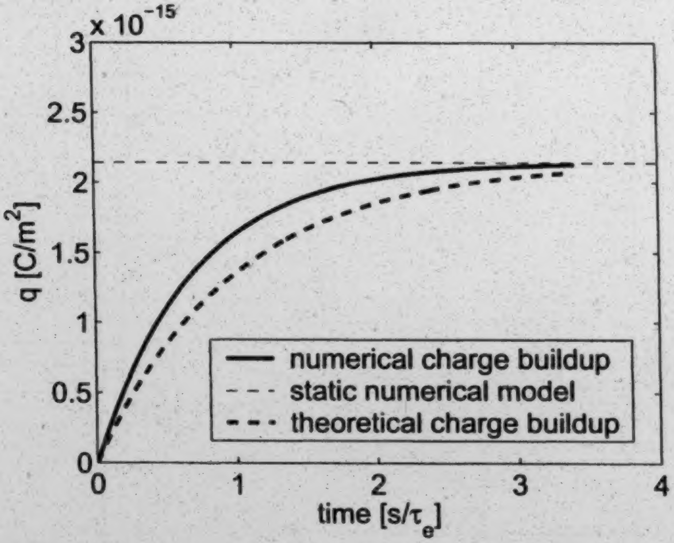

Figure 4.9: Total interfacial charge buildup on upper hemisphere as a function of time, for a far-field ionic concentration of 10^{-5} M and a partition coefficient of 1.

unity on the normalized time axis, which suggests that in addition to the final distribution, the time history provided by the numerical method is approximately correct. There remains a significant difference between these two results, which may be explained by examining the main assumption under which the theoretical prediction was obtained.

The theoretical prediction of the interfacial charge buildup assumes that the combined effect of conduction in two fluids is modeled well by a single exponential, as in Equation 4.8. Figure 4.9 indicates that this may not be the case. In order to obtain a conclusive test of the numerical model's accuracy, the parameters of the modeled system were altered so as to make conduction in the drop dominant over conduction in the continuous phase. This mitigates the effect of combined two-fluid conduction and should allow Equation 4.8 to accurately describe the physical system.

Figure 4.10 shows a comparison of the numerical results with the theoretical pre-

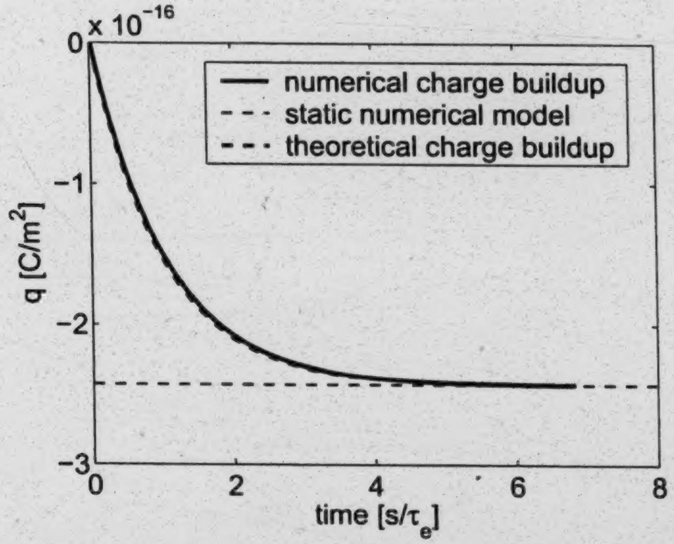

Figure 4.10: Total interfacial charge buildup on upper hemisphere as a function of time, for a far-field ionic concentration of 10^{-7} M and a partition coefficient of 1000.

diction of Equation 4.8 for the modified case. The external conductivity is reduced to 7.51×10^{-7} S/m, and the partition coefficient is increased to 1000, so that the drop plays a dominant role in charge transfer and the time evolution is more nearly a single exponential. The time scale for these given parameters is 9.77×10^{-7} s. It is clear from Figure 4.10 that the agreement is much better than before, which implies that the numerical model is correct.

Convection

The characteristic steady-state vortices predicted by Taylor (1966) involve flow along the interface of the drop. This flow convects free charge on the interface, and may significantly alter the steady-state distribution of charge. This affects the steady-state deformation as well. Feng (1999) performed a numerical study of the effects of charge convection on the steady-state leaky dielectric solution. Among other results, he generated plots of the charge distribution along the boundary, some of which showed

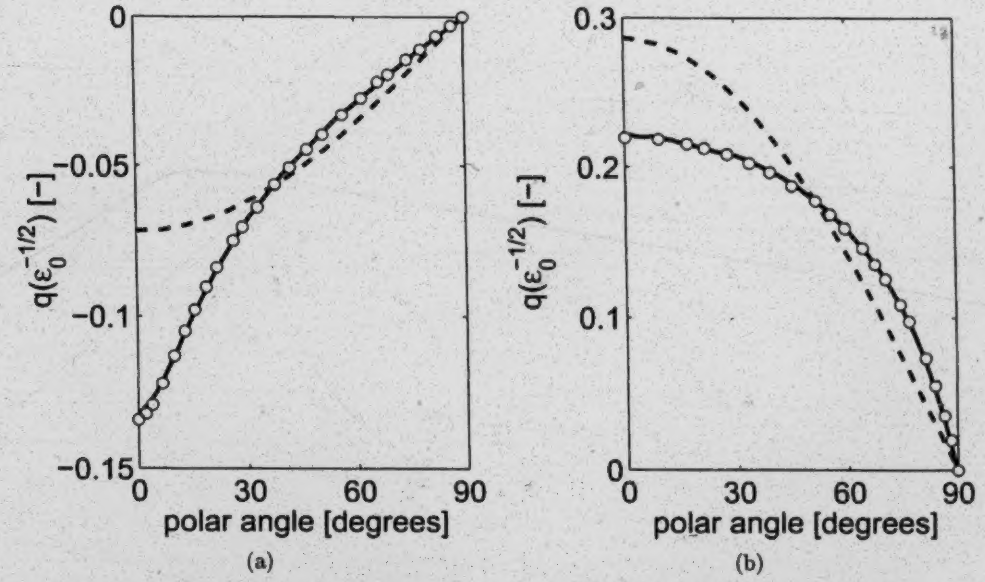

(a) (b)

Figure 4.11: Steady-state charge distribution on the drop interface, calculated both with and without convection. The solid lines are results from the present work with convection and interfacial dilation accounted for. The dashed lines are obtained from the static model. The open circles are from Feng (1999), Figures 3a and 4a, for comparison.

substantial differences from the static case without convection.

Figure 4.11 shows the effect of convection on the steady-state interfacial charge distribution, for two different cases. The parameters are taken from Feng (1999). Figure 4.11a was generated with the parameter set given in Table 4.3, additionally specifying a conductivity ratio σ_i/σ_e of 0.625 and an ionic concentration in the continuous phase of 3.214×10^{-12} M. This yields a conductive relaxation time of 2.5 s from Equation 3.4. Figure 4.11b was generated with the same parameter set, but with a conductivity ratio of 0.1 and an increased ionic concentration of 1.607×10^{-11} M, leading to a faster conductive relaxation time of 0.5 s.

It may be seen from both figures that the results from the present work are in substantial agreement with those of Feng (1999). Taylor's circulation in Figure 4.11a

Table 4.3: Common Parameters For Figures 4.11a and 4.11b

Applied Electric Field E_0	33607 V/m
Droplet Radius R_0	1 mm
Droplet Relative Permittivity ϵ_i	2.5
Medium Relative Permittivity ϵ_e	5
Interfacial Tension γ	0.001 N/m
Droplet Density ρ_i	1000 kg/m^3
Medium Density ρ_e	1000 kg/m^3
Droplet Viscosity μ_i	0.01 Pa·s
Medium Viscosity μ_e	0.01 Pa·s

is from equator to pole, and the charge distribution is skewed toward the z-axis (0° polar angle). There is a substantial peak in free charge density near the pole, which appears to be well described by the present model, based on its agreement with the earlier result.

Figure 4.11b displays pole-to-equator flow, due to the reversal of the sign of the charge distribution. This occurs because the conductivity ratio between the drop and the medium is now less than the permittivity ratio, whereas in the previous case it was greater. This case displays a flattening of the free charge distribution in the area of the pole, caused by convection toward the equator. In both cases, results from the present model are in good agreement with those of Feng (1999), indicating that the treatment of convection on the interface is correct.

4.4 Large Deformations: Agreement With Prior Numerical Studies

The problem of dynamic droplet deformation in an electric field has been solved numerically by Hirata et al. (2000). Their work was restricted to the leaky dielectric problem with the equilibrium (static) boundary condition. The results obtained by Hirata et al. cover a larger subset of the present model's capabilities than the analytic results do, and large-deformation results from their work may be directly compared with static-interface-charge leaky dielectric results from the present model.

4.4.1 Free Oscillation at High Reynolds Number

The first result shown in Hirata et al. is a verification problem, in which they compare their own code with that of Basaran [Basaran, 1992]. Basaran's paper did not examine the electrical problem; it was a study of nonlinear droplet oscillations. The case under study is a droplet of fluid in air (a "dynamically inactive" medium, or one having a negligible effect on the droplet fluid mechanics), with a predicted Reynolds number $\sqrt{\rho_i \gamma R_0/\mu_i^2}$ of 100. It is released from a spheroidal initial shape having a prolate aspect ratio of 2:1. The damping ratio is quite low, and the problem is far from the Stokes regime, so it represents a significant test of the code's robustness.

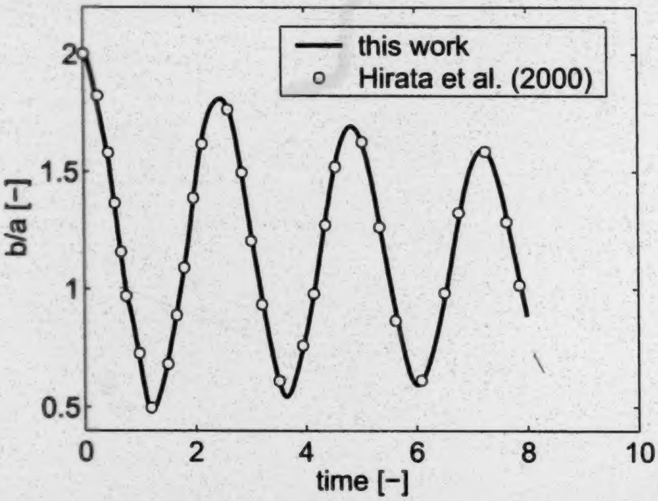

Figure 4.12: Comparison of the current model with that of Hirata et al. (2000) for a drop starting from a spheroidal shape with a 2:1 aspect ratio ($d = 1/3$). The drop Reynolds number as defined by Basaran (1992) is 100, and the surrounding fluid exerts negligible stress on the droplet.

Figure 4.12 is a comparison of the present model with that of Hirata et al. (2000) for this specific instance. The presence of higher-order harmonics is most clearly apparent as a slight concavity in the bottom half of the first descent; this occurs because the initial spheroidal shape does not correspond exactly to the second spherical harmonic [Basaran, 1992]. The close agreement between these two results is a good validation of the fluid mechanics component of the present model.

4.4.2 Large Electrically Induced Deformation

Figures 4.13 and 4.14 compare the present model with results in Hirata et al. The parameter sets for these curves are taken from Tsukada et al. (1993) and represent a combination of silicone oil with a mixture of corn oil and castor oil. The system consisting of a droplet of silicone oil in the mixed oil is called 'case 1' in Tsukada et al., and the reverse is called 'case 3'. Case 2 was a fictitious system in which the Taylor model predicted no deformation regardless of applied field; it is not treated here. The relevant parameters are listed in Table 4.4, including the applied field used in the dynamic simulations.

Figure 4.13 shows simulations of case 1. The first curve (a) is the basic droplet response, representing the physical system with no modifications. The second curve (b) is done with the internal viscosity multiplied by 100, *i.e.* $\kappa_2 = 6.80$. The third curve (c) is obtained with the same parameters as (a), but with the tangential elec-

Table 4.4: Parameters for Figures 4.13 and 4.14

Parameter	Definition	Case 1	Case 3
H	σ_i/σ_e	0.016	62.9
S	ϵ_i/ϵ_e	0.581	1.72
M	μ_i/μ_e	0.068	14.7
N	ρ_i/ρ_e	1.0	1.0
Ca	$\mu_e^2/(2\rho_e\gamma R_0)$	4.56	0.021
E^H	$E_0\sqrt{8\pi\epsilon_0\epsilon_e R_0/\gamma}$	7.0	2.5

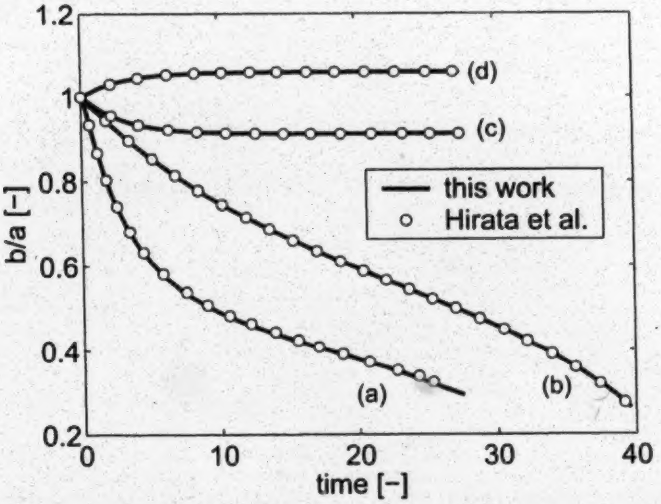

Figure 4.13: Comparison of numerical results with equivalent cases from Hirata et al. (2000): Case 1.

trical stresses removed from the boundary condition. The last curve (d), at the top, is the perfect dielectric equivalent case to (a). The aspect ratio b/a is plotted rather than d, with the time axis in units of $t\mu_e/4\rho_e R_0^2$, as in Hirata et al. (2000).

Agreement between the present model and that of Hirata et al. is excellent in this case. The results match almost exactly, despite the fact that the (a) curve at the end of the run is on the verge of developing a sharp edge around the equator. Such a singularity behaves in a method-dependent fashion, requiring fine discretization and time stepping in order to follow it accurately.

Another case where a comparison of interest can be made is in case 3, where Hirata et al. obtain a dynamic response which is apparently just on the far side of stability. The droplet rapidly reaches an intermediate plateau where it remains, deforming slowly, for a substantial period. It then seems to encounter a severe nonlinearity and elongates rapidly without bound.

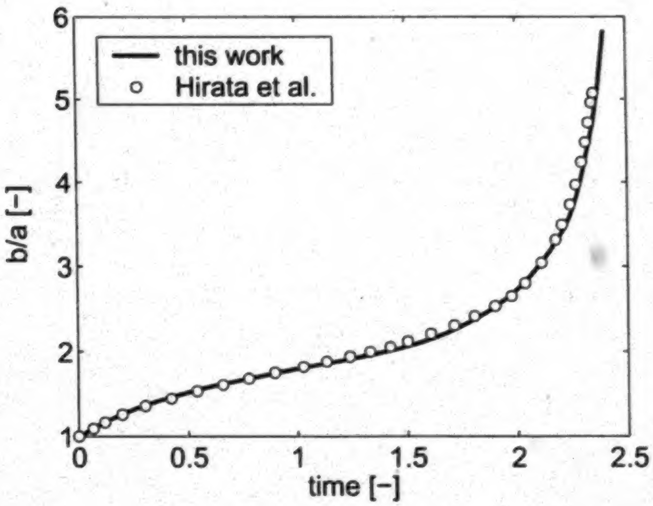

Figure 4.14: Comparison of numerical results with equivalent cases from Hirata et al. (2000): Case 3.

Figure 4.14 shows the comparison between the present model and that of Hirata et al. (2000) for the case described above. Once again, the agreement is good, if slightly less so than before. The pole of the drop in this case is pulled out into a long, thin extension before breakup, which distorts the electric field strongly and causes the numerical problem to become stiff.

The interfacial mesh used here was generated with 'Hmax' = 0.05, and the time step was 0.06 radians. If the interface resolution is increased further, a substantial reduction in the time step is necessary to achieve convergence. However, the instability seen in Figures 4.2 and 4.3 does not appear in this case except for relatively large time steps. This problem is a counter-example to the generalization made earlier that the model can be considered accurate if the time step is small enough to stabilize the interfacial mesh motion.

4.5 Comparison With Experiments

Lu (2002) reported experiments in which drops of water were suspended in organic solvents in both the presence and absence of surfactants and bitumen. One of the control tests was a series of measurements of the deformation of a drop of water in decyl alcohol. This experiment was duplicated numerically in this study, and Figure 4.15 shows the results.

The Weber number is defined as:

$$We = \frac{\epsilon_0 \epsilon_e R_0 E_0^2}{\gamma} \tag{4.9}$$

The value of the interfacial tension used in the simulations was 0.0089 N/m, as reported in Lu (2002).

The figure presented by Lu incorporates a linear regression through the data,

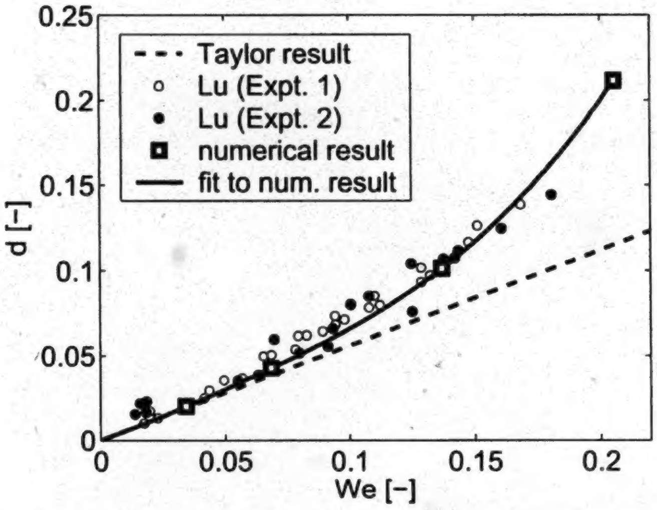

Figure 4.15: Steady-state deformation parameter plotted against Weber number for water in decyl alcohol: Comparison with Lu's results.

passing through zero and having a slope greater than that of the Taylor result. While the use of a straight line does seem natural from the visually apparent distribution of the data, the results of the numerical simulation suggest an alternative. The nonlinear departure from Taylor's result observed in the numerical simulations for this case is gentle enough that it provides a possible explanation for the observed trend. The agreement between simulation and experiment seen here is encouraging.

This chapter was focused on model validation with analytic, numerical and experimental results from the literature. With confidence in the model's accuracy established, the next chapter proceeds to explore the parameter space more fully.

CHAPTER 5

RESULTS AND DISCUSSION

5.1 Perfect Dielectric Results

5.1.1 Small Deformations

In the foregoing chapter, it was established that the perfect dielectric model produces results in good agreement with linear theory when deformations are small. Without departing from the small-deformation region, the analysis can be expanded to include variation in several base parameters. This is useful because the analytic dynamic results are only a first-order approximation, and it is helpful to be able to predict the system dynamics with a high degree of accuracy.

For the case of the perfect dielectric system, variation in the electrical problem affects only the magnitude of the resulting step response; the shape of the response does not change substantially. Therefore the parameters of interest in small-deformation perfect dielectric systems are primarily those of the fluid mechanics problem. The base case in Table 4.1 is taken as a starting point, and parameters are varied as in Table 5.1. This yields a range of dynamics where the ratio between interfacial tension and viscous forces is not extreme.

In Figure 5.1a, the viscosity of the continuous phase is held fixed at 0.001 Pa·s while the droplet viscosity is varied between 0.0001 and 0.01 Pa·s. Figure 5.1b rep-

Table 5.1: Range of Parameters for Small-Deformation Perfect Dielectric Simulations.

Interfacial Tension γ	0.01 - 0.07 N/m
Viscosity μ_i, μ_e	0.0001 - 0.01 Pa·s
Density ρ_i, ρ_e	500 - 1000 kg/m^3
Droplet Radius R_0	1 - 100 μm

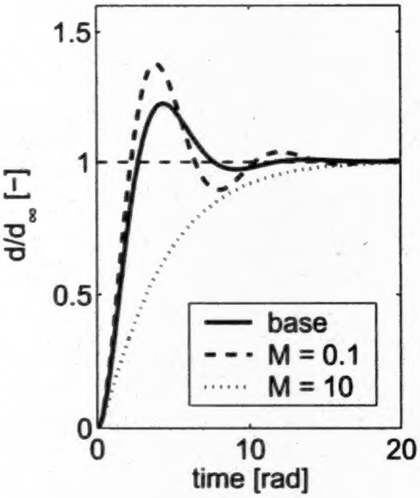

(a)

(b)

Figure 5.1: Effect of (a) droplet viscosity and (b) continuous phase viscosity on perfect dielectric dynamic response. M is the viscosity ratio, μ_i/μ_e.

resents the opposite case, in which the viscosity of the continuous phase was varied from 0.0001 to 0.01 Pa·s while the droplet viscosity was held fixed at the central value of 0.001 Pa·s. The plots are normalized by the OTAM result for steady-state deformation and by the theoretical inviscid natural frequency of the droplet. However, since these values are identical for all the cases shown, plotting the unscaled physical results would not change the geometric relationships between the curves.

Varying one viscosity while keeping the other fixed causes a change in the overall viscous damping of the system. The responses for lower viscosity show increased oscillatory behaviour, indicating lower damping, while those with higher viscosity show monotonic, non-oscillatory responses indicating overdamping. The time scale of the oscillation is shorter for the lower-viscosity cases, which is consistent with the expected behaviour of a damped dynamic system. It is also notable that changing the external viscosity appears to have a more pronounced effect than changing the internal viscosity.

This behaviour is in accordance with Whitaker's result for damping time. Equation 4.5 contains the expression $6\mu_i^2\rho_i + 16\mu_e^2\rho_e$, which are the only terms in the equation in which the two viscosities are separate. The term containing only the external viscosity has a coefficient of 16, whereas the corresponding term for the internal viscosity has a coefficient of 6. The total effect of viscosity is more complex than a simple proportionality, as an inspection of Equation 4.5 readily shows; however, the general trend seen in Figure 5.1 is expected based on the theory.

Figure 5.2 shows the effect of reducing the density of either the droplet or the continuous phase to 500 kg/m^3 while maintaining the other at the base value of 1000 kg/m^3. Both variation curves are plotted together with the base case. The normalization does not affect the geometric relationship between the curves.

It may be noted that reducing either density produces an increase in the apparent damping of the system; that is, the response is less oscillatory and has a lower peak. Furthermore, the density of the droplet has a greater effect than that of the surrounding fluid. It appears that the inertia of the droplet, at least in this range of parameters, is more important to the dynamics than that of the surrounding fluid.

This is expected based on the importance of the parameter β, which is proportional to $(2\rho_e + 3\rho_i)$, in the denominator of Equation 4.5. The coefficients of 2 and 3 in β for the external and internal densities, respectively, are congruent with the observed

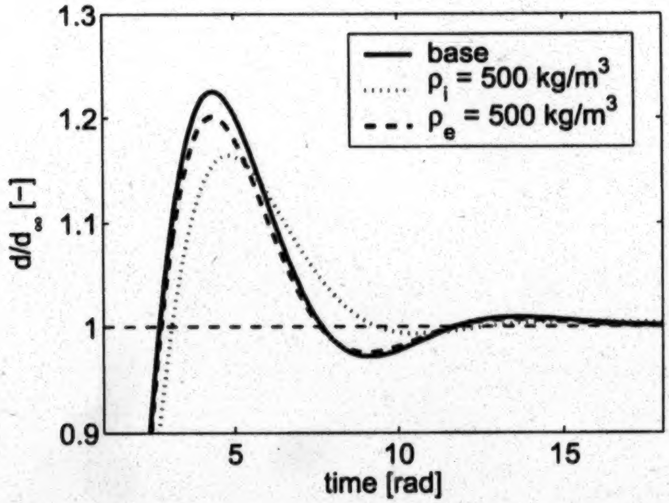

Figure 5.2: Effect of droplet and continuous phase density on the dynamic response of the perfect dielectric model.

result. Once again, the relationship between density and damping is not a simple proportionality when the whole of Equation 4.5 is considered, but it may be seen that the results obtained here are consistent with the form of the analytic result.

In Figure 5.3, interfacial tension is varied between 0.01 and 0.07 N/m, keeping all other parameters constant. The results shown here are normalized by the inviscid natural frequency and OTAM result, which vary substantially with γ; therefore the normalized plot masks some of the variation between cases.

It may be seen from Figure 5.3 that the oscillatory behaviour of the system varies substantially with γ, and the less-damped oscillations correspond to higher values of the interfacial tension. These cases also show slightly faster oscillations than the more heavily damped, lower-γ cases. This is consistent with the interpretation of γ as a zero-order, or position-related, restoring force, which in the context of a dynamic system provides the system's stiffness.

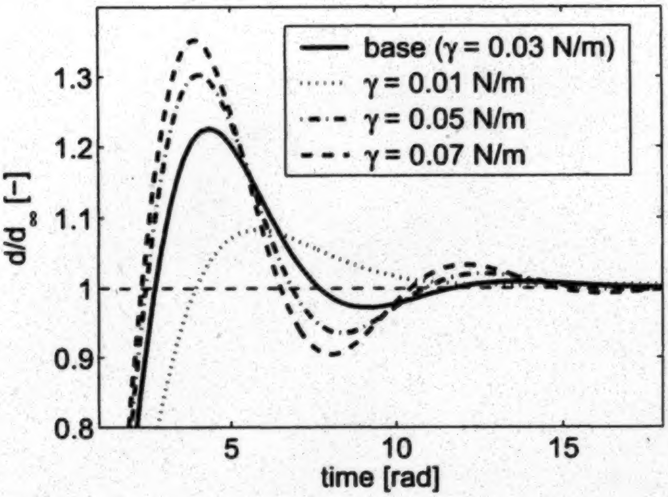

Figure 5.3: Effect of interfacial tension on the dynamic response of the perfect dielectric model.

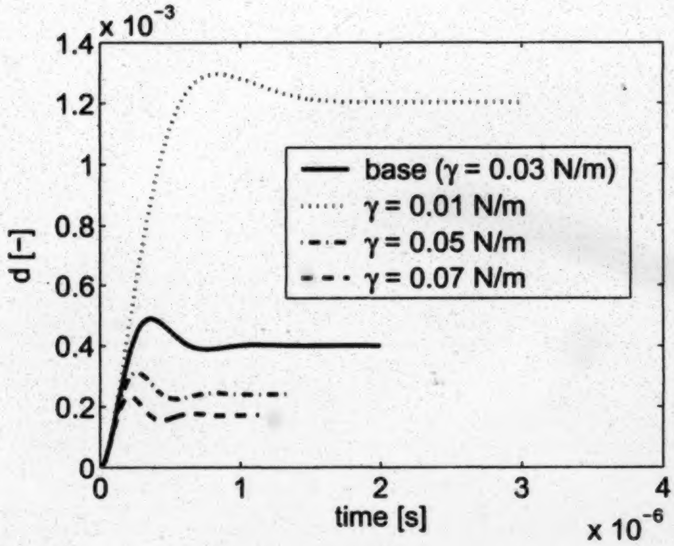

Figure 5.4: Fully dimensional plot of the effect of interfacial tension in the perfect dielectric model.

A substantial increase in oscillation speed and a decrease in equilibrium deformation are expected based on the theory, but this is not evident in the normalized plot in Figure 5.3. Therefore it is useful to plot these same results without the normalization, as in Figure 5.4.

Figure 5.4 is a fully physical replot of the results in Figure 5.3. The subtle differences in the shapes of the damped responses are not as evident, but the large-scale changes produced by altering the stiffness of the system can be clearly seen. By considering both Figure 5.3 and Figure 5.4, it may be seen that the effect of interfacial tension on oscillation time and equilibrium deformation is well modeled.

Figure 5.5 shows the effect of increasing the size of the droplet. The base case, at $R_0 = 1\ \mu$m, is plotted along with results for 10 and 100 μm droplet radii. No other parameters are varied. The time scale and equilibrium deformation vary dramatically in this case, so the results are presented in normalized format.

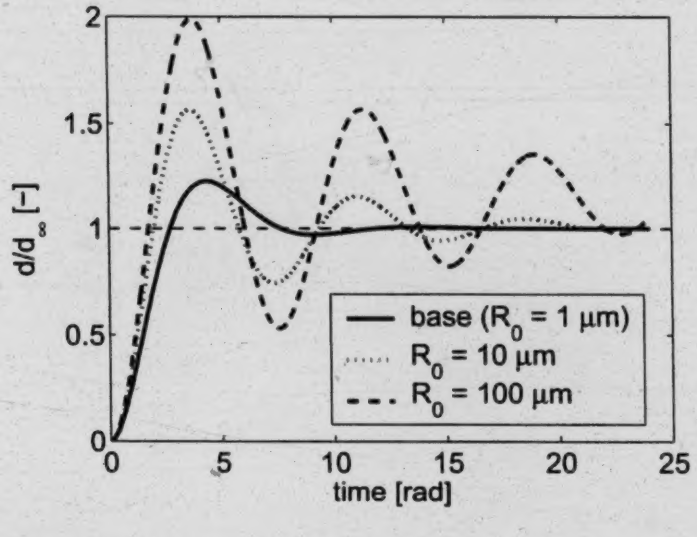

Figure 5.5: Effect of droplet size on the dynamic response of the perfect dielectric model

It may be seen from Figure 5.5 that the agreement with the theoretical deformation value is good, and the time scale of the oscillation is relatively consistent. The increased oscillatory behaviour of the larger drops is expected, once again, from Equation 4.5. It can be shown that the damping rate decreases faster than the oscillation rate for this case, so that although the larger droplets oscillate more slowly in an absolute sense, their dynamic responses are more lightly damped. It may be noted that the 100 μm case does not converge exactly to the analytic limit. This is because the analytic deformation (see Equation 2.7) is linearly proportional to the drop size, so the deformation in this case is 100 times as large as for the 1 μm-radius droplet, and some nonlinearity is expected.

The results thus far appear intuitively correct and are elementary in that they do not show significant effects that cannot be predicted by theory. The strength of a numerical model is the prediction of nonlinear effects that cannot be described easily or at all by analytic techniques. To observe such effects in the perfect dielectric case we must increase the deformation substantially, and the simplest way to do that is to increase the applied field.

5.1.2 Large Deformations

Figure 5.6 shows the dynamic response for fields ranging from the base value of 1 MV/m to a maximum value of 20 MV/m. All other parameters are those of the base case in Table 4.1. The equilibrium shape of the droplet in the 10 MV/m case is shown in Figure 5.7a, and Figure 5.7b shows the deformed shape of a droplet subjected to 20 MV/m as it appears at the end of the simulation.

Increasing the field past 10 MV/m in the base case results in substantial nonlinearity. The electrical stress is proportional to the square of the local field, so deformation increases rapidly with applied field. Figure 5.7a illustrates the high

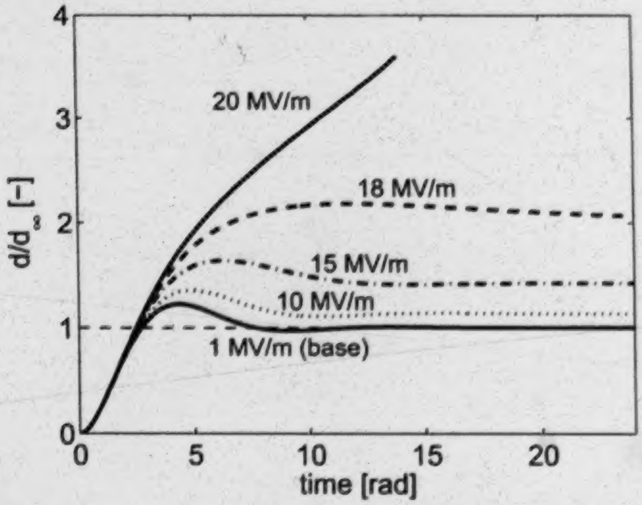

Figure 5.6: Normalized dynamic responses for high applied fields, using the perfect dielectric model.

degree of deformation resulting from a tenfold increase in applied field over the base case. The nonlinearity induced by asphericity of the prolate droplet under high applied fields results in a uniformly positive divergence from the linear result. In particular, the deformation in the 20 MV/m case appears to have no steady-state value; it develops pointed tips as shown in Figure 5.7b, and the numerical method breaks down due to a singularity in the boundary curvature description. This occurs at a deformation parameter of 0.593, corresponding to an aspect ratio of 3.91. In physical systems, the development of the pointed tip precedes the emission of fluid strands and/or satellite droplets from the pole of the main droplet [Allan and Mason, 1962, Ha and Yang, 1998]. This phenomenon is known as tip streaming, and occurs when the drop permittivity is large relative to the continuous phase [Garton and Krasucki, 1964, Rosenkilde, 1969, Sherwood, 1988].

It may be observed that the apparent damping ratio goes up as the deformation in-

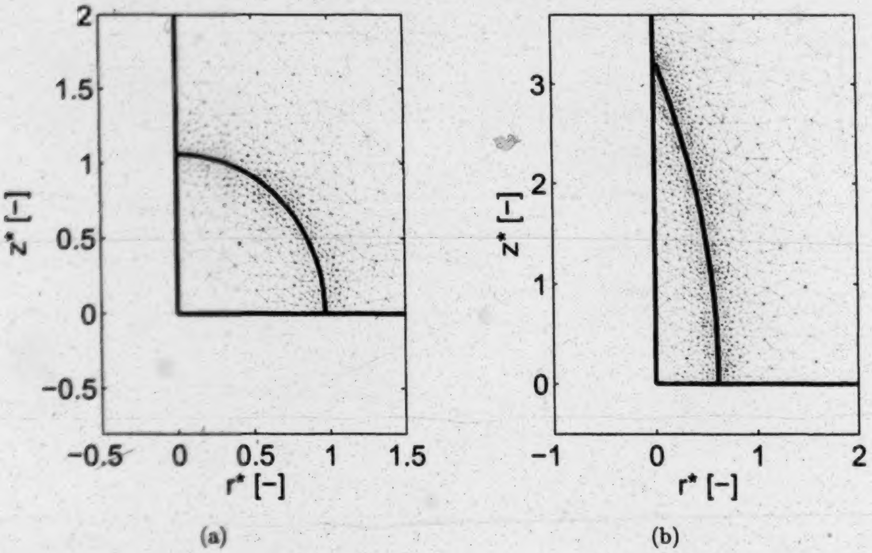

Figure 5.7: Deformed droplet shape at end of run for an applied field of (a) 10 MV/m and (b) 20 MV/m.

creases. This may be because the nature of the nonlinearity is such that the electrical forcing increases with the asphericity. Since the droplet starts out with an acceleration appropriate to a lower equilibrium deformation than it eventually achieves, less momentum is carried into the high-deformation region, and the overshoot decreases as compared with a more nearly linear system. The extreme case, with unbounded deformation, illustrates this effect well: the droplet decelerates as though towards an equilibrium, but the electrical forcing on the deformed droplet increases with deformation, resulting in an inflection point where the deformation rate begins to increase in an unstable fashion.

Given that deformation of the drop increases its tendency to deform further, it might be expected that reducing the viscosity of a marginally stable system might produce an unstable system, due to the increase in magnitude of the initial oscillatory

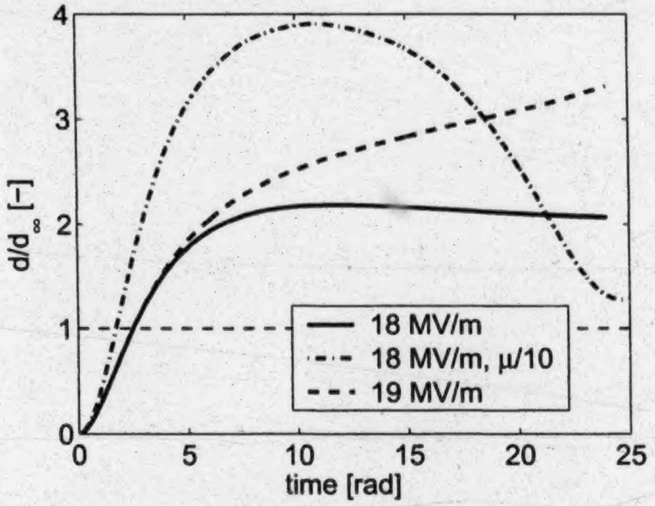

Figure 5.8: Normalized dynamic responses at the limit of stability, using the perfect dielectric model.

peak. Figure 5.8 shows responses from the base case at 18 MV/m and 19 MV/m, along with a case at 18 MV/m where both fluid viscosities have been reduced to 0.0001 Pa·s, or 1/10 of the base case value.

The 18 MV/m case in Figure 5.8 is stable, as was observed previously. The 19 MV/m case appears to be unstable; that is, it is increasing without bound. However, the 18 MV/m case with reduced viscosity is stable, despite a large initial oscillatory peak. This peak represents substantially greater deformation than the value of the inflection point on the 19 MV/m plot, and the deviation from sinusoidal behaviour may be clearly seen. Nevertheless it is oscillating in a stable manner.

It was hypothesized that reducing the viscosity of a drop at the limit of stability, without changing the applied field, could cause the drop to become unstable due to dynamic effects. The stability of the reduced-viscosity system in Figure 5.8 does not support this conjecture. It indicates that if there is a range of applied fields in which

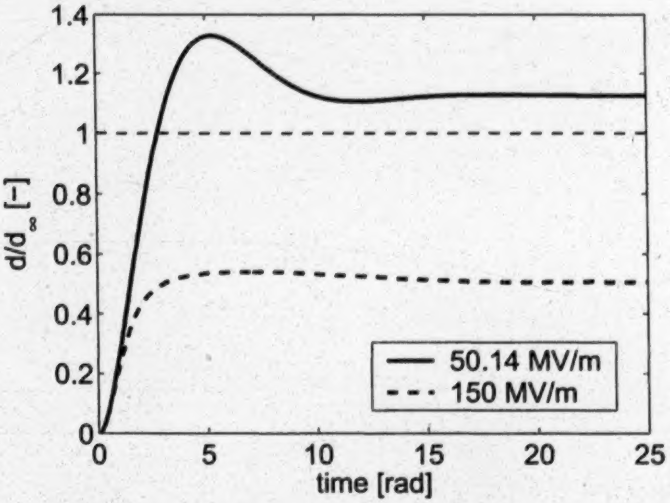

Figure 5.9: Normalized dynamic responses for high applied fields in the perfect dielectric base case, but with the drop permittivity reduced from 80 to 8.

a more viscous drop is stable but a less viscous drop is not, it is is quite narrow, at least for this specific parameter set.

According to Garton and Krasucki (1964), the breakup of drops by tip streaming occurs only for permittivity ratios ϵ_i/ϵ_e greater than approximately 20. The permittivity ratio in the base case is 80/3, or 26.7, so this behaviour is expected. In cases with a lower permittivity ratio, it is expected that the droplet will remain stable for arbitrarily large values of the applied field. Figure 5.9 illustrates this.

Figure 5.9 shows the effect of reducing the permittivity of the drop from 80 to 8, thus reducing the permittivity ratio ϵ_i/ϵ_e from 26.7 to 2.67. The vertical axis is normalized by the OTAM result. Two applied fields are used: 50.14 MV/m and 150 MV/m. The applied field of 50.14 MV/m was chosen because it results in the same analytically predicted OTAM deformation ($d_t = 0.1597$) as the 20 MV/m case in Figure 5.6.

It may be seen that both responses in Figure 5.9 possess a stable equilibrium. The 50.14 MV/m case shows an increase over the analytically predicted value, as indicated by its steady-state deformation exceeding 1 on this normalized plot. However, the 150 MV/m case is substantially less deformed than the theory predicts. This is because at this applied field, the predicted deformation is 1.429, which is physically impossible due to the fact that $d = 1$ corresponds to an infinite aspect ratio.

The difference between the nonlinear numerical result and the OTAM deformation is not monotonic in this case. For small deformations, the OTAM result is valid, and according to Figure 5.9, increasing the deformation substantially produces a positive nonlinearity; that is, the droplet deforms further than the theory predicts. As the applied field increases even further, this trend reverses, and the nonlinearity becomes negative. This implies that at some point the steady-state deformation must pass through the analytically predicted result, so that the error in the OTAM result must be zero for some nonzero value of the applied field.

Figure 5.10 shows the steady-state shapes of the drops in Figure 5.9, in which the drop permittivity has been reduced by a factor of 10. Figure 5.10a represents the steady state for an applied field of 50.14 MV/m. This applied field was chosen to produce the same predicted OTAM deformation as that of the unstable case in Figure 5.7b. Figure 5.10b represents the steady state resulting from an applied field of 150 MV/m on the same drop.

The drop in Figure 5.10a is far from being as deformed as its counterpart in Figure 5.7b. The nonlinearity in the high-permittivity-ratio case of Figure 5.7b resulted in a deformation parameter at breakup of nearly four times the analytic value, but here the equilibrium deformation is only 12.4% greater than the analytically predicted value. This may be because the lower permittivity ratio results in a more moderate electric field distortion, which is less sensitive to changes in the drop geometry.

Figure 5.10b shows a deformation similar to that in Figure 5.7b. However, this

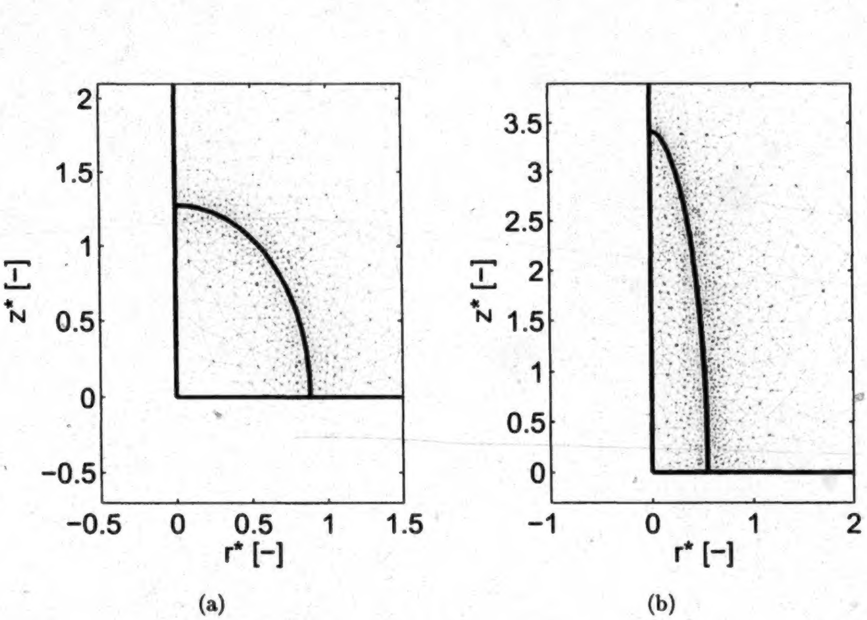

(a) (b)

Figure 5.10: Deformed droplet shape at steady-state for $\epsilon_i/\epsilon_e = 2.67$ and an applied field of (a) 50.15 MV/m and (b) 150 MV/m.

deformation is actually lower than that predicted by the OTAM result, largely because the OTAM result becomes nonphysical ($d > 1$) at such an extreme applied field. The drop in Figure 5.10b shows no sign of the unstable pointed tip in Figure 5.7b. Rather, it has a rounded end despite the severity of the deformation. Most importantly, it is stable; Figure 5.10b represents a steady-state profile, whereas Figure 5.7b represents the instantaneous drop profile just before tip streaming/breakdown of the numerical method. The stability of this system with low permittivity ratio is in accordance with the predictions of other researchers [Garton and Krasucki, 1964, Miksis, 1981].

5.2 Leaky Dielectric Results

5.2.1 Small Deformations

For small deformations the static-boundary leaky dielectric model shows very similar dynamics to the perfect dielectric model, with the exception that the deformation can be negative, or zero. The leaky dielectric case in general is characterized by tangential electrical stresses on the drop surface, resulting in steady-state flow along the interface and persistent circulatory flow patterns inside the droplet. The full leaky dielectric model can show strong effects of the boundary charge dynamics, and convective transport of charge along the interface can alter the steady-state value of the deformation.

The parameters used in the leaky dielectric model are the same as in Table 4.1, with the addition of a pair of conductivities. These are calculated from Equation 3.5, given a set of ion characteristics combined with a temperature and partition coefficient

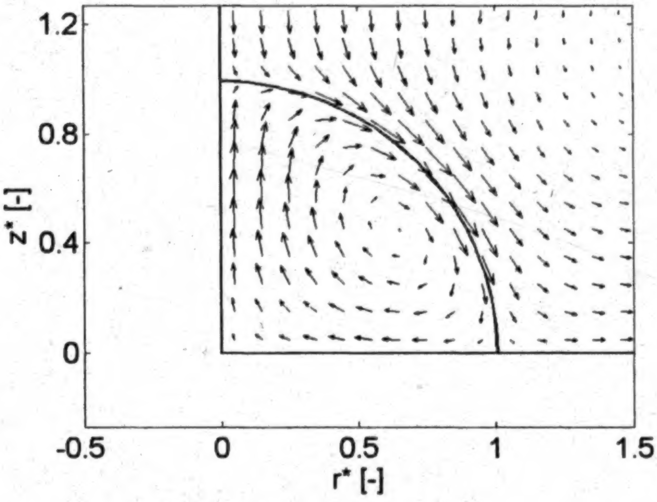

Figure 5.11: Steady-state circulation in the static leaky dielectric model.

Table 5.2: Leaky Dielectric Base Case

Applied Electric Field E_0	1 MV/m
Droplet Radius R_0	1 μm
Droplet Relative Permittivity ϵ_i	80
Medium Relative Permittivity ϵ_e	3
Interfacial Tension γ	0.03 N/m
Droplet Density ρ_i	1000 kg/m^3
Medium Density ρ_e	1000 kg/m^3
Droplet Viscosity μ_i	0.001 Pa·s
Medium Viscosity μ_e	0.001 Pa·s
Medium Ionic Concentration c_e	0.04 mol/m^3 (4×10^{-4} M)
Ion Partition Coefficient (i/e) α	1.0
Positive Ion Valence z^1	1
Negative Ion Valence z^2	-1
Droplet +ve Ion Diffusion Coefficient D_i^1	10^{-9} m^2/s
Droplet −ve Ion Diffusion Coefficient D_i^2	10^{-9} m^2/s
Medium +ve Ion Diffusion Coefficient D_e^1	10^{-9} m^2/s
Medium −ve Ion Diffusion Coefficient D_e^2	10^{-9} m^2/s
System Temperature T	298 K

($\alpha = c_i/c_e$). The relevant ion characteristics are the absolute concentration in the continuous phase (c_e), valence of each ion (z^1, z^2), and diffusion coefficient (D_i^1, D_i^2, D_e^1, D_e^2). This allows a fully physical description, as in the perfect dielectric case. This is done in both the static and full leaky dielectric models, even though the static model only requires a conductivity ratio. Table 5.2 gives the full parameter set.

Figure 5.11 illustrates the steady-state velocity field for the base case as outlined in Table 5.2. This velocity plot results from solving the dynamic problem to equilibrium, which in this case is adequately achieved at a solution time of 24 radians based on the inviscid natural frequency. The static leaky dielectric model is used.

In Figure 5.11, the circulation within the drop, known as a Taylor vortex, can be clearly seen. The stress along the boundary induces tangential flow, which results in a circulatory pattern inside the droplet and an approximately hyperbolic profile outside

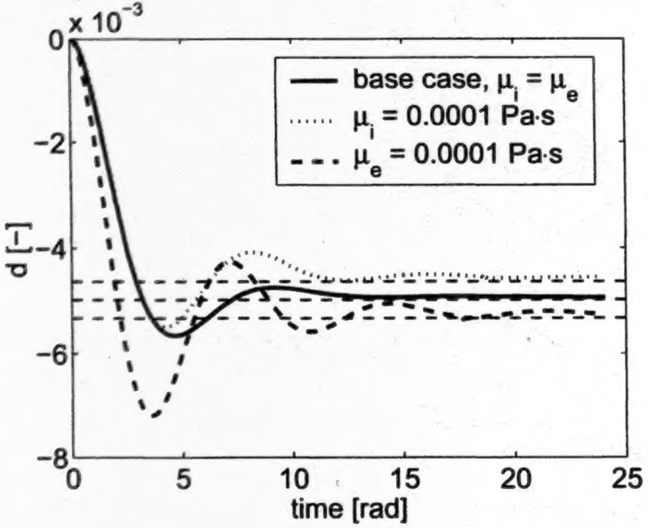

Figure 5.12: Effect of viscosity on leaky dielectric response.

it. This matches the effect predicted by Taylor (1966) and observed by McEwan and de Jong in an addendum to the same paper.

Figure 5.12 shows the response of the static leaky dielectric model to variation of the internal and external viscosity. In this illustration, the base case with $\mu =$ 0.001 Pa·s is shown along with two cases of reduced viscosity, one with the internal viscosity reduced by a factor of 10, and another with the external viscosity reduced by the same factor of 10. This plot is not normalized in the vertical axis. Taylor's result for each case is shown as a dashed line.

As in the perfect dielectric case, the damping rate of the system is strongly affected by viscosity. The external viscosity has a greater effect on the damping than the internal viscosity. Once again, the time axis is the same in all three cases; the normalization on that axis does not affect the geometry of the plot.

It should be noted that in the leaky dielectric problem, the viscosity affects the steady-state as well as the transient. Here the viscosity ratio appears to be the relevant

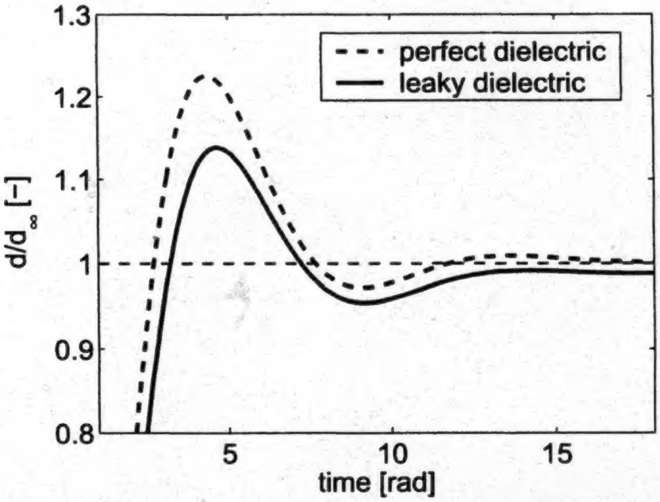

Figure 5.13: Superimposition of normalized perfect and leaky dielectric results, for comparison of the dynamics.

parameter, since reducing the external viscosity has exactly the opposite effect on the steady-state versus reducing the internal viscosity. This is in accordance with the Taylor theory, in which the absolute viscosity does not appear, but only the ratio.

Figure 5.13 shows the perfect and leaky dielectric base cases normalized and superimposed on one another. The parameter sets are the same as those used in Tables 4.1 and 5.2. Applied field is 1 MV/m. The static leaky dielectric model is used.

Figure 5.13 demonstrates that the overshoot of the leaky dielectric model is substantially less than that of the perfect dielectric model, given the same fluid mechanical system. The steady-state deformation is also marginally less relative to the analytic result, showing a difference on the order of approximately 0.5%.

The steady-state error is most likely due to the fact that the equilibrium state in the leaky dielectric solution is dynamic, and errors in the fluid mechanics solution can have a systematic effect on the steady-state deformation. The reduced damping may

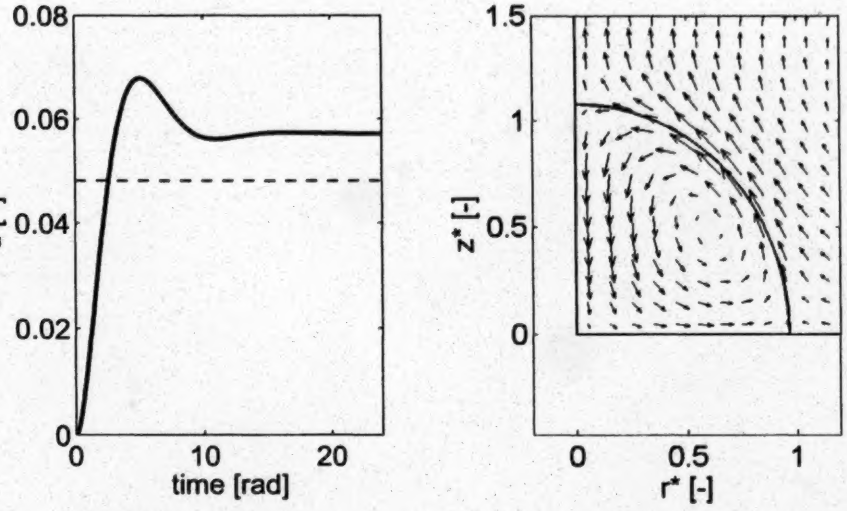

(a) (b)

Figure 5.14: Prolate deformation of a leaky dielectric droplet due to large ion partition coefficient for the drop.

be due to the fact that a significant part of the deformation of the leaky dielectric droplet is a secondary effect resulting from the development of the Taylor vortices, which require a finite amount of time to develop. This reduces the initial acceleration of the droplet relative to its final position, producing an effect similar to what was described in Section 5.1.2. That effect was discussed as a possible explanation for the reduced overshoot at high applied field in the perfect dielectric case.

Figure 5.14 shows one possible result of altering the ion partition coefficent α between the droplet and the continuous phase. Here $\alpha = 100$, and all other parameters are as in the base case. The applied field is 10 MV/m, and the static leaky dielectric model is used. The dashed line indicates the analytic prediction from Taylor's result.

The deformation in this case is not oblate as with previous instances of the leaky dielectric model. Due to the alteration of the partition coefficient, the conductivity

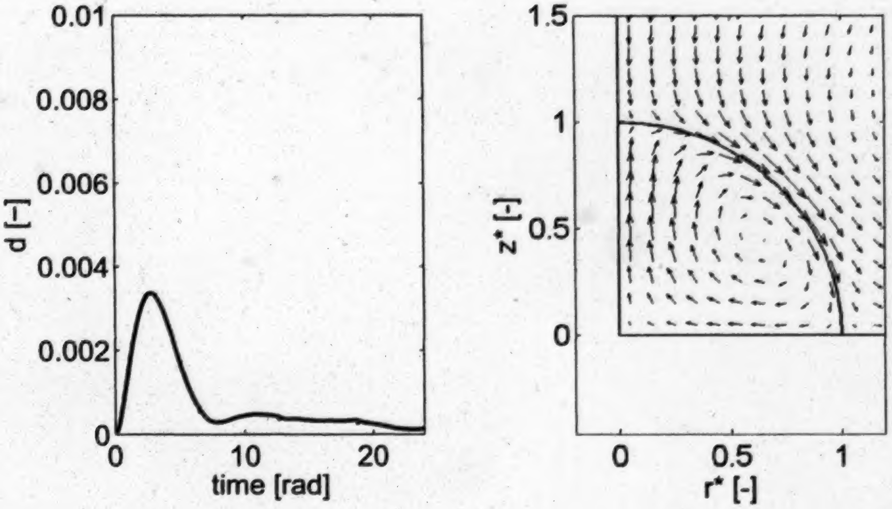

(a) (b)

Figure 5.15: Dynamic response and steady-state flow pattern for parameters leading to an analytically predicted deformation of zero.

ratio has changed substantially, and the deformation in this case is prolate. It may be noted that the Taylor circulation inside the drop is now in the equator-to-pole direction, or opposite to the base case of Figure 5.11. It may also be noted that the deformation is not exactly as predicted by linear theory, but looks somewhat similar to the 10 MV/m case in Figure 5.6.

Taylor's result can predict either prolate or oblate deformation depending on the parameter ratios of the system under examination, particularly the conductivity ratio. The result shown here demonstrates this effect. It also illustrates a nonlinearity similar to what was observed in the perfect dielectric case for large fields; namely, that the deformation is larger than that predicted by the linear theory.

Figure 5.15 is obtained by setting α to a value that results in Taylor's solution predicting no deformation. This value, for the base case parameters, is approximately

8.8882. The applied field in this test is 10 MV/m. The static leaky dielectric model is used.

The deformation in this case is substantially smaller than the result for $\alpha = 100$. The deformation curve degenerates after an initial peak, and appears to be converging approximately to zero, although there is a substantial amount of discretization noise present. The flow pattern is from pole to equator.

Considering the large normal electrical force in this case that must be balanced by an equally large pressure gradient generated by the pole-to-equator flow, the error in this result is not unexpected. One interesting feature is the initial peak, which is probably a result of the aforementioned finite development time for the Taylor vortices. Initially the system is not in balance, because it is quiescent and the requisite pressure gradient to produce the predicted equilibrium has not yet developed. Later, as the vortices reach maturity, the problem converges back towards zero deformation.

5.2.2 Effect of Charge Dynamics

The full leaky dielectric model allows for finite-in-time charge buildup on the interface, as well as steady-state convection effects. This can have a profound effect on the overall response, both in terms of the initial transient and in terms of the steady-state deformation.

Figure 5.16 shows the effect of varying the ionic concentration in the leaky dielectric base case, starting with the static model and demonstrating the effect of lowering the absolute conductivity. In the base case, the conductivities of the two fluids are equal. The dynamic boundary simulations were done with monovalent ionic concentrations of 2×10^{-4} M and 4×10^{-5} M, leading to conductivity values of approximately 1.5×10^{-3} S/m and 3×10^{-4} S/m, respectively. The dashed line indicates the analytic deformation from Taylor's result.

The validity of the leaky dielectric model for a given system may be confirmed by

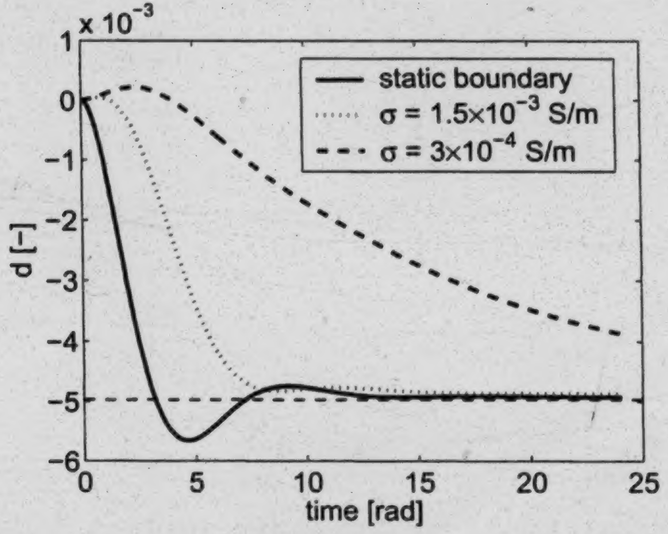

Figure 5.16: Dynamic contribution from charge relaxation on interface for various fluid conductivities in the full leaky dielectric model.

calculating the ratio of drop radius to the electrostatic double layer thickness given by Equation 3.6. For a concentration of 4×10^{-4} M with the base case parameters, this ratio is at a minimum in the drop, where it takes a value of 20.6. This value is much greater than 1, which indicates that the assumption of small double layer thickness is valid in this case.

The dynamic response of the static leaky dielectric model is very similar to that of the perfect dielectric model. However, the inclusion of charge dynamics increases the complexity of the response significantly. The dynamic boundary cases here show non-minimum-phase behaviour; their initial motion is away from the steady-state position they will eventually reach. In addition, the lowest-conductivity case shows a significant secondary time scale, slower than the droplet's oscillation frequency, by which relaxation to the final state occurs.

The reason for this behaviour is the finite charge buildup time. Initially, the

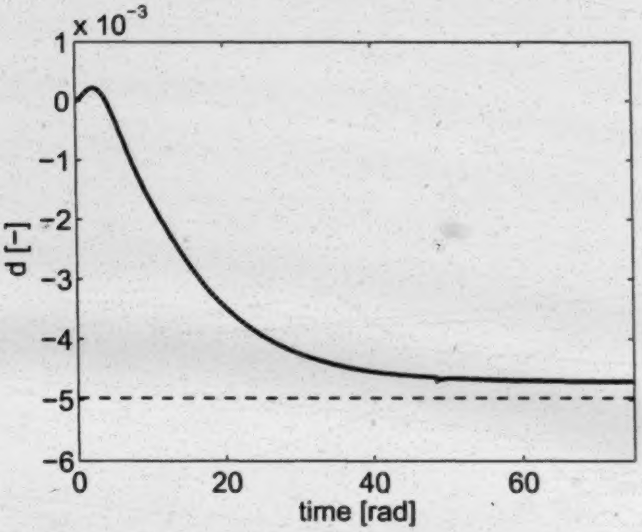

Figure 5.17: Steady-state offset from Taylor limit resulting from charge convection in the full leaky dielectric model.

boundary is uncharged, so the dynamic response begins identically to the perfect dielectric case. As the charge builds up, the droplet's deformation changes direction towards the leaky dielectric steady-state limit. If the charge relaxation is significantly slower than the drop oscillation, the transition to steady-state deformation is governed by the charge buildup. This effect is first-order and resembles an exponential; this can be seen in the lowest-conductivity case in Figure 5.16. In an extreme case with very low conductivity, the complete perfect dielectric transient oscillation might occur, followed by a slow, monotonic transition to the leaky dielectric steady-state limit.

Figure 5.17 shows the complete dynamic response of a leaky dielectric drop using the dynamic interfacial boundary condition. The parameters are those of the leaky dielectric base case, with an ionic concentration in both fluids of 4×10^{-5} M, leading to a conductivity of 3×10^{-4} S/m.

This result demonstrates the effect of charge convection along the drop interface on the steady-state deformation. The steady-state value predicted by Taylor's analytic result is shown by the dashed line; clearly, the steady-state value reached by the simulation is different from the analytic prediction. As mentioned in Chapter 4, the charge distribution on the interface is modified by the steady-state tangential flows associated with the leaky dielectric system. This effect alters the electrical stress distribution and can affect the steady-state deformation. As noted by Feng (1999), the result in the case of oblate deformation is a reduction of the steady-state deformation relative to the analytic result.

5.2.3 Large Deformations

The leaky dielectric model has a significantly wider range of behaviours than the perfect dielectric model due to the larger parameter set. The conductivity ratio in particular has a large effect on the dynamic response, and variations in it can produce significant differences in dynamics between systems.

Figure 5.18 shows the effects of increasing the applied field in the base case. The field is varied from 1 MV/m in the base case to a maximum of 20 MV/m. All results are normalized by the analytic deformation and inviscid natural frequency. The static leaky dielectric model is used.

In this figure, it can be seen that some of the same effects are present as in the perfect dielectric case, seen in Figure 5.6. The increase in applied field produces a nonlinear response, accompanied by a decrease in overshoot. However, it is notable that in this case the nonlinearity is in the opposite direction from that observed in the perfect dielectric base case of Figure 5.6. The high-field deformations are less extreme than predicted by Taylor's result, and all of them have steady-state values. The responses appear more like the results in Figure 5.9 for perfect dielectrics with low permittivity ratio.

Part of the reason for the reduced deformation at high fields is that the analytic de-

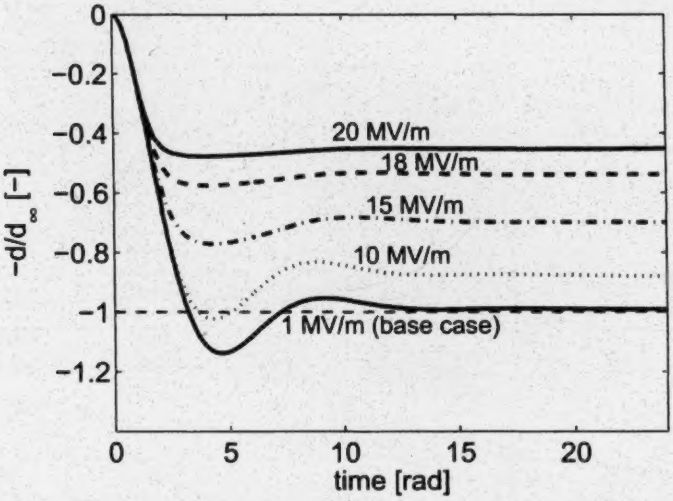

Figure 5.18: Effect of high applied fields on the static leaky dielectric response.

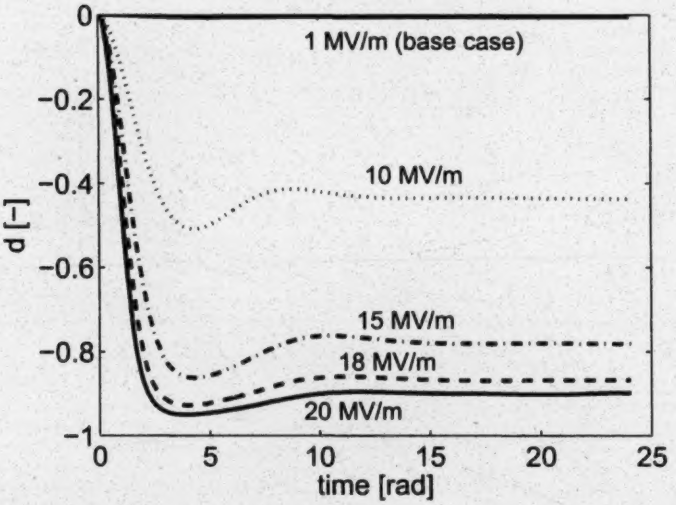

Figure 5.19: Effect of high applied fields on the static leaky dielectric response, with physical values of the deformation parameter.

formation parameter in these cases exceeds -1. This is a physical impossibility, since it requires a negative aspect ratio. The 20 MV/m case has a theoretical deformation parameter of -1.9885, but the numerical result gives only -0.898, which corresponds to an aspect ratio of 0.0539. This may be seen more clearly in Figure 5.19, which is a replot of the data in Figure 5.18 without normalization of the deformation parameter values.

Figure 5.19 shows deformation curves that appear to be asymptotically approaching -1 as the field increases. No instability is apparent, even for severely deformed drops. The reason for this is that the higher fields here produce droplets that are essentially squashed into thin disks, with most of the circulation occurring near the outer edge. No points or edges develop that might lead to jet ejection, and the drop does not tend to fragment. This may be seen in Figure 5.20.

In Figure 5.20, the deformed shapes and circulatory patterns in steady-state are shown. The 10 MV/m case in Figure 5.20a shows a substantial deformation that nevertheless appears approximately spheroidal. The flow pattern is similar to what is seen in lower-deformation cases. The 15 MV/m case, shown in Figure 5.20b, has departed entirely from the spheroidal regime and deformed into a flattened disk shape. The majority of the circulation is occurring near the edge of the disk, and the rest of the droplet is relatively quiescent. Figure 5.20b is representative of the higher-field cases; the only differences are that for the higher fields, the disk is flatter and the circulation more localized and pronounced.

Figure 5.21 shows four snapshots of the 10 MV/m leaky dielectric case of Figure 5.20a at different simulation times. Figure 5.21a shows the velocity field after one time step (0.06 radians). Figure 5.21b shows a state halfway through the initial transient, at 1.8 radians, and Figure 5.21c shows the first oscillatory peak. Figure 5.21d shows the steady-state, and is the same as Figure 5.20a.

It may be seen from Figure 5.21a that the early development of the flow field

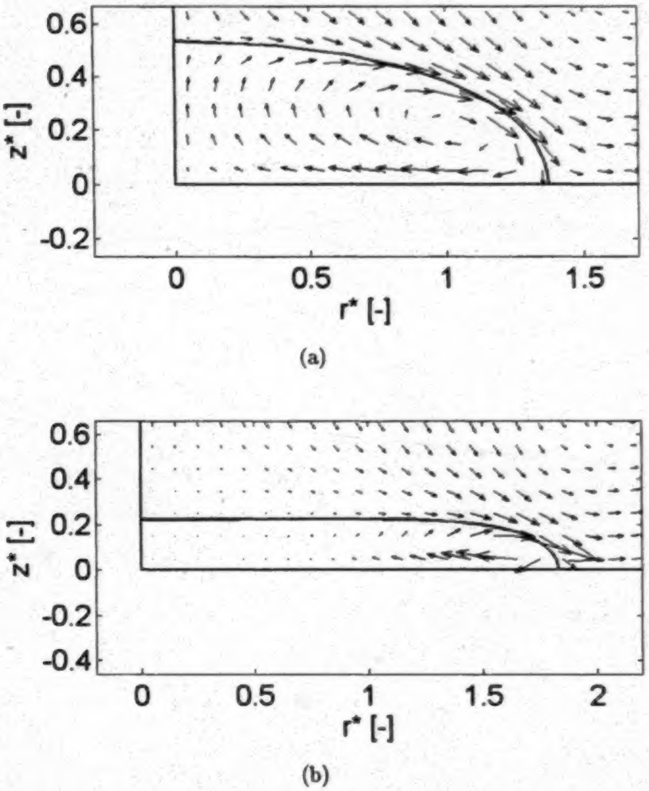

Figure 5.20: Deformed droplet shape and velocity field at end of run for (a) 10 MV/m and (b) 15 MV/m.

is dominated by a tangential flow near the interface. This flow is caused by the presence of interfacial charge, which appears immediately due to the static boundary assumption. Figures 5.21c and 5.21d show that this tangential flow develops into the steady-state circulation predicted by Taylor (1966). Figure 5.21b is plotted with the arrow scale reduced by a factor of 4, due to the fact that the velocity field associated with the transient deformation is much more intense than the steady-state Taylor circulation. It may be seen by comparing Figure 5.21b with 5.21a that for conductivity large enough to justify the static boundary assumption, the tangential

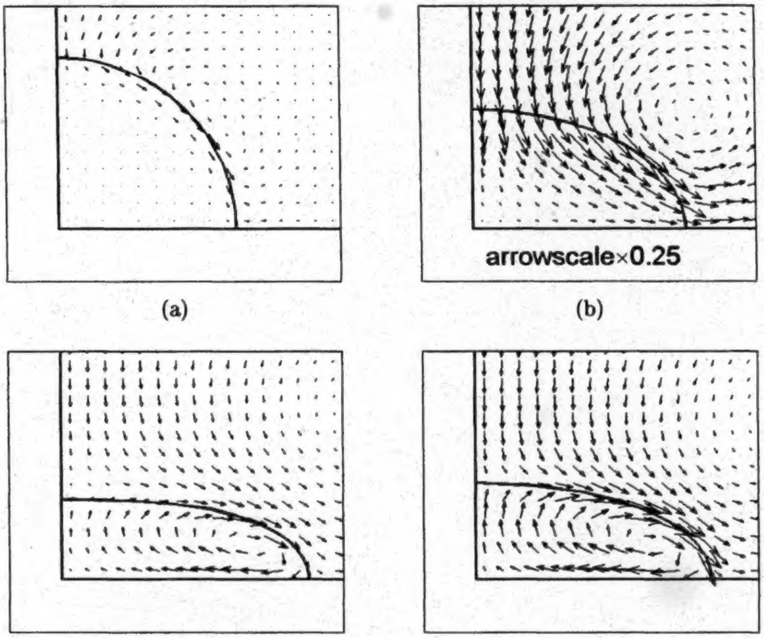

(a) (b)

(c) (d)

Figure 5.21: Stages of deformation for 10 MV/m leaky dielectric case: (a) 0.06 rad, (b) 1.8 rad, (c) 4.5 rad, and (d) 24 rad (steady-state).

flow associated with the steady-state Taylor vortex develops much faster than the main deformation flow. This is consistent with the fact that the main deformation shows no non-minimum-phase effects, despite its sign and magnitude being largely dictated by the pressure gradient set up by Taylor's circulation.

The leaky dielectric results presented in Figures 5.18 - 5.21 are uniformly well-behaved. No tendency toward instability or development of sharp edges is observed. This observation is, however, limited to the specific parameter set studied here. It is not uniformly true of the leaky dielectric model, or even of oblate deformations obtained using it. It depends on the combination of the viscosity, permittivity, and conductivity ratios present in Taylor's discriminatory function. Representative results can be obtained by varying the conductivity ratio, as in Figure 5.22.

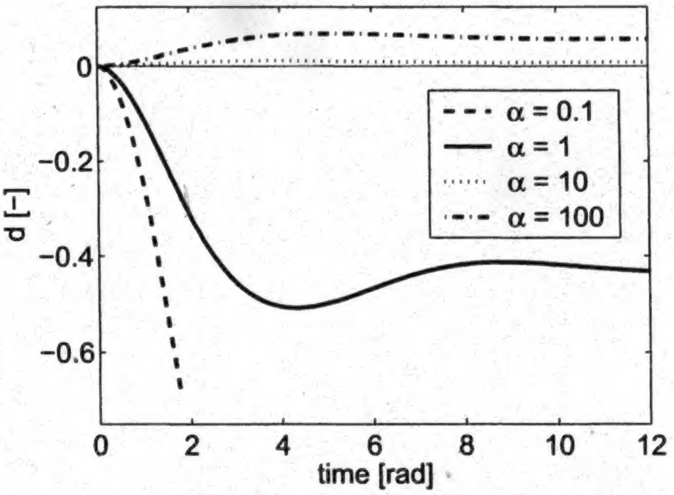

Figure 5.22: Effect of conductivity ratio on the character of the nonlinearity for an applied field of 10 MV/m.

Figure 5.22 shows the effect of altering the conductivity ratio with a consistent applied field of 10 MV/m. The static leaky dielectric model is used. The conductivity ratio here is equal to α, since none of the ion characteristics vary between the two fluids, and values of α between 0.1 and 100 are employed.

The case $\alpha = 0.1$ shows a rapid unbounded response which quickly reaches a singular point, beyond which it is not possible to continue the simulation. The next case, $\alpha = 1$, is identical to the 10 MV/m case in Figure 5.18; it shows moderate deformation with a well-defined steady-state. For $\alpha = 10$, the response is very slightly prolate; it should be noted that this value of the partition coefficient is very close to the value of 8.8882 used to generate the zero-deformation result. In the case where $\alpha = 100$, the deformation is substantially prolate. This case is identical to the one shown in Figure 5.14a, and has a slightly higher deformation than that predicted by the linear theory.

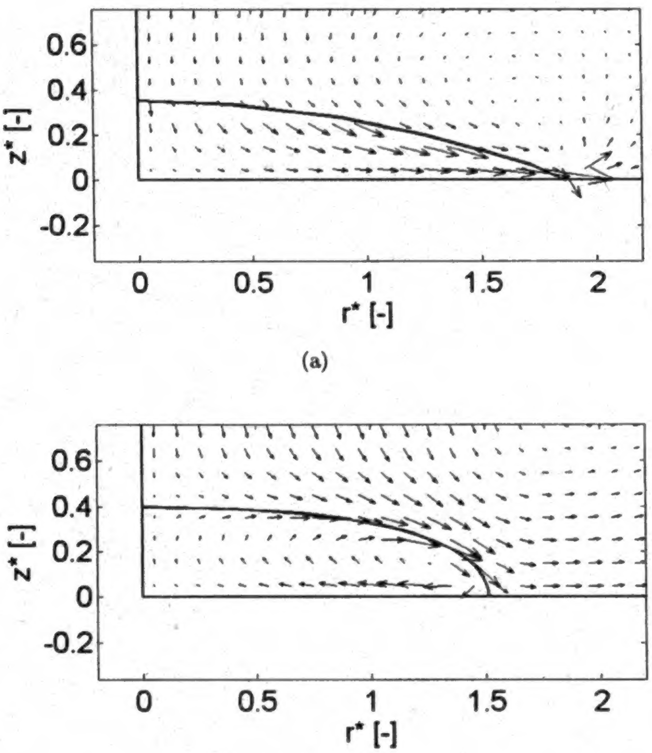

(a)

(b)

Figure 5.23: Deformed droplet shape and velocity field at end of run, for (a) $\alpha = 0.1$ and 10 MV/m and (b) $\alpha = 3$ and 30 MV/m.

This case illustrates the alteration that the conductivity ratio can produce in the character of the deformation. The difference between the cases $\alpha = 0.1$ and 1 is particularly striking. Despite the fact that they are both oblate deformations under the same applied field, the $\alpha = 0.1$ case develops a singularity so fast that the simulation is ended before the deformation reaches values as high as the more extreme cases in Figure 5.18. The deformation parameter at the singularity in this case is -0.723, which denotes a substantially thicker drop than the value of -0.898 reached by the (stable) 20 MV/m case from Figure 5.18.

Figure 5.23 shows the difference in deformed shape between the $\alpha = 0.1$ case from Figure 5.22 and a new case with $\alpha = 3$. The $\alpha = 3$ case uses an applied electric field of 30 MV/m, because at this partition coefficient it is relatively insensitive to electrical actuation. The static leaky dielectric model is used for both cases. The $\alpha = 3$ case in Figure 5.23b represents steady-state, but the $\alpha = 0.1$ case in Figure 5.23a represents the point at which the boundary becomes singular, as this case has no steady state.

The difference in character of the deformation induced by the change in partition coefficient, and hence conductivity ratio, is clear in these figures. The lower ratio of 0.1 causes the drop, under high electric field, to develop a sharp edge around its equator, which constitutes an analogue to the tip streaming mode of breakup. A higher ratio of 3 results in a less extreme shape having no singularities, and a much larger applied field is necessary to produce it.

Figure 5.24 shows deformed shapes for α values of 0.2 and 0.5. The applied field is 10 MV/m, and the static leaky dielectric model is used.

These two cases are much closer to the crossover point between the sharp-edged and blunt-disk modes of deformation. Figure 5.24a shows a third type of behaviour that appears near the transition, in which a toroidal segment pinches off from the main drop. Figure 5.24b shows a case with a larger partition coefficient of 0.5, and it shows most of the characteristics of the blunt disk droplets. A vestige of the toroidal ring can nevertheless be seen in the widening of this droplet toward its edge.

Transitions between these modes of deformation are here facilitated by changing only a single parameter, the partition coefficient. It is not unlikely that the observed effect is actually part of a compound effect involving the fluid parameters, as well as the permittivity ratio, which is known to affect the character of perfect dielectric deformations [Rosenkilde, 1969, Miksis, 1981, Sherwood, 1988].

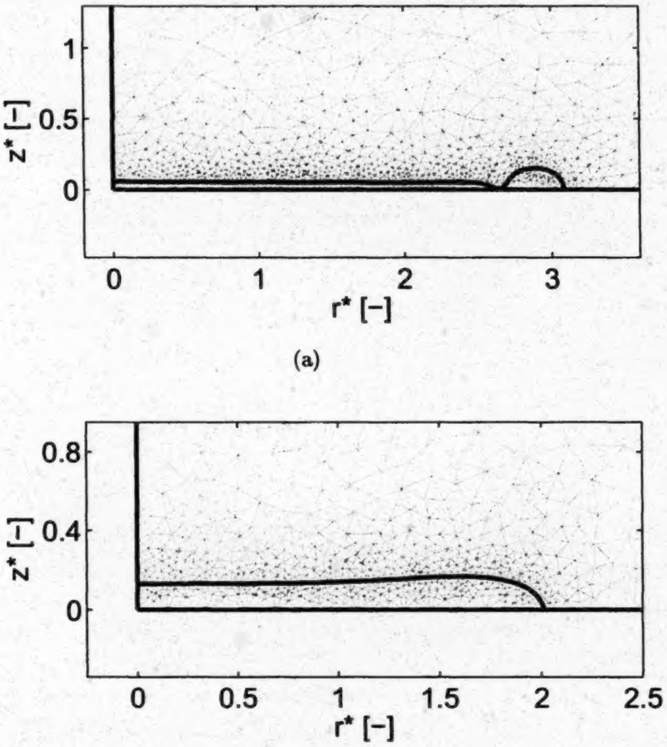

(a)

(b)

Figure 5.24: Deformed droplet shapes for (a) $\alpha = 0.2$ and (b) $\alpha = 0.5$, with an applied field of 10 MV/m, showing the transition between two modes of nonlinear deformation.

5.3 Lumped Parameter Modeling of Dynamic Responses

One of the objectives of this work is to move toward an understanding of the dynamics of drop actuation by electrowetting, in order to develop methods of dynamically controlling such actuation systems. Finite element modeling cannot be used in real-time control software, due to its computationally intensive nature. It is therefore desirable to be able to generate accurate approximations to the numerical results using a simplified model framework with only a few parameters. Such a lumped

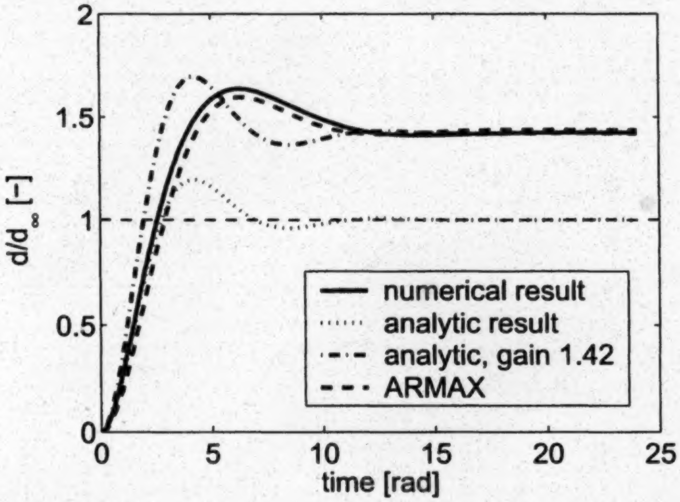

Figure 5.25: Comparison of the numerical results with analytic predictions and with the ARMAX-derived lumped parameter model, for the perfect dielectric base case with 15 MV/m applied field.

parameter model would be amenable to solution within the computational resources of embedded control hardware.

In order to fit a lumped parameter dynamic model to the numerical results, an AutoRegressive Moving Average, Extra Input (ARMAX) technique is employed. This technique allows least-squares fitting of a parametric dynamic model of arbitrary order to an input response; in this case, the finite element results. For the stable perfect dielectric deformations studied here, a second-order linear model was found to display adequate accuracy characteristics.

Figure 5.25 shows a plot of the perfect dielectric dynamic response with base case parameters and an applied field of 15 MV/m, compared with the ARMAX parametric model response. The analytically predicted dynamic response from Equation 4.7 is included for comparison, as well as a modification of the analytic prediction in which a static gain of 1.42 has been applied to the transfer function in order to match the numerically obtained steady-state. The dashed line denotes the analytic Taylor result.

The analytic prediction in its unadjusted state is clearly inadequate. It predicts the initial rise correctly, but it breaks off too soon, following the analytic steady state. Correcting it with static gain in order to match the steady-state value of the numerical result provides the correct steady state, but the transient is too fast. The second-order ARMAX model does not precisely track the numerical result, but it is far superior to the analytic prediction, giving essentially correct rise and damping times.

It is clear from Figure 5.25 that in cases of large deformation, the lumped parameter model offers substantially better prediction of the drop dynamics than the analytic model. Such a model could be used as a predictor in an embedded control scheme. Given a set of simulations at different applied fields, an ARMAX model could be used to linearize at each applied field, and interpolation on a lookup table could be used to track the nonlinearity at high deformations. Both the model order and parameters could be determined for each applied field, since the ARMAX method is not limited to second-order models.

5.4 Summary

The numerical method developed here is capable of simulating droplet deformation over a wide range of physical parameters, extending to large deformations and the effects of finite electric time scales. Numerical results for smaller deformations are in accord with expectations based on existing analytic results, and for larger deformations, several nonlinear phenomena have been simulated which are observed in experiments but cannot be predicted by analytic theory. The dynamic evolution of such phenomena is also tracked by the simulation results. In the framework of the leaky dielectric model, the effects of migration, convection and interface dilation on the interfacial charge buildup can also be modeled, yielding differences from early analytic results even for small deformations. Due to the interface description employed in this method, it is impossible to continue a solution past a boundary singularity or pinchoff event, which places a limit on large-deformation simulations in which such events occur.

CHAPTER 6

CONCLUSIONS AND FURTHER RESEARCH

6.1 Development of the Numerical Technique

A numerical scheme based on the finite element method has been developed for transient simulation of drop deformation in an electric field. The method is capable of simulating perfect dielectric fluids or fluids with finite conductivity, so long as any conductive charge buildup occurs in a layer much smaller than the drop radius. The time dependence of electrical conduction can also be taken into account, along with finite charge convection effects on the drop interface. Large deformations can be simulated, but due to the use of a moving mesh method the drop must remain contiguous, which prohibits the simulation of breakup modes past their initiating singularities. The method has been demonstrated to produce solutions of equivalent accuracy to the methods of other researchers in cases of relatively high Reynolds number oscillations.

6.2 Observed Results

6.2.1 Perfect Dielectric Results

In low-deformation cases, the perfect dielectric results accord well with theory. For larger deformations, the observed mode of instability replicates a well-known phenomenon; that of tip streaming. The numerical method prohibits actual ejection of satellite drops, but the formation of the well-known pointed tip for high applied field and permittivity ratio is observed.

An apparent increase in damping for high-field dynamic responses with defined steady-states is noted. It is speculated that this may be due to nonuniform electrical stress during the transient.

6.2.2 Leaky Dielectrics: Boundary Charge Dynamics

The buildup of charge due to conduction is compared with analytic theory and found to be in good agreement. Steady-state effects on the deformation due to charge convection accord well with the calculations of other researchers. The transient effect of finite-in-time charge buildup is noted to result in non-minimum-phase dynamic responses when the steady-state deformation is oblate.

6.2.3 Leaky Dielectrics: Large Deformations

Three classes of large oblate deformation are noted, in addition to prolate modes, which are selectable through choice of fluid electrical parameters. The first is a stable, round-edged disk that flattens but does not burst under the symmetry assumptions made here. The second is a sharp-edged disk shape which is unstable due to the rapid development of the equatorial singularity. The third is a transitional mode, also unstable, in which the edge of the disk pinches off into a torus. This mode, like the extreme cases of the flat disk mode, is expected to behave differently in a fully three-dimensional setting where the axial and equatorial symmetry assumptions are relaxed.

6.2.4 Lumped Parameter Modeling

Finite element calculations are prohibitively computationally intensive for real-time control systems. A dynamic controller for electrowetting actuation on a lab-on-a-chip would require a low-complexity lumped parameter model which could be used in real time. A best-fit dynamic model utilizing only two parameters is demonstrated here for the suspended drop system, and exhibits much lower error than the analytic model in large-deformation cases.

6.3 Recommendations for Future Work

Due to the time spent developing the code, the parameter space was not as thoroughly explored as might be desirable. In addition, a dimensional analysis of the results to isolate relevant parameters has not been performed. Such an analysis might also assist in the design of a less user-dependent timestep selection scheme.

In the course of development, the Navier-Stokes/Poisson-Nernst-Planck system necessary to describe the full electrokinetic problem was solved for certain conditions on stationary geometries. However, a proper moving-mesh implementation of the full electrokinetic model capable of predicting the correct deformation for intermediate double layer thicknesses has not yet been developed. It is recommended that if this is attempted, the Nernst-Planck equations be considered in equilibrium as a first attempt, since the time scale for the full transient problem is very long compared with the drop oscillation.

The numerical technique outlined in this dissertation was implemented using MATLAB scripting in the framework of FEMLAB 2.3b. FEMLAB 3.x no longer supports the necessary low-level programming and data access necessary to implement the method, and FEMLAB 2.3b is incompatible with the latest version of MATLAB. In short, the code is in danger of becoming obsolete. An attempt to implement a finite element method with equivalent capabilities on a safer platform might be advisable, if it involves substantially less effort than the original development.

Once the two-phase suspended droplet problem is sufficiently well understood, options should be explored regarding the modeling of the electrowetting effect. The aim of such research should be to understand the fundamental physics underlying the electrowetting phenomenon. Ideally, a fully three-dimensional model incorporating correct physics for all aspects of the electrowetting problem should become possible once the requisite physical understanding and numerical resources are acquired.

BIBLIOGRAPHY

[Ajayi, 1978] Ajayi, O. O. (1978). A note on taylor's electrohydrodynamic theory. *Proc. Roy. Soc. Lond. A-Math. Phys. Sci.*, 364(1719):499–507.

[Allan and Mason, 1962] Allan, R. S. and Mason, S. G. (1962). Particle behaviour in shear and electric fields .1. deformation and burst of fluid drops. *Proc. Roy. Soc. Lond. A-Math. Phys. Sci.*, 267(1328):45–61.

[Azuma and Yoshihara, 1999] Azuma, H. and Yoshihara, S. (1999). Three-dimensional large-amplitude drop oscillations: experiments and theoretical analysis. *J. Fluid Mech.*, 393:309–332.

[Basaran, 1992] Basaran, O. A. (1992). Nonlinear oscillations of viscous liquid drops. *J. Fluid Mech.*, 241:169–198.

[Basaran et al., 1995] Basaran, O. A., Patzek, T. W., Benner, R. E., and Scriven, L. E. (1995). Nonlinear oscillations and breakup of conducting, inviscid drops in an externally applied electric field. *Ind. Eng. Chem. Res.*, 34(10):3454–3465.

[Basaran and Scriven, 1989] Basaran, O. A. and Scriven, L. E. (1989). Axisymmetric shapes and stability of charged drops in an external electric field. *Phys. Fluids A*, 1(5):799–809.

[Batchelor, 1967] Batchelor, G. K. (1967). *An Introduction to Fluid Mechanics*. Cambridge University Press.

[Baygents and Saville, 1989] Baygents, J. C. and Saville, D. A. (1989). The circulation produced in a drop by an electric field: a high field strength electrokinetic model. In Wang, T. G., editor, *Drops and Bubbles: Third Intl. Colloq.*, pages 7–17. American Institute of Physics.

[Bentenitis and Krause, 2005] Bentenitis, N. and Krause, S. (2005). Droplet deformation in dc electric fields: the extended leaky dielectric model. *Langmuir*, 21:6194–6209.

[Bhattacharjee, 1995] Bhattacharjee, S. (1995). *Role of surface interactions in prediction of flux decline during ultrafiltration*. PhD thesis, Indian Institute of Technology (Kanpur).

[Brazier-Smith, 1971] Brazier-Smith, P. R. (1971). Stability and shape of isolated and pairs of water drops in an electric field. *Phys. Fluids*, 14(1):1–6.

[Brazier-Smith et al., 1971] Brazier-Smith, P. R., Jennings, S. G., and Latham, J. (1971). An investigation of the behaviour of drops and drop-pairs subjected to strong electrical forces. *Proc. Roy. Soc. Lond. A-Math. Phys. Sci.*, 325(1562):363–376.

[Brown et al., 1994] Brown, P. N., Hindmarsh, A. C., and Petzold, L. R. (1994). Using krylov methods in the solution of large-scale differential-algebraic systems. *SIAM J. Sci. Comput.*, 15:1467–1488.

[Brown et al., 1998] Brown, P. N., Hindmarsh, A. C., and Petzold, L. R. (1998). Consistent initial condition calculation for differential-algebraic systems. *SIAM J. Sci. Comput.*, 19:1495–1512.

[Cho et al., 2003] Cho, S. K., Moon, H. J., and Kim, C. J. (2003). Creating, transporting, cutting, and merging liquid droplets by electrowetting-based actuation for digital microfluidic circuits. *J. Microelectromech. Syst.*, 12(1):70–80.

[COMSOL, 2002] COMSOL (2002). *FEMLAB Reference Manual*. COMSOL AB. Version 2.3.

[CRC, 2004] CRC (2004). *CRC Handbook of Chemistry and Physics*. CRC Press, 85th edition.

[Eow et al., 2001] Eow, J. S., Ghadiri, M., and Sharif, A. (2001). Deformation and break-up of aqueous drops in dielectric liquids in high electric fields. *Journal of Electrostatics*, 51-52:463–469.

[Feng, 1999] Feng, J. Q. (1999). Electrohydrodynamic behaviour of a drop subjected to a steady uniform electric field at finite electric reynolds number. *Proc. Roy. Soc. Lond. A-Math. Phys. Eng. Sci.*, 455(1986):2245–2269.

[Feng, 2002] Feng, J. Q. (2002). A 2d electrohydrodynamic model for electrorotation of fluid drops. *J. Coll. Interf. Sci.*, 246:112–121.

[Feng and Beard, 1990] Feng, J. Q. and Beard, K. V. (1990). Small-amplitude oscillations of electrostatically levitated drops. *Proc. Roy. Soc. Lond. A-Math. Phys. Sci.*, 430(1878):133–150.

[Feng and Beard, 1991a] Feng, J. Q. and Beard, K. V. (1991a). 3-dimensional oscillation characteristics of electrostatically deformed drops. *Proc. Roy. Soc. Lond. A-Math. Phys. Sci.*, 227:429–447.

[Feng and Beard, 1991b] Feng, J. Q. and Beard, K. V. (1991b). Resonances of a conducting drop in an alternating electric field. *J. Fluid Mech.*, 222:417–435.

[Feng and Scott, 1996] Feng, J. Q. and Scott, T. C. (1996). A computational analysis of electrohydrodynamics of a leaky dielectric drop in an electric field. *J. Fluid Mech.*, 311:289–326.

[Franklin et al., 2002] Franklin, G. F., Powell, J. D., and Emami-Naeini, A. (2002). *Feedback Control of Dynamic Systems.* Prentice-Hall, 4th edition.

[Garton and Krasucki, 1964] Garton, C. G. and Krasucki, Z. (1964). Bubbles in insulating liquids: stability in an electric field. *Proc. Roy. Soc. Lond. A-Math. Phys. Sci.*, 280(1381):211–226.

[Ha and Yang, 1995] Ha, J. W. and Yang, S. M. (1995). Effects of surfactant on the deformation and stability of a drop in a viscous-fluid in an electric-field. *J. Colloid Interf. Sci.*, 175(2):369–385.

[Ha and Yang, 1998] Ha, J. W. and Yang, S. M. (1998). Effect of nonionic surfactant on the deformation and breakup of a drop in an electric field. *J. Colloid Interf. Sci.*, 206:195–204.

[Haywood et al., 1991] Haywood, R. J., Renksizbulut, M., and Raithby, G. D. (1991). Transient deformation of freely-suspended liquid droplets in electrostatic fields. *AICHE Journal*, 37(9):1305–1317.

[Hirata et al., 2000] Hirata, T., Kikuchi, T., Tsukada, T., and Hozawa, M. (2000). Finite element analysis of electrohydrodynamic time-dependent deformation of dielectric drop under uniform dc electric field. *J. Chem. Eng. Jpn.*, 33(1):160–167.

[Landau and Lifshitz, 1960] Landau, L. D. and Lifshitz, E. M. (1960). *Electrodynamics of continuous media.* Pergamon Press.

[Lev et al., 2001] Lev, B. I., Nazarenko, V. G., Nych, A. B., Schur, D., Tomchuk, P. M., Yamamoto, J., and Yokoyama, H. (2001). Deformation of liquid crystal droplets under the action of an external ac electric field. *Phys. Rev. E*, 64(021706):1–5.

[Lu, 2002] Lu, Y. (2002). Electrohydrodynamic deformation of water drops in oil with an electric field. Master's thesis, University of Alberta (Canada).

[Masliyah, 1994] Masliyah, J. H. (1994). *Electrokinetic transport phenomena*. AOSTRA Technical Publication Series # 12. AOSTRA.

[Melcher and Taylor, 1969] Melcher, J. R. and Taylor, G. I. (1969). Electrohydrodynamics: a review of the role of interfacial shear stresses. *Annu. Rev. Fluid Mech.*, 1:111–146.

[Miksis, 1981] Miksis, M. J. (1981). Shape of a drop in an electric field. *Phys. Fluids*, 24(11):1967–1972.

[Miller and Scriven, 1968] Miller, C. A. and Scriven, L. E. (1968). The oscillations of a fluid droplet immersed in another fluid. *J. Fluid Mech.*, 32:417–435.

[O'Konski and Harris, 1957] O'Konski, C. T. and Harris, F. E. (1957). Electric free energy and the deformation of droplets in electrically conducting systems. *J. Phys. Chem.*, 61:1172–1174.

[O'Konski and Thacher, 1953] O'Konski, C. T. and Thacher, H. C. (1953). The distortion of aerosol droplets by an electric field. *J. Phys. Chem.*, 57:955–958.

[Rosenkilde, 1969] Rosenkilde, C. E. (1969). A dielectric fluid drop in an electric field. *Proc. Roy. Soc. Lond. A-Math. Phys. Sci.*, 312(1511):473–494.

[Saville, 1997] Saville, D. A. (1997). Electrohydrodynamics: the taylor-melcher leaky dielectric model. *Annu. Rev. Fluid Mech.*, 29:27–64.

[Scott et al., 1990] Scott, T. C., Basaran, O. A., and Byers, C. H. (1990). Characteristics of electric-field-induced oscillations of translating liquid droplets. *Ind. Eng. Chem. Res.*, 29(5):901–909.

[Shapiro et al., 2003] Shapiro, B., Moon, H., Garrell, R. L., and Kim, C. J. (2003). Equilibrium behavior of sessile drops under surface tension, applied external fields, and material variations. *J. Appl. Phys.*, 93(9):5794–5811.

[Sherwood, 1988] Sherwood, J. D. (1988). Breakup of fluid droplets in electric and magnetic-fields. *J. Fluid Mech.*, 188:133–146.

[Smythe, 1968] Smythe, W. R. (1968). *Static and Dynamic Electricity.* McGraw - Hill, 3rd edition.

[Sozou, 1972] Sozou, C. (1972). Electrohydrodynamics of a liquid drop: the time-dependent problem. *Proc. Roy. Soc. Lond. A-Math. Phys. Sci.*, 331(1585):263–272.

[Sozou, 1973] Sozou, C. (1973). Electrohydrodynamics of a liquid drop: the development of the flow field. *Proc. Roy. Soc. Lond. A-Math. Phys. Sci.*, 334(1598):343–356.

[Taylor, 1934] Taylor, G. I. (1934). The formation of emulsions in definable fields of flow. *Proc. Roy. Soc. Lond. A*, 146(858):501–523.

[Taylor, 1964] Taylor, G. I. (1964). Disintegration of water drops in an electric field. *Proc. Roy. Soc. Lond. A-Math. Phys. Sci.*, 280(1382):383–397.

[Taylor, 1966] Taylor, G. I. (1966). Studies in electrohydrodynamics. i. circulation produced in a drop by an electric field. *Proc. Roy. Soc. Lond. A-Math. Phys. Sci.*, 291(1425):159–166.

[Torza et al., 1971] Torza, S., Cox, R. G., and Mason, S. G. (1971). Electrohydrodynamic deformation and burst of liquid drops. *Phil. Trans. Roy. Soc. Lond. A-Math. Phys. Sci.*, 269(1198):295–319.

[Tsukada et al., 1993] Tsukada, T., Katayama, T., Ito, Y., and Hozawa, M. (1993). Theoretical and experimental studies of circulation inside and outside a deformed drop under a uniform electric field. *J. Chem. Eng. Japan*, 26:698–703.

[Vizika and Saville, 1992] Vizika, O. and Saville, D. A. (1992). The electrohydrodynamic deformation of drops suspended in liquids in steady and oscillatory electric-fields. *J. Fluid Mech.*, 239:1–21.

[Whitaker et al., 1998] Whitaker, D. L., Kim, C., Vicente, C. L., Weilert, M. A., Maris, H. J., and Seidel, G. M. (1998). Shape oscillations in levitated he ii drops. *J. Low Temp. Phys.*, 113:491–499.

[Zhang and Kwok, 2005] Zhang, J. and Kwok, D. Y. (2005). A 2d lattice boltzmann study on electrohydrodynamic drop deformation with the leaky dielectric theory. *J. Comp. Phys.*, 206:150–161.

[Zholkovskij et al., 2002] Zholkovskij, E. K., Masliyah, J. H., and Czarnecki, J. (2002). An electrokinetic model of drop deformation in an electric field. *J. Fluid Mech.*, 472:1–27.

APPENDIX A

ANNOTATED MODEL SCRIPTS

The numerical model described in this dissertation was implemented utilizing the FEMLAB/MATLAB interface, via M-file scripting. Here follows a series of annotated excerpts detailing various key sections of the algorithm.

A.1 Dynamic Interfacial Charge Calculation

```
%%%%%%%%%%%%%%%%%%%%%%%%%%%%%%%%%%%%%%%%%%%%%%%%%%%%%%%%%%%%%%%%%%%%%%%%%%%%%%
% The dynamic behaviour of the interfacial free charge distribution is modeled
% with a first-order integration method in time, using the same time stepping
% scheme as the bulk solution.  At each time step, this code block is executed
% to update the values in the nodewise list of interfacial charge densities from
% the previous time step.  Conduction, convection and dilation are treated as in
% Saville (1997).
%%%%%%%%%%%%%%%%%%%%%%%%%%%%%%%%%%%%%%%%%%%%%%%%%%%%%%%%%%%%%%%%%%%%%%%%%%%%%%

%%%%%%%%%%%%%%%%%%%%%%%%%%%%%%%%%%%%%%%%%%%%%%%%%%%%%%%%%%%%%%%%%%%%%%%%%%%%%%
% A list of distances between adjacent boundary nodes will be required for
% differentiation purposes.  This list is one entry shorter than ‘S2’, the
% nodewise curve parameter list for the interface as established by the
% curvature calculator.  The curve parameter in S2 goes from 0 at the pole of
% the drop (on the z-axis) to 1 at the equator (the r-axis).  ‘lscale’ is the
% radius of the drop.  This result is fully dimensional.
%%%%%%%%%%%%%%%%%%%%%%%%%%%%%%%%%%%%%%%%%%%%%%%%%%%%%%%%%%%%%%%%%%%%%%%%%%%%%%
clear seglength;
for i = 1:length(S2)-1;
    seglength(i) = lscale*sqrt((r(i+1)-r(i))^2+(z(i+1)-z(i))^2);
end

%%%%%%%%%%%%%%%%%%%%%%%%%%%%%%%%%%%%%%%%%%%%%%%%%%%%%%%%%%%%%%%%%%%%%%%%%%%%%%
% If this is the first time step (‘t’ is zero), or if Taylor’s static boundary
% condition is being used (‘static’ is not zero), or if both fluids are perfect
% dielectrics (the far-field ionic concentration ‘c0’ is zero), all entries in
% the nodewise list of interfacial free charge densities are zero.
%%%%%%%%%%%%%%%%%%%%%%%%%%%%%%%%%%%%%%%%%%%%%%%%%%%%%%%%%%%%%%%%%%%%%%%%%%%%%%%%
if t == 0;
    charge = zeros(size(S2));
elseif static ~= 0;
    charge = zeros(size(S2));
elseif c0 == 0;
    charge = zeros(size(S2));

%%%%%%%%%%%%%%%%%%%%%%%%%%%%%%%%%%%%%%%%%%%%%%%%%%%%%%%%%%%%%%%%%%%%%%%%%%%%%%%%
% If none of the above is true, the charge distribution is updated based on the
% solution from the previous time step.
%%%%%%%%%%%%%%%%%%%%%%%%%%%%%%%%%%%%%%%%%%%%%%%%%%%%%%%%%%%%%%%%%%%%%%%%%%%%%%%%
else

    %%%%%%%%%%%%%%%%%%%%%%%%%%%%%%%%%%%%%%%%%%%%%%%%%%%%%%%%%%%%%%%%%%%%%%%%%%%%%
    % Since convection will be included later, the convective effect of moving
    % the mesh is removed by interpolating the old solution in position to the
    % new nodes.  This method requires the curve parameter to NOT move with the
    % nodes; this is desirable for other reasons as well, and is guaranteed by
    % the curve parameter correction function ‘chord.m’.  The variables ‘nE_i’
    % and ‘nE_e’ are nodewise lists of the normal components of the electric
    % field from the internal and external fluids respectively.
    %%%%%%%%%%%%%%%%%%%%%%%%%%%%%%%%%%%%%%%%%%%%%%%%%%%%%%%%%%%%%%%%%%%%%%%%%%%%%
    charge = interp1(S2_old,charge,S2);
    nE_i = interp1(S2_old,nE_i,S2);
    nE_e = interp1(S2_old,nE_e,S2);

    %%%%%%%%%%%%%%%%%%%%%%%%%%%%%%%%%%%%%%%%%%%%%%%%%%%%%%%%%%%%%%%%%%%%%%%%%%%%%
    % The convective change in charge density is integrated over the time step.
    % The nondimensional time step is given by ‘tstep’, and the dimensional
    % characteristic time is ‘time’.  This result is fully dimensional.
    %%%%%%%%%%%%%%%%%%%%%%%%%%%%%%%%%%%%%%%%%%%%%%%%%%%%%%%%%%%%%%%%%%%%%%%%%%%%%
    conductive = time*tstep.*(sigma_i.*nE_i-sigma_e.*nE_e);

    %%%%%%%%%%%%%%%%%%%%%%%%%%%%%%%%%%%%%%%%%%%%%%%%%%%%%%%%%%%%%%%%%%%%%%%%%%%%%
    % The time average of the velocity on the interface over the previous time
    % step is required. Nodewise lists of r and z velocity components are
    % generated using FEMLAB’s postprocessing interpolator, ‘postinterp’, acting
    % on the unconvected saved copy of the FEMLAB data structure, ‘fem00’.
    %  Quadratic time averaging is used: given three equally spaced points, the
    % average value of a parabolic fit through these points is 2/3 of the value
    % at the centre point plus 1/6 of the value at each end point.  The
    % dimensional characteristic velocity is ‘velocity’.  These results are
    % fully dimensional.
    %%%%%%%%%%%%%%%%%%%%%%%%%%%%%%%%%%%%%%%%%%%%%%%%%%%%%%%%%%%%%%%%%%%%%%%%%%%%%
    u_bnd = velocity.*(postinterp(fem00,'u',S2,'dom',7,'solnum',1)./6+...
        postinterp(fem00,'u',S2,'dom',7,'solnum',2).*(2/3)+...
        postinterp(fem00,'u',S2,'dom',7,'solnum',3)./6);
    v_bnd = velocity.*(postinterp(fem00,'v',S2,'dom',7,'solnum',1)./6+...
        postinterp(fem00,'v',S2,'dom',7,'solnum',2).*(2/3)+...
        postinterp(fem00,'v',S2,'dom',7,'solnum',3)./6);
```

```
%%%%%%%%%%%%%%%%%%%%%%%%%%%%%%%%%%%%%%%%%%%%%%%%%%%%%%%%%%%%%%%%%%%%%%%%%%%%%%%%
% The gradient of the charge density along the interface is calculated based
% on the charge distribution from the previous time step.  For the first
% point (the pole of the drop), it is zero.  For subsequent points, a
% second-order polynomial fit is used based on the point of interest and its
% immediate neighbours.  The last point (the equator of the drop) re-uses
% the polynomial fit from the previous point, which is a valid procedure
% given that equatorial symmetry is assumed.  The polynomial fit is
% nondimensionalized in order to avoid ill-conditioning.  The permittivity
% of free space is 'epsilon0', the applied field is 'field', and the drop
% radius is 'lscale'.  The calculated derivative 'dq', which is the
% derivative of free charge density as a function of distance along the
% boundary from pole to equator, is fully dimensional.
%%%%%%%%%%%%%%%%%%%%%%%%%%%%%%%%%%%%%%%%%%%%%%%%%%%%%%%%%%%%%%%%%%%%%%%%%%%%%%%%
dq = zeros(1,length(S2));
for i = 2:length(S2)-1;
    quadcharge = polyfit([-seglength(i-1) 0 seglength(i)]./lscale, ...
        [charge(i-1) charge(i) charge(i+1)]./(epsilon0*field),2);
    dq(i) = epsilon0*field*quadcharge(2)/lscale;
end
dq(end) = epsilon0*field*polyval([2*quadcharge(1) quadcharge(2)],...
        seglength(end)/lscale)/lscale;

%%%%%%%%%%%%%%%%%%%%%%%%%%%%%%%%%%%%%%%%%%%%%%%%%%%%%%%%%%%%%%%%%%%%%%%%%%%%%%%%
% The convective change in charge density over the time step is calculated
% using the boundary velocities and interfacial charge gradient.  The
% tangential component of the interfacial velocity at each point is
% calculated using the normal vector obtained by the curvature calculator,
% consisting of r and z components 'n_r' and 'n_z'.  The tangential vector
% has r and z components 'n_z' and '-n_r', respectively.  This result is
% fully dimensional.
%%%%%%%%%%%%%%%%%%%%%%%%%%%%%%%%%%%%%%%%%%%%%%%%%%%%%%%%%%%%%%%%%%%%%%%%%%%%%%%%
convective = -time*tstep.*(n_z.*u_bnd-n_r.*v_bnd).*dq;

%%%%%%%%%%%%%%%%%%%%%%%%%%%%%%%%%%%%%%%%%%%%%%%%%%%%%%%%%%%%%%%%%%%%%%%%%%%%%%%%
% The average spatial derivatives of the interfacial velocity over the
% previous time step are obtained in a manner similar to the velocity above.
%  Quadratic time averaging is used.  These results are fully dimensional.
%%%%%%%%%%%%%%%%%%%%%%%%%%%%%%%%%%%%%%%%%%%%%%%%%%%%%%%%%%%%%%%%%%%%%%%%%%%%%%%%
ur_bnd = velocity.*(postinterp(fem00,'ur',S2,'dom',7,'solnum',1)./6+...
    postinterp(fem00,'ur',S2,'dom',7,'solnum',2).*(2/3)+...
    postinterp(fem00,'ur',S2,'dom',7,'solnum',3)./6)./lscale;
vr_bnd = velocity.*(postinterp(fem00,'vr',S2,'dom',7,'solnum',1)./6+...
    postinterp(fem00,'vr',S2,'dom',7,'solnum',2).*(2/3)+...
    postinterp(fem00,'vr',S2,'dom',7,'solnum',3)./6)./lscale;
uz_bnd = velocity.*(postinterp(fem00,'uz',S2,'dom',7,'solnum',1)./6+...
    postinterp(fem00,'uz',S2,'dom',7,'solnum',2).*(2/3)+...
    postinterp(fem00,'uz',S2,'dom',7,'solnum',3)./6)./lscale;
vz_bnd = velocity.*(postinterp(fem00,'vz',S2,'dom',7,'solnum',1)./6+...
    postinterp(fem00,'vz',S2,'dom',7,'solnum',2).*(2/3)+...
    postinterp(fem00,'vz',S2,'dom',7,'solnum',3)./6)./lscale;
    %%%%%%%%%%%%%%%%%%%%%%%%%%%%%%%%%%%%%%%%%%%%%%%%%%%%%%%%%%%%%%%%%%%%%%%%%%%%
    % The contribution of interface dilation to the change in free charge
    % density is calculated from the average velocity gradient over the previous
    % time step.  This result is fully dimensional.
    %%%%%%%%%%%%%%%%%%%%%%%%%%%%%%%%%%%%%%%%%%%%%%%%%%%%%%%%%%%%%%%%%%%%%%%%%%%%
    dilative = time*tstep.*charge.*...
        (ur_bnd.*n_r.^2+(uz_bnd+vr_bnd).*n_r.*n_z+vz_bnd.*n_z.^2);

    %%%%%%%%%%%%%%%%%%%%%%%%%%%%%%%%%%%%%%%%%%%%%%%%%%%%%%%%%%%%%%%%%%%%%%%%%%%%
    % The conductive, convective, and dilative components of the change in
    % interfacial free charge density are added to the free charge density from
    % the previous step to produce an updated nodewise list.  This result is
    % fully dimensional.
    %%%%%%%%%%%%%%%%%%%%%%%%%%%%%%%%%%%%%%%%%%%%%%%%%%%%%%%%%%%%%%%%%%%%%%%%%%%%
    charge = charge+conductive+convective+dilative;
end

%%%%%%%%%%%%%%%%%%%%%%%%%%%%%%%%%%%%%%%%%%%%%%%%%%%%%%%%%%%%%%%%%%%%%%%%%%%%%%%%
% In order to allow use of the calculated free charge density in the finite
% element solution, it is nondimensionalized appropriately.
%%%%%%%%%%%%%%%%%%%%%%%%%%%%%%%%%%%%%%%%%%%%%%%%%%%%%%%%%%%%%%%%%%%%%%%%%%%%%%%%
charge_nd = charge./(epsilon0*field);
```

A.2 Interfacial Curvature Calculation

```
%%%%%%%%%%%%%%%%%%%%%%%%%%%%%%%%%%%%%%%%%%%%%%%%%%%%%%%%%%%%%%%%%%%%%%%%%%%%%%%%
% This code is responsible for extracting the interface nodes from the mesh and
% generating a high-quality normal vector and mean curvature at each point.
% First, a list of curve parameters corresponding to the node positions along
% the interfacial boundary is extracted.  Then the geometric coordinates of
% these points are found by using the FEMLAB function 'postinterp' on the
% boundary.  At each end of the list, two additional nodes are added; these are
% mirrors of the second and third nodes away from each end, and are incorporated
% to allow a symmetric polynomial fit on all real nodes.
%
% The polynomial fitting process takes place on a rotated coordinate system.
% Two fits are done, the first to obtain the local normal at each point and the
% second to find the curvature.  Both fits are fourth-order, using two points on
% either side of the node in question as well as the node itself, for a total of
% five points.  The horizontal axis used during the first fit passes through the
% endpoints of the fit.  For the second fit, the coordinate system is rotated
% again so as to align the vertical axis with the newly-calculated normal
% vector.  This allows calculation of the in-plane curvature by differentiating
% the polynomial fit twice.
%
% The normal vector is used in conjunction with the geometric coordinates of
% each point in order to calculate the curvature perpendicular to the r-z plane.
%  The mean curvature at each point is calculated by averaging the in-plane and
% perpendicular curvatures.
%%%%%%%%%%%%%%%%%%%%%%%%%%%%%%%%%%%%%%%%%%%%%%%%%%%%%%%%%%%%%%%%%%%%%%%%%%%%%%%%
```

```
%%%%%%%%%%%%%%%%%%%%%%%%%%%%%%%%%%%%%%%%%%%%%%%%%%%%%%%%%%%%%%%%%%%%%%%%%%%%%%%%
% Get S2, the nodewise list of curve parameters along the interface.  The FEMLAB
% data structure is called 'fem', and the mesh field is 'fem.mesh'.  The
% subfield 'fem.mesh.e' contains boundary data for the mesh, in a series of
% columns describing individual boundary segments.  The third and fourth rows
% are curve parameters for the start and end points of the boundary segment, and
% the fifth row is the boundary number in the current geometry.  In the geometry
% used here, the interface is boundary number 7, and the curve parameter goes
% from 0 at the z-axis to 1 at the r-axis; i.e., from pole to equator.
%%%%%%%%%%%%%%%%%%%%%%%%%%%%%%%%%%%%%%%%%%%%%%%%%%%%%%%%%%%%%%%%%%%%%%%%%%%%%%%%
if t ~= 0, S2_old = S2; end; clear S2; ind = 1;
for i = 1:size(fem.mesh.e,2);
    if fem.mesh.e(5,i) == 7;
        S1(ind) = fem.mesh.e(3,i);
        S1(ind+1) = fem.mesh.e(4,i);
        ind = ind + 2;
    end
end

%%%%%%%%%%%%%%%%%%%%%%%%%%%%%%%%%%%%%%%%%%%%%%%%%%%%%%%%%%%%%%%%%%%%%%%%%%%%%%%%
% Reorder list to be monotonically increasing, and remove repeated points.
%%%%%%%%%%%%%%%%%%%%%%%%%%%%%%%%%%%%%%%%%%%%%%%%%%%%%%%%%%%%%%%%%%%%%%%%%%%%%%%%
S1 = (sortrows(S1'))';
S2 = unique(S1);

%%%%%%%%%%%%%%%%%%%%%%%%%%%%%%%%%%%%%%%%%%%%%%%%%%%%%%%%%%%%%%%%%%%%%%%%%%%%%%%%
% Get positions of the boundary points in the normalized geometry, using
% FEMLAB's postprocessing interpolator 'postinterp' on domain 7 (the interface).
%%%%%%%%%%%%%%%%%%%%%%%%%%%%%%%%%%%%%%%%%%%%%%%%%%%%%%%%%%%%%%%%%%%%%%%%%%%%%%%%
clear r z;
r = postinterp(fem,'r',S2(1:end),'dom',7,'ext',1);
z = postinterp(fem,'z',S2(1:end),'dom',7,'ext',1);

%%%%%%%%%%%%%%%%%%%%%%%%%%%%%%%%%%%%%%%%%%%%%%%%%%%%%%%%%%%%%%%%%%%%%%%%%%%%%%%%
% Interpolation vector; boundary points with extension for curve fitting.
%%%%%%%%%%%%%%%%%%%%%%%%%%%%%%%%%%%%%%%%%%%%%%%%%%%%%%%%%%%%%%%%%%%%%%%%%%%%%%%%
r_int = [-r(3) -r(2) r(1:end) r(end-1) r(end-2)];
z_int = [z(3) z(2) z(1:end) -z(end-1) -z(end-2)];

%%%%%%%%%%%%%%%%%%%%%%%%%%%%%%%%%%%%%%%%%%%%%%%%%%%%%%%%%%%%%%%%%%%%%%%%%%%%%%%%
% Outward normal based on quartic polynomial fit.  The procedure operates on
% each entry in the interpolation vector that corresponds to an actual boundary
% node, so the first and last two points are ignored.
%%%%%%%%%%%%%%%%%%%%%%%%%%%%%%%%%%%%%%%%%%%%%%%%%%%%%%%%%%%%%%%%%%%%%%%%%%%%%%%%
clear n_r n_z;
for i = 3:length(r_int)-2;

    %%%%%%%%%%%%%%%%%%%%%%%%%%%%%%%%%%%%%%%%%%%%%%%%%%%%%%%%%%%%%%%%%%%%%%%%%%%%
    % Coordinate transform.  'alpha' is the angle between the r-axis and the
    % line connecting the i-2 and i+2 points.  'phase' is a MATLAB function for
    % complex numbers; hence the sqrt(-1).
    %%%%%%%%%%%%%%%%%%%%%%%%%%%%%%%%%%%%%%%%%%%%%%%%%%%%%%%%%%%%%%%%%%%%%%%%%%%%
    alpha = phase(r_int(i+2)-r_int(i-2)+(z_int(i+2)-z_int(i-2))*sqrt(-1));

    %%%%%%%%%%%%%%%%%%%%%%%%%%%%%%%%%%%%%%%%%%%%%%%%%%%%%%%%%%%%%%%%%%%%%%%%%%%%
    % Remap r_int and z_int around the point of interest to xfit and yfit (five
    % points long) by rotation:
    %%%%%%%%%%%%%%%%%%%%%%%%%%%%%%%%%%%%%%%%%%%%%%%%%%%%%%%%%%%%%%%%%%%%%%%%%%%%
    xfit = 0; yfit = 0;
    for j = i-1:i+1;
        beta = phase(r_int(j)-r_int(i-2)+(z_int(j)-z_int(i-2))*sqrt(-1));
        theta = beta - alpha;
        xfit(j+3-i) = sqrt((r_int(j)-r_int(i-2))^2+(z_int(j)...
            -z_int(i-2))^2)*cos(theta);
        yfit(j+3-i) = sqrt((r_int(j)-r_int(i-2))^2+(z_int(j)...
            -z_int(i-2))^2)*sin(theta);
    end
    xfit(end+1) = sqrt((r_int(i+2)-r_int(i-2))^2+(z_int(i+2)-z_int(i-2))^2);
    yfit(end+1) = 0;

    %%%%%%%%%%%%%%%%%%%%%%%%%%%%%%%%%%%%%%%%%%%%%%%%%%%%%%%%%%%%%%%%%%%%%%%%%%%%
    % Fourth-order polynomial fit, using the MATLAB function ‘polyfit’.  The
    % coefficients are written to a row in the matrix ‘npoly’, which will
    % contain fits for all the boundary nodes.  Another matrix ‘d_npoly’ is
    % generated containing the coefficents of the analytic first derivative of
    % ‘npoly’.
    %%%%%%%%%%%%%%%%%%%%%%%%%%%%%%%%%%%%%%%%%%%%%%%%%%%%%%%%%%%%%%%%%%%%%%%%%%%%
    npoly(i-2,:) = polyfit(xfit,yfit,4);
    for j = 1:size(npoly,2)-1;
        d_npoly(i-2,j) = (size(npoly,2)-j)*npoly(i-2,j);
    end

    %%%%%%%%%%%%%%%%%%%%%%%%%%%%%%%%%%%%%%%%%%%%%%%%%%%%%%%%%%%%%%%%%%%%%%%%%%%%
    % The slope ‘tfit’ at each point in its local rotated coordinate system is
    % found, and local tangent vector components derived by Pythagoras’ theorem.
    % Normal components are then calculated from the tangent components.
    %%%%%%%%%%%%%%%%%%%%%%%%%%%%%%%%%%%%%%%%%%%%%%%%%%%%%%%%%%%%%%%%%%%%%%%%%%%%
    tfit = polyval(d_npoly(i-2,:),xfit(3));
    t_x = 1/sqrt(1+tfit^2); t_y = tfit/sqrt(1+tfit^2);
    n_x = -t_y;
    n_y = t_x;

    %%%%%%%%%%%%%%%%%%%%%%%%%%%%%%%%%%%%%%%%%%%%%%%%%%%%%%%%%%%%%%%%%%%%%%%%%%%%
    % Rotation of slope data at point of interest back to the global coordinate
    % system, yielding ‘dz’ which is z’(r), as well as the
    % normal vector components ‘n_r’ and ‘n_z’ at that point.
    %%%%%%%%%%%%%%%%%%%%%%%%%%%%%%%%%%%%%%%%%%%%%%%%%%%%%%%%%%%%%%%%%%%%%%%%%%%%
    gamma = pi/2 - atan(n_x/n_y);
    if i < length(r_int)-2;
        dz(i-2) = tan(alpha+gamma-pi/2);
    else
        dz(i-2) = -Inf;
    end
    n_r(i-2) = cos(alpha+gamma); n_z(i-2) = sin(alpha+gamma);
end
```

```
clear npoly d_npoly;

%%%%%%%%%%%%%%%%%%%%%%%%%%%%%%%%%%%%%%%%%%%%%%%%%%%%%%%%%%%%%%%%%%%%%%%%%%%%%%%%
% In-plane curvature based on quartic polynomial fit.  Once again, the procedure
% operates on each entry in the interpolation vector that corresponds to an
% actual boundary node, so the first and last two points are ignored.
%%%%%%%%%%%%%%%%%%%%%%%%%%%%%%%%%%%%%%%%%%%%%%%%%%%%%%%%%%%%%%%%%%%%%%%%%%%%%%%%
for i = 3:length(r_int)-2;

    %%%%%%%%%%%%%%%%%%%%%%%%%%%%%%%%%%%%%%%%%%%%%%%%%%%%%%%%%%%%%%%%%%%%%%%%%%%%%%
    % Coordinate transform.  This time the local coordinate system at each point
    % has a vertical axis parallel to the normal vector calculated above.
    %%%%%%%%%%%%%%%%%%%%%%%%%%%%%%%%%%%%%%%%%%%%%%%%%%%%%%%%%%%%%%%%%%%%%%%%%%%%%%
    alpha = phase(n_z(i-2)-n_r(i-2)*sqrt(-1));

    %%%%%%%%%%%%%%%%%%%%%%%%%%%%%%%%%%%%%%%%%%%%%%%%%%%%%%%%%%%%%%%%%%%%%%%%%%%%%%
    % As before, remap r_int and z_int around the point of interest to xfit and
    % yfit (five points long) by rotation:
    %%%%%%%%%%%%%%%%%%%%%%%%%%%%%%%%%%%%%%%%%%%%%%%%%%%%%%%%%%%%%%%%%%%%%%%%%%%%%%
    xfit = 0; yfit = 0;
    for j = i-1:i+2;
        beta = phase(r_int(j)-r_int(i-2)+(z_int(j)-z_int(i-2))*sqrt(-1));
        theta = beta - alpha;
        xfit(j+3-i) = sqrt((r_int(j)-r_int(i-2))^2+(z_int(j)...
            -z_int(i-2))^2)*cos(theta);
        yfit(j+3-i) = sqrt((r_int(j)-r_int(i-2))^2+(z_int(j)...
            -z_int(i-2))^2)*sin(theta);
    end

    %%%%%%%%%%%%%%%%%%%%%%%%%%%%%%%%%%%%%%%%%%%%%%%%%%%%%%%%%%%%%%%%%%%%%%%%%%%%%%
    % Fourth-order polynomial fit, using the MATLAB function 'polyfit'.  The
    % coefficients are written to a row in the matrix 'npoly', which will
    % contain fits for all the boundary nodes.  Two more matrices 'd_npoly' and
    % 'dd_npoly' are generated, containing the coefficents of the analytic first
    % and second derivatives of 'npoly', respectively.
    %%%%%%%%%%%%%%%%%%%%%%%%%%%%%%%%%%%%%%%%%%%%%%%%%%%%%%%%%%%%%%%%%%%%%%%%%%%%%%
    npoly(i-2,:) = polyfit(xfit,yfit,4);
    for j = 1:size(npoly,2)-1;
        d_npoly(i-2,j) = (size(npoly,2)-j)*npoly(i-2,j);
    end
    for j = 1:size(d_npoly,2)-1;
        dd_npoly(i-2,j) = (size(d_npoly,2)-j)*d_npoly(i-2,j);
    end

    %%%%%%%%%%%%%%%%%%%%%%%%%%%%%%%%%%%%%%%%%%%%%%%%%%%%%%%%%%%%%%%%%%%%%%%%%%%%%%
    % The in-plane curvature at the point of interest on the normalized geometry
    % is calculated as the local second derivative of the polynomial fit.
    %%%%%%%%%%%%%%%%%%%%%%%%%%%%%%%%%%%%%%%%%%%%%%%%%%%%%%%%%%%%%%%%%%%%%%%%%%%%%%
    K_1(i-2) = polyval(dd_npoly(i-2,:),xfit(3));
end

%%%%%%%%%%%%%%%%%%%%%%%%%%%%%%%%%%%%%%%%%%%%%%%%%%%%%%%%%%%%%%%%%%%%%%%%%%%%%%%%
% The curvature perpendicular to the r-z plane is calculated according to the
% formula of Bhattacharjee (1995), except where this formula becomes singular.
% At the drop pole, which is the first point in the list, the two principal
% curvatures are equal. At the equator, which is the last point in the list,
% the interface is vertical, so the perpendicular curvature is the inverse of
% the local radius.
%%%%%%%%%%%%%%%%%%%%%%%%%%%%%%%%%%%%%%%%%%%%%%%%%%%%%%%%%%%%%%%%%%%%%%%%%%%%%%%%
for i = 1:length(S2);
    if i == 1;
        K_2(i) = K_1(i);
    elseif i == length(S2);
        K_2(i) = -1/r(i);
    else
        K_2(i) = dz(i)/(r(i)*sqrt(1+dz(i)^2));
    end
end

%%%%%%%%%%%%%%%%%%%%%%%%%%%%%%%%%%%%%%%%%%%%%%%%%%%%%%%%%%%%%%%%%%%%%%%%%%%%%%%%
% Mean curvature is the average the two principal curvatures.
%%%%%%%%%%%%%%%%%%%%%%%%%%%%%%%%%%%%%%%%%%%%%%%%%%%%%%%%%%%%%%%%%%%%%%%%%%%%%%%%
K2 = (K_1+K_2)./2;

%%%%%%%%%%%%%%%%%%%%%%%%%%%%%%%%%%%%%%%%%%%%%%%%%%%%%%%%%%%%%%%%%%%%%%%%%%%%%%%%
% Since the curvatures were calculated on the normalized geometry, the scaling
% factor 'lscale', equal to the drop radius, must be introduced to generate the
% correct fully dimensional result. The units of curvature are 1/m.
%%%%%%%%%%%%%%%%%%%%%%%%%%%%%%%%%%%%%%%%%%%%%%%%%%%%%%%%%%%%%%%%%%%%%%%%%%%%%%%%
clear K;
K = K2./lscale;
```

A.3 Moving Mesh

```
%%%%%%%%%%%%%%%%%%%%%%%%%%%%%%%%%%%%%%%%%%%%%%%%%%%%%%%%%%%%%%%%%%%%%%%%%%%%%%%%
% A quadratic time integration of the local pointwise velocity over the time
% step is used to move the finite element mesh. The three output solution times
% are equally spaced, so the average velocity based on a parabolic fit is 2/3 of
% the midpoint velocity plus 1/6 each of the initial and final velocities.
%  Values at each time are obtained by applying the FEMLAB postprocessing
% interpolator 'postinterp' on a saved copy 'fem0' of the FEMLAB data structure.
% Internal and external velocity integrations are done separately and then
% summed, and measures are taken to ensure that each point is convected by only
% one velocity vector. The result is a list of distances in the r and z
% directions, which can then be added to the geometric coordinates of the points
% in the mesh.
%%%%%%%%%%%%%%%%%%%%%%%%%%%%%%%%%%%%%%%%%%%%%%%%%%%%%%%%%%%%%%%%%%%%%%%%%%%%%%%%
clear pmoveri pmovezi pmovere pmoveze pmover pmovez

%%%%%%%%%%%%%%%%%%%%%%%%%%%%%%%%%%%%%%%%%%%%%%%%%%%%%%%%%%%%%%%%%%%%%%%%%%%%%%%%
% First, the internal velocity variables 'u' and 'v' are time-integrated at each
% point in the mesh, according to the coordinate list 'fem0.mesh.p'. For points
% in the external fluid, this procedure will return NaN (Not a Number). The
% results in 'pmoveri' and 'pmovezi' are nondimensional, but will require
% additional scaling before use.  When the mesh is moved, these values will be
% multiplied by 'S', the Strouhal number, in order to complete the
% nondimensionalization.
%%%%%%%%%%%%%%%%%%%%%%%%%%%%%%%%%%%%%%%%%%%%%%%%%%%%%%%%%%%%%%%%%%%%%%%%%%%%%%%%
pmoveri = tstep.*(postinterp(fem0,'u',[fem0.mesh.p(1,1:end);...
    fem0.mesh.p(2,1:end)],'dom',1,'solnum',1,'ext',0)./6+...
    postinterp(fem0,'u',[fem0.mesh.p(1,1:end);...
    fem0.mesh.p(2,1:end)],'dom',1,'solnum',2,'ext',0).*(2/3)+...
    postinterp(fem0,'u',[fem0.mesh.p(1,1:end);...
    fem0.mesh.p(2,1:end)],'dom',1,'solnum',3,'ext',0)./6);
pmovezi = tstep.*(postinterp(fem0,'v',[fem0.mesh.p(1,1:end);...
    fem0.mesh.p(2,1:end)],'dom',1,'solnum',1,'ext',0)./6+...
    postinterp(fem0,'v',[fem0.mesh.p(1,1:end);...
    fem0.mesh.p(2,1:end)],'dom',1,'solnum',2,'ext',0).*(2/3)+...
    postinterp(fem0,'v',[fem0.mesh.p(1,1:end);...
    fem0.mesh.p(2,1:end)],'dom',1,'solnum',3,'ext',0)./6);

%%%%%%%%%%%%%%%%%%%%%%%%%%%%%%%%%%%%%%%%%%%%%%%%%%%%%%%%%%%%%%%%%%%%%%%%%%%%%%%%
% Repeat the above, but for the external variables 'ue' and 've'.  This will
% return NaN for points inside the drop.
%%%%%%%%%%%%%%%%%%%%%%%%%%%%%%%%%%%%%%%%%%%%%%%%%%%%%%%%%%%%%%%%%%%%%%%%%%%%%%%%
pmovere = tstep.*(postinterp(fem0,'ue',[fem0.mesh.p(1,1:end);...
    fem0.mesh.p(2,1:end)],'dom',2,'solnum',1,'ext',0)./6+...
    postinterp(fem0,'ue',[fem0.mesh.p(1,1:end);...
    fem0.mesh.p(2,1:end)],'dom',2,'solnum',2,'ext',0).*(2/3)+...
    postinterp(fem0,'ue',[fem0.mesh.p(1,1:end);...
    fem0.mesh.p(2,1:end)],'dom',2,'solnum',3,'ext',0)./6);
pmoveze = tstep.*(postinterp(fem0,'ve',[fem0.mesh.p(1,1:end);...
    fem0.mesh.p(2,1:end)],'dom',2,'solnum',1,'ext',0)./6+...
    postinterp(fem0,'ve',[fem0.mesh.p(1,1:end);...
    fem0.mesh.p(2,1:end)],'dom',2,'solnum',2,'ext',0).*(2/3)+...
    postinterp(fem0,'ve',[fem0.mesh.p(1,1:end);...
    fem0.mesh.p(2,1:end)],'dom',2,'solnum',3,'ext',0)./6);

%%%%%%%%%%%%%%%%%%%%%%%%%%%%%%%%%%%%%%%%%%%%%%%%%%%%%%%%%%%%%%%%%%%%%%%%%%%%%%%%
% Points on the interface are shared between fluids.
In order to obtain correct values for points on the interface, and correct for
% possible numerical artifacts leading to failures of 'postinterp' on outer
% boundaries with extrapolation turned off, the boundaries are treated
% separately.  Extrapolation is turned on, and the interface is considered to be
% part of the internal fluid.
%
% The boundary element matrix 'fem0.mesh.e' contains columns describing
% individual boundary segments on the mesh.  The first two rows are indices of
% the start and end points, respectively, into the coordinate list
% 'fem0.mesh.p'.  The fifth row contains the boundary number.  In this case,
% boundaries 1, 2, and 7 bound the drop, and 3, 4, 5, and 6 are boundaries of
% the external fluid.  Boundary 7 is the interface.  The list 'bndpts_i'
% consists of points on boundaries of the internal fluid, and 'bndpts_e'
% contains points on boundaries of the external fluid.
%%%%%%%%%%%%%%%%%%%%%%%%%%%%%%%%%%%%%%%%%%%%%%%%%%%%%%%%%%%%%%%%%%%%%%%%%%%%%%%%
bndpts_i = []; bndpts_e = [];
```

```
for i = 1:size(fem0.mesh.e,2);
    switch fem0.mesh.e(5,i)
        case {1, 2, 7}
            bndpts_i(end+1:end+2,1) = fem0.mesh.e(1:2,i);
        case {3, 4, 5, 6}
            bndpts_e(end+1:end+2,1) = fem0.mesh.e(1:2,i);
        otherwise
            error('Boundary number mismatch during mesh update.');
    end
end
bndpts_i = unique(bndpts_i); bndpts_e = unique(bndpts_e);

%%%%%%%%%%%%%%%%%%%%%%%%%%%%%%%%%%%%%%%%%%%%%%%%%%%%%%%%%%%%%%%%%%%%%%%%%%%%%%%%%%
% The time-integrals of the internal velocities ‘u’ and ‘v’ are now obtained for
% the points in ‘bndpts_i’.  The corresponding entries in the external velocity
% integration lists are forced to zero.
%%%%%%%%%%%%%%%%%%%%%%%%%%%%%%%%%%%%%%%%%%%%%%%%%%%%%%%%%%%%%%%%%%%%%%%%%%%%%%%%%%
pmoveri(bndpts_i) = tstep.*(postinterp(fem0,'u',[fem0.mesh.p(1,bndpts_i);...
    fem0.mesh.p(2,bndpts_i)],'dom',1,'solnum',1,'ext',1)./6+...
    postinterp(fem0,'u',[fem0.mesh.p(1,bndpts_i);...
    fem0.mesh.p(2,bndpts_i)],'dom',1,'solnum',2,'ext',1).*(2/3)+...
    postinterp(fem0,'u',[fem0.mesh.p(1,bndpts_i);...
    fem0.mesh.p(2,bndpts_i)],'dom',1,'solnum',3,'ext',1)./6);
pmovezi(bndpts_i) = tstep.*(postinterp(fem0,'v',[fem0.mesh.p(1,bndpts_i);...
    fem0.mesh.p(2,bndpts_i)],'dom',1,'solnum',1,'ext',1)./6+...
    postinterp(fem0,'v',[fem0.mesh.p(1,bndpts_i);...
    fem0.mesh.p(2,bndpts_i)],'dom',1,'solnum',2,'ext',1).*(2/3)+...
    postinterp(fem0,'v',[fem0.mesh.p(1,bndpts_i);...
    fem0.mesh.p(2,bndpts_i)],'dom',1,'solnum',3,'ext',1)./6);
pmovere(bndpts_i) = 0;
pmoveze(bndpts_i) = 0;

%%%%%%%%%%%%%%%%%%%%%%%%%%%%%%%%%%%%%%%%%%%%%%%%%%%%%%%%%%%%%%%%%%%%%%%%%%%%%%%%%%
% The time-integrals of the external velocities ‘ue’ and ‘ve’ are now obtained
% for the points in ‘bndpts_e’.  The corresponding entries in the internal
% velocity integration lists are forced to zero.
%%%%%%%%%%%%%%%%%%%%%%%%%%%%%%%%%%%%%%%%%%%%%%%%%%%%%%%%%%%%%%%%%%%%%%%%%%%%%%%%%%
pmovere(bndpts_e) = tstep.*(postinterp(fem0,'ue',[fem0.mesh.p(1,bndpts_e);...
    fem0.mesh.p(2,bndpts_e)],'dom',2,'solnum',1,'ext',1)./6+...
    postinterp(fem0,'ue',[fem0.mesh.p(1,bndpts_e);...
    fem0.mesh.p(2,bndpts_e)],'dom',2,'solnum',2,'ext',1).*(2/3)+...
    postinterp(fem0,'ue',[fem0.mesh.p(1,bndpts_e);...
    fem0.mesh.p(2,bndpts_e)],'dom',2,'solnum',3,'ext',1)./6);
pmoveze(bndpts_e) = tstep.*(postinterp(fem0,'ve',[fem0.mesh.p(1,bndpts_e);...
    fem0.mesh.p(2,bndpts_e)],'dom',2,'solnum',1,'ext',1)./6+...
    postinterp(fem0,'ve',[fem0.mesh.p(1,bndpts_e);...
    fem0.mesh.p(2,bndpts_e)],'dom',2,'solnum',2,'ext',1).*(2/3)+...
    postinterp(fem0,'ve',[fem0.mesh.p(1,bndpts_e);...
    fem0.mesh.p(2,bndpts_e)],'dom',2,'solnum',3,'ext',1)./6);
pmoveri(bndpts_e) = 0;
pmovezi(bndpts_e) = 0;

%%%%%%%%%%%%%%%%%%%%%%%%%%%%%%%%%%%%%%%%%%%%%%%%%%%%%%%%%%%%%%%%%%%%%%%%%%%%%%%%%%
```

```
% Any entries in any of the integration vectors which are NaN are assigned zero.
%  This procedure, coupled with the above exclusive treatment of boundaries,
% should produce a set of lists in which each point has nonzero r- and
% z-direction velocity integrations from only one of the fluids.  The only
% possible exceptions to this are the start and end points of the interface,
% which are shared between three boundaries.  This case is treated specifically
% below.
%%%%%%%%%%%%%%%%%%%%%%%%%%%%%%%%%%%%%%%%%%%%%%%%%%%%%%%%%%%%%%%%%%%%%%%%%%%%%%%%
for i = 1:length(pmoveri);
    if isnan(pmoveri(i));
        pmoveri(i) = 0;
    end
    if isnan(pmovezi(i));
        pmovezi(i) = 0;
    end
    if isnan(pmovere(i));
        pmovere(i) = 0;
    end
    if isnan(pmoveze(i));
        pmoveze(i) = 0;
    end
end

%%%%%%%%%%%%%%%%%%%%%%%%%%%%%%%%%%%%%%%%%%%%%%%%%%%%%%%%%%%%%%%%%%%%%%%%%%%%%%%%
% The two pairs of lists are summed, to create a single list pair corresponding
% to convection distances in the r-direction ('pmover') and z-direction
% ('pmovez') respectively.
%%%%%%%%%%%%%%%%%%%%%%%%%%%%%%%%%%%%%%%%%%%%%%%%%%%%%%%%%%%%%%%%%%%%%%%%%%%%%%%%
pmover = pmoveri + pmovere;
pmovez = pmovezi + pmoveze;

%%%%%%%%%%%%%%%%%%%%%%%%%%%%%%%%%%%%%%%%%%%%%%%%%%%%%%%%%%%%%%%%%%%%%%%%%%%%%%%%
% The correct value of convection distance for the interface endpoints - the
% points at the z-axis (the pole) and r-axis (the equator) - is particularly
% vital.  Since these points are shared between three boundaries each, the above
% procedure may not produce the correct values, so they are analyzed
% individually to obtain the proper result.  In the geometry as defined, these
% two points are numbered 2 and 4, respectively.
%%%%%%%%%%%%%%%%%%%%%%%%%%%%%%%%%%%%%%%%%%%%%%%%%%%%%%%%%%%%%%%%%%%%%%%%%%%%%%%%
pmover(2) = 0;
pmovez(2) = tstep*(postinterp(fem0,'v',fem0.mesh.p(:,2),...
    'dom',1,'solnum',1,'ext',1)/6+...
    postinterp(fem0,'v',fem0.mesh.p(:,2),'dom',1,'solnum',2,'ext',1)*2/3+...
    postinterp(fem0,'v',fem0.mesh.p(:,2),'dom',1,'solnum',3,'ext',1)/6);
pmover(4) = tstep*(postinterp(fem0,'u',fem0.mesh.p(:,4),...
    'dom',1,'solnum',1,'ext',1)/6+...
    postinterp(fem0,'u',fem0.mesh.p(:,4),'dom',1,'solnum',2,'ext',1)*2/3+...
    postinterp(fem0,'u',fem0.mesh.p(:,4),'dom',1,'solnum',3,'ext',1)/6);
pmovez(4) = 0;

%%%%%%%%%%%%%%%%%%%%%%%%%%%%%%%%%%%%%%%%%%%%%%%%%%%%%%%%%%%%%%%%%%%%%%%%%%%%%%%%
% The mesh is moved by summing the results of the above procedure with the node
% positions.  Due to the presence of the Strouhal number 'S' in the Navier-
% Stokes nondimensionalization, so that the characteristic velocity is not equal
% to the characteristic length divided by the characteristic time, the correct
% application of this technique requires the Strouhal number as a multiplier in
% the mesh motion.
%%%%%%%%%%%%%%%%%%%%%%%%%%%%%%%%%%%%%%%%%%%%%%%%%%%%%%%%%%%%%%%%%%%%%%%%%%%%%%%%
fem0.mesh.p=fem0.mesh.p+[S.*pmover;S.*pmovez];

%%%%%%%%%%%%%%%%%%%%%%%%%%%%%%%%%%%%%%%%%%%%%%%%%%%%%%%%%%%%%%%%%%%%%%%%%%%%%%%%
% Since the mesh structure stores the curve parameter in pointwise fashion,
% moving the mesh moves the curve parameter along with it, which can distort the
% curve parameter and produce unexpected results when remeshing.  This function
% rescales the curve parameter to be proportional to chord length, which removes
% the convection effect.
%%%%%%%%%%%%%%%%%%%%%%%%%%%%%%%%%%%%%%%%%%%%%%%%%%%%%%%%%%%%%%%%%%%%%%%%%%%%%%%%
fem0.mesh=chord(fem0.mesh);

%%%%%%%%%%%%%%%%%%%%%%%%%%%%%%%%%%%%%%%%%%%%%%%%%%%%%%%%%%%%%%%%%%%%%%%%%%%%%%%%
% For consistency in obtaining values from the moved FEM structure 'fem0', the
% geometry 'fem0.geom' and extended mesh 'fem0.xmesh' are updated.
%%%%%%%%%%%%%%%%%%%%%%%%%%%%%%%%%%%%%%%%%%%%%%%%%%%%%%%%%%%%%%%%%%%%%%%%%%%%%%%%
fem0.geom=fem0.mesh;
fem0.xmesh=meshextend(fem0);
```

A.4 Curve Parameter Correction

```
function cmesh = chord(mesh);

%%%%%%%%%%%%%%%%%%%%%%%%%%%%%%%%%%%%%%%%%%%%%%%%%%%%%%%%%%%%%%%%%%%%%%%%%%%%%%%%
%CHORD    Correct curve parameter values in a distorted FEMLAB mesh.
%   CMESH = CHORD(MESH) takes a 2-D FEMLAB mesh MESH and returns it with
%   the curve parameter values along the boundaries reset according to
%   chord length.  The correction is made by first calculating the total
%   length of all segments of a boundary, and then dividing the length of
%   each segment by the total to obtain the span of its curve parameter.
%   The start and end values are corrected to 0 and 1, respectively.
%
%   Since the underlying geometry is not known, chord length calculations
%    do not account for element curvature, and are simply sums of linear
%   distances between successive nodes.
%
%   The purpose of this utility is to provide a fix for mesh degradation in
%   custom moving mesh codes where significant flow along a boundary is
%   expected.  It should only be used if all boundaries have curve
%   parameters spanning 0 -> 1.
%%%%%%%%%%%%%%%%%%%%%%%%%%%%%%%%%%%%%%%%%%%%%%%%%%%%%%%%%%%%%%%%%%%%%%%%%%%%%%%%

%%%%%%%%%%%%%%%%%%%%%%%%%%%%%%%%%%%%%%%%%%%%%%%%%%%%%%%%%%%%%%%%%%%%%%%%%%%%%%%%
% This procedure is performed on each boundary in the geometry, according to the
% boundary numbers in the fifth row boundary element matrix 'mesh.e'.
%
```

```
% The boundary element matrix consists of columns describing individual boundary
% segments between nodes in the mesh.  The first two rows are indices of the
% start and end points into the geometric coordinate list 'mesh.p'.  The third
% and fourth rows are curve parameters for the start and end points.  The fifth
% row is the number of the boundary containing the segment in question.
%%%%%%%%%%%%%%%%%%%%%%%%%%%%%%%%%%%%%%%%%%%%%%%%%%%%%%%%%%%%%%%%%%%%%%%%%%%%%%%%%%
for i = 1:max(mesh.e(5,:));
    bndlength = 0; indices = [];

    %%%%%%%%%%%%%%%%%%%%%%%%%%%%%%%%%%%%%%%%%%%%%%%%%%%%%%%%%%%%%%%%%%%%%%%%%%%%%%
    % For each column 'j' in 'mesh.e', the boundary number is checked to see if
    % it matches the working boundary number 'i'.  If it does, its length is
    % calculated from the coordinate list 'mesh.p' and added to the boundary
    % length 'bndlength'.  A list 'indices' is also built of the column indices
    % belonging to the working boundary.
    %
    % Boundary numbers should be integers, but for robustness the equality check
    % is adjusted so that it will still work if MATLAB has jiggled one of the
    % values slightly.
    %%%%%%%%%%%%%%%%%%%%%%%%%%%%%%%%%%%%%%%%%%%%%%%%%%%%%%%%%%%%%%%%%%%%%%%%%%%%%%
    for j = 1:size(mesh.e,2);
        if abs(mesh.e(5,j)-i) < 0.1;
            indices(end+1) = j;
            bndlength = bndlength + sqrt((mesh.p(1,mesh.e(1,j))-...
                mesh.p(1,mesh.e(2,j)))^2+(mesh.p(2,mesh.e(1,j))-...
                mesh.p(2,mesh.e(2,j)))^2);
        end
    end

    %%%%%%%%%%%%%%%%%%%%%%%%%%%%%%%%%%%%%%%%%%%%%%%%%%%%%%%%%%%%%%%%%%%%%%%%%%%%%%
    % The starting boundary segment is determined by the smallest value of the
    % start point curve parameter out of all the segments on the working
    % boundary.  The variable 'seg' is assigned the index of the corresponding
    % column in 'mesh.e'.
    %%%%%%%%%%%%%%%%%%%%%%%%%%%%%%%%%%%%%%%%%%%%%%%%%%%%%%%%%%%%%%%%%%%%%%%%%%%%%%
    startparam = 1;
    for j = indices;
        if mesh.e(3,j) < startparam;
            startparam = mesh.e(3,j);
            seg = j;
        end
    end

    %%%%%%%%%%%%%%%%%%%%%%%%%%%%%%%%%%%%%%%%%%%%%%%%%%%%%%%%%%%%%%%%%%%%%%%%%%%%%%
    % The curve parameters for the boundary must now be modified.  Stepping
    % through the boundary is done via a while-loop, with a test indicating that
    % the last boundary segment has not yet been found.  The point at the start
    % of the segment is assigned a curve parameter of 'startparam'.  The second
    % point is assigned 'startparam' plus 'paramspan', which is a value obtained
    % by dividing the length of the segment by the total 'bndlength'.  This sum
    % is then assigned to 'startparam', so that the curve parameter is advanced
    % according to the fractional length of each segment relative to the entire
    % boundary as the loop progresses.
```

```
%%%%%%%%%%%%%%%%%%%%%%%%%%%%%%%%%%%%%%%%%%%%%%%%%%%%%%%%%%%%%%%%%%%%%%%%%%%%%%%%
startparam = 0; done = 0;
while done == 0;
    mesh.e(3,seg) = startparam;
    paramspan = sqrt((mesh.p(1,mesh.e(1,seg))-...
            mesh.p(1,mesh.e(2,seg)))^2+(mesh.p(2,mesh.e(1,seg))-...
            mesh.p(2,mesh.e(2,seg)))^2)/bndlength;
    mesh.e(4,seg) = startparam+paramspan;
    startparam = mesh.e(4,seg); lastseg = seg;

    %%%%%%%%%%%%%%%%%%%%%%%%%%%%%%%%%%%%%%%%%%%%%%%%%%%%%%%%%%%%%%%%%%%%%%%%%%%%
    % After reassigning start and end curve parameters for a single segment,
    % the next segment is found by searching for the index of the current
    % end point in the start point row of all columns of 'mesh.e' listed
    % in 'indices'.
    %%%%%%%%%%%%%%%%%%%%%%%%%%%%%%%%%%%%%%%%%%%%%%%%%%%%%%%%%%%%%%%%%%%%%%%%%%%%
    for j = indices;
        if abs(mesh.e(2,lastseg)-mesh.e(1,j)) < 0.1;
            seg = j;
        end
    end

    %%%%%%%%%%%%%%%%%%%%%%%%%%%%%%%%%%%%%%%%%%%%%%%%%%%%%%%%%%%%%%%%%%%%%%%%%%%%
    % If the above loop did not find a match, the last segment treated was
    % the end of the boundary.  The ending curve parameter is set to 1, and
    % the while-loop exits.
    %%%%%%%%%%%%%%%%%%%%%%%%%%%%%%%%%%%%%%%%%%%%%%%%%%%%%%%%%%%%%%%%%%%%%%%%%%%%
    if lastseg == seg;
        mesh.e(4,lastseg) = 1;
        done = 1;
    end
  end
end
cmesh = mesh;
```

A.5 Solution Reinitialization

```
%%%%%%%%%%%%%%%%%%%%%%%%%%%%%%%%%%%%%%%%%%%%%%%%%%%%%%%%%%%%%%%%%%%%%%%%%%%%%%%%
% DASPK requires a solution vector as an initial condition for a time-dependent
% problem.  In the second and subsequent time steps, it is necessary to
% construct this solution vector based on the solution at the end of the
% previous time step.  Since the full Navier-Stokes equations are used, allowing
% the solution to remain on the nodes is inadmissible, because this constitutes
% convection, which is already accounted for in the equation set.  Therefore the
% solution must be interpolated in place, without convection, onto the new,
% convected, extended mesh.  This method does not require any modification to
% map a solution onto a reinitialized mesh, as it makes no assumptions about the
% location or number of individual degrees of freedom.
%%%%%%%%%%%%%%%%%%%%%%%%%%%%%%%%%%%%%%%%%%%%%%%%%%%%%%%%%%%%%%%%%%%%%%%%%%%%%%%%
```

```
%%%%%%%%%%%%%%%%%%%%%%%%%%%%%%%%%%%%%%%%%%%%%%%%%%%%%%%%%%%%%%%%%%%%%%%%%%%%%%%%%%
% If this is the first time step, the initialization is a standard FEMLAB call.
%%%%%%%%%%%%%%%%%%%%%%%%%%%%%%%%%%%%%%%%%%%%%%%%%%%%%%%%%%%%%%%%%%%%%%%%%%%%%%%%%%
if t == 0;
    init=asseminit(fem, ...
        'context','local', ...
        'init',   fem.xmesh.eleminit);

%%%%%%%%%%%%%%%%%%%%%%%%%%%%%%%%%%%%%%%%%%%%%%%%%%%%%%%%%%%%%%%%%%%%%%%%%%%%%%%%%%
% If this is not the first time step, the interpolation method must be used.
%%%%%%%%%%%%%%%%%%%%%%%%%%%%%%%%%%%%%%%%%%%%%%%%%%%%%%%%%%%%%%%%%%%%%%%%%%%%%%%%%%
else

    %%%%%%%%%%%%%%%%%%%%%%%%%%%%%%%%%%%%%%%%%%%%%%%%%%%%%%%%%%%%%%%%%%%%%%%%%%%%%%
    %  The global degree of freedom (DOF) list 'fem.xmesh.gdof' has rows
    % corresponding to point indices in the geometric coordinate list
    % 'fem.xmesh.p', and columns corresponding to the index into the variable
    % name list 'fem.xmesh.name' for the global variable each degree of freedom
    % belongs to.  The entries in the DOF list are the actual DOF numbers, which
    % serve as indices into the initial solution vector 'init'.  The '{1}' at
    % the end of each data structure call is a cell array index corresponding to
    % the geometry number; in this case there is only one geometry, so the value
    % of this index is always 1.
    %
    % For each variable in the name list, a matrix is compiled containing DOF
    % numbers in the first column and point indices in the second column.  This
    % matrix is then row-sorted by DOF number.
    %%%%%%%%%%%%%%%%%%%%%%%%%%%%%%%%%%%%%%%%%%%%%%%%%%%%%%%%%%%%%%%%%%%%%%%%%%%%%%
    init = [];
    for j = 1:size(fem.xmesh.name{1},1);
        indx = 1; clear gdof;
        for i = 1:size(fem.xmesh.gdof{1},1);
            if fem.xmesh.gdof{1}(i,j) ~= 0;
                gdof(indx,1) = fem.xmesh.gdof{1}(i,j);
                gdof(indx,2) = i;
                indx = indx + 1;
            end
        end
        gdof = sortrows(gdof);

        %%%%%%%%%%%%%%%%%%%%%%%%%%%%%%%%%%%%%%%%%%%%%%%%%%%%%%%%%%%%%%%%%%%%%%%%%%%
        % 'fem00' is a copy of the solved FEMLAB data structure from the
        % previous time step.  It has not been convected, so the nodes are not
        % congruent with those in the current extended mesh.  The FEMLAB
        % postprocessing interpolator 'postinterp' is used on the old solution
        % to obtain a value for each DOF in the new extended mesh, with
        % positions given by the coordinate list 'fem.xmesh.p'.  Extrapolation
        % is turned off by setting the option 'ext' to 0.  Since the variables
        % are being dealt with in the order specified by 'fem.xmesh.name', which
        % is the same order as that used in the solution vector, it is
        % sufficient to append the results for each variable to 'init'.
        %%%%%%%%%%%%%%%%%%%%%%%%%%%%%%%%%%%%%%%%%%%%%%%%%%%%%%%%%%%%%%%%%%%%%%%%%%%
        init(end+1:end+size(gdof,1),1) = postinterp(fem00,...
            char(fem.xmesh.name{1}(j,1)),fem.xmesh.p{1}(:,gdof(:,2)),...
            'solnum',size(fem00.sol.u,2),'ext',0)';

        %%%%%%%%%%%%%%%%%%%%%%%%%%%%%%%%%%%%%%%%%%%%%%%%%%%%%%%%%%%%%%%%%%%%%%%%
        % If ‘postinterp’ has returned Not a Number for any DOF in ‘init’, the
        % point in question is assumed to have moved off its subdomain as
        % described by ‘fem00’.  If the point has moved into the other
        % subdomain, the error is recoverable, and the value of the appropriate
        % variable from the other subdomain is used.  Extrapolation is turned
        % on.  This section depends on the specifics of the problem definition,
        % since it assumes that j=1,2,3 mean internal r-velocity, z-velocity,
        % and pressure, respectively, and that j=4,5,6 mean the corresponding
        % external fluid variables.
        %%%%%%%%%%%%%%%%%%%%%%%%%%%%%%%%%%%%%%%%%%%%%%%%%%%%%%%%%%%%%%%%%%%%%%%%
        for i = 1:size(gdof,1);
            if isnan(init(end-size(gdof,1)+i));
                switch j
                    case {1,2,3}
                        init(end-size(gdof,1)+i) = postinterp(fem00,...
                            char(fem.xmesh.name{1}(j+3,1)),...
                            fem.xmesh.p{1}(:,gdof(i,2)),...
                            'solnum',size(fem00.sol.u,2),'ext',1)';
                    case {4,5,6}
                        init(end-size(gdof,1)+i) = postinterp(fem00,...
                        char(fem.xmesh.name{1}(j-3,1)),...
                        fem.xmesh.p{1}(:,gdof(i,2)),...
                        'solnum',size(fem00.sol.u,2),'ext',1)';
                end
            end

            %%%%%%%%%%%%%%%%%%%%%%%%%%%%%%%%%%%%%%%%%%%%%%%%%%%%%%%%%%%%%%%%%%%%
            % If the above method still returns NaN, the error is not
            % recoverable, and 0 is used as the DOF value.  This may occur if a
            % node moves off one of the external boundaries of the old geometry.
            %%%%%%%%%%%%%%%%%%%%%%%%%%%%%%%%%%%%%%%%%%%%%%%%%%%%%%%%%%%%%%%%%%%%
            if isnan(init(end-size(gdof,1)+i));
                init(end-size(gdof,1)+i) = 0;
            end
        end
    end
end
```